

OPTICAL PROPERTIES OF SOME QUATERNARY THALLIUM
CHALCOGENIDES

A THESIS SUBMITTED TO
THE GRADUATE SCHOOL OF NATURAL AND APPLIED SCIENCES
OF
MIDDLE EAST TECHNICAL UNIVERSITY

BY

KADİR GÖKŞEN

IN PARTIAL FULFILLMENT OF THE REQUIREMENTS
FOR
THE DEGREE OF DOCTOR OF PHILOSOPHY
IN
PHYSICS

APRIL 2008

Approval of the thesis:

**OPTICAL PROPERTIES OF SOME QUATERNARY THALLIUM
CHALCOGENIDES**

submitted by **KADİR GÖKŞEN** in partial fulfillment of the requirements for the degree of **Doctor of Philosophy in Physics Department, Middle East Technical University** by,

Prof. Dr. Canan Özgen
Dean, Graduate School of **Natural and Applied Sciences**

Prof. Dr. Sinan Bilikmen
Head of Department, **Physics**

Prof. Dr. Nizami Hasanli
Supervisor, **Physics Dept., METU**

Prof. Dr. Hüsni Özkan
Co-supervisor, **Physics Dept., METU**

Examining Committee Members

Prof. Dr. Yakup Cevdet Akgöz
Engineering Sciences Dept., METU

Prof. Dr. Nizami Hasanli
Physics Dept., METU

Prof. Dr. Raşit Turan
Physics Dept., METU

Prof. Dr. Tofiq Mammedov
Physics Dept., Gazi University

Assoc. Prof. Dr. Enver Bulur
Physics Dept., METU

Date: 14 April 2008

I hereby declare that all information in this document has been obtained and presented in accordance with academic rules and ethical conduct. I also declare that, as required by these rules and conduct, I have fully cited and referenced all material and results that are not original to this work.

Name, Last Name : Kadir Gökşen

Signature :

ABSTRACT

OPTICAL PROPERTIES OF SOME QUATERNARY THALLIUM CHALCOGENIDES

Gökşen, Kadir

Ph. D., Department of Physics

Supervisor: Prof. Dr. Nizami Hasanli

Co-supervisor: Prof. Dr. Hüsnü Özkan

April 2008, 133 pages

Optical properties of $\text{Tl}_4\text{In}_3\text{GaSe}_8$, $\text{Tl}_4\text{InGa}_3\text{Se}_8$, $\text{Tl}_4\text{In}_3\text{GaS}_8$, $\text{Tl}_2\text{InGaS}_4$ and $\text{Tl}_4\text{InGa}_3\text{S}_8$ chain and layered crystals were studied by means of photoluminescence (PL) and transmission-reflection experiments. Several emission bands were observed in the PL spectra within the 475-800 nm wavelength region. The results of the temperature- and excitation intensity-dependent PL measurements in 15-300 K and 0.13×10^{-3} -110.34 W cm^{-2} ranges, respectively, suggested that the observed bands were originated from the recombination of electrons with the holes by realization of donor-acceptor or free-to-bound type transitions. Transmission-reflection measurements in the wavelength range of 400-1100 nm revealed the values of indirect and direct band gap energies of the crystals studied. By the temperature-dependent transmission measurements in 10-300 K range, the rates of

change of the indirect band gap of the samples with temperature were found to be negative. The oscillator and dispersion energies, and zero-frequency refractive indices were determined by the analysis of the refractive index dispersion data using the Wemple–DiDomenico single-effective-oscillator model. Furthermore, the structural parameters of all crystals were defined by the analysis of X-ray powder diffraction data. The determination of the compositional parameters of the studied crystals was done by energy dispersive spectral analysis experiments.

Keywords: Photoluminescence, X-ray diffraction, EDSA (energy dispersive spectral analysis), semiconductors, defect states, optical properties, optical constants, dispersion of refractive index, energy band gap.

ÖZ

BAZI DÖRTLÜ TALYUM ÇALKOGENİTLERİN OPTİK ÖZELLİKLERİ

Gökşen, Kadir

Doktora, Department of Physics

Tez Yöneticisi: Prof. Dr. Nizami Hasanlı

Ortak Tez Yöneticisi: Prof. Dr. Hüsnü Özkan

Nisan 2008, 133 sayfa

$Tl_4In_3GaSe_8$, $Tl_4InGa_3Se_8$, $Tl_4In_3GaS_8$, Tl_2InGaS_4 ve $Tl_4InGa_3S_8$ zincirli ve katmanlı kristallerinin optik özellikleri, fotoişıma ve geçirgenlik-yansıtıcılık deneyleri aracılığıyla incelendi. 475-800 nm dalgaboyu aralığında kaydedilen fotoişıma spektrumlarında çeşitli ışım bantları görüldü. 15-300 K aralığında yapılan sıcaklık ve 0.13×10^{-3} -110.34 $W\ cm^{-2}$ aralığında yapılan uyarım gücü bağımlı deneyler, gözlemlenen bantların sebebinin elektron ve deşiklerin, verici-alıcı veya iletim bandı-alıcı enerji seviyeleri üzerinden yeniden birleşmeleri olduğu anlaşıldı. 400-1100 nm dalgaboyu aralığında yapılan geçirgenlik-yansıtıcılık deneyleri sonucu, örneklerin doğrudan ve dolaylı enerji bant boşlukları bulundu. Dolaylı enerji bant boşluğunun sıcaklığa göre değişim oranı, 10-300 K sıcaklık aralığında yapılan geçirgenlik deneyleri sonucu bütün örnekler için negatif olarak bulundu. Titreşim

enerjileri, dađılma enerjileri ve sıfır frekans kırınım indisleri, Wemple–DiDomenico tek-etkin-osilatör modeli kullanılarak bulundu. Bunların yanısıra, bütün kristallerin yapısal parametreleri, X-ışını saçılım verileri kullanılarak hesaplandı. Ayrıca, örneklerin bileşim parametreleri de enerji dađımlı spektrum analizi deneyleri aracılıđıyla bulundu.

Anahtar kelimeler: Fotoışma, X-ışını saçılımı, EDSA (enerji dađımlı spektrum analizi), yarıiletkenler, safsızlık durumları, optik özellikler, optik sabitler, kırınım indisinin dađılması, energy bant boşluđu.

ACKNOWLEDGMENTS

I would like to express my gratitude to my supervisor, Prof. Dr. Nizami Hasanli, whose expertise, understanding, and patience, added considerably to my graduate study. I could easily say that I would not have been able complete my study without his continuous motivation and encouragement. I also want to thank my co-supervisor, Prof. Dr. Hüsnü Özkan, for his valuable helps and continuous support especially during the X-ray and temperature dependent transmission measurements. His helps and the facilities of the superconductivity laboratory made it possible to complete that part this work.

I would also like to thank to my professors who advised and assisted me during this research, namely Prof. Dr. Raşit Turan, Prof. Dr. Atilla Aydınli, Prof. Dr. Mehmet Parlak, and Assoc. Prof. Dr. Enver Bulur. They provided a lot of help at all levels of my research and I benefitted from their experiences a lot.

I owe a debt of gratitude to my friend and colleague Ayşe Seyhan for her valuable helps, whenever I needed, in the photoluminescence laboratory during the initial stage of this work. I also want to thank to my friends Arife Gençer İmer for her helps with the FTIR measurements, Mustafa Kulakçı and Murat Kaleli for their helps during the production of silver mirrors.

I also wish to give special thanks to my roommate Arif Sinan Alagöz, who is like a brother to me. To speak the truth, without his continuous support and encouragement it would really be harder to complete this study.

Finally, I would like to thank to my family and all of my friends, who were always there for me with their uninterrupted love and patience.

TABLE OF CONTENTS

ABSTRACT	iv
ÖZ	vi
ACKNOWLEDGMENTS	viii
TABLE OF CONTENTS	ix
LIST OF TABLES	xii
LIST OF FIGURES	xiii

CHAPTER

1. INTRODUCTION	1
2. THEORETICAL APPROACH	7
2.1. Introduction	7
2.2. Theoretical Approach to the Band Structure in Semiconductors	8
2.2.1. Introduction	8
2.2.2. Band Structure in Perfect Semiconductors	8
2.2.3. Impurities and Band Structure in Real Semiconductors	13
2.2.4. Configuration Coordinate Model for Band Structure	15
2.2.5. Effect of Temperature on Band Gap Energy	18
2.3. Theoretical Approach to Characterization Experiments	19
2.3.1. X-Ray Diffraction Experiments	19
2.3.2. Energy Dispersive Spectral Analysis (EDSA) Experiments	20
2.3.3. Transmission and Reflection Experiments	22
2.3.4. Photoluminescence Experiments	25
2.3.4.1. Introduction	25
2.3.4.2. Recombination Mechanisms	26

2.3.4.2.a. Band-to-Band Transitions	26
2.3.4.2.b. Free-to-Bound Transitions	27
2.3.4.2.c. Donor-Acceptor Pair Transitions	28
2.3.4.3 Laser Excitation Power Dependence of the Peak Intensity and the Peak Energy of the Photoluminescence Spectra on Semiconductors	29
2.3.4.4. Temperature Dependence of the Peak Intensity and the Peak Energy of the Photoluminescence Spectra on Semiconductors	31
3. EXPERIMENTAL SETUPS AND TECHNIQUES USED IN EXPERIMENTS	36
3.1. Introduction	36
3.2. Energy Dispersive Spectral Analysis Experiments	36
3.3. X-Ray Diffraction Experiments	37
3.4. Transmission and Reflection Experiments	38
3.5. Photoluminescence Experiments	39
3.6. Properties of the Crystals Used in the Experiments	42
4. RESULTS AND DISCUSSION	43
4.1. Introduction	43
4.2. Results of the Structural and Optical Characterization Experiments for $\text{Tl}_4\text{In}_3\text{GaSe}_8$ crystal	43
4.2.1. Results of X-Ray Experiments	44
4.2.2. Results of EDSA Experiments	46
4.2.3. Results of Transmission Experiments	47
4.2.4. Results of Photoluminescence Experiments	49
4.3. Results of the Structural and Optical Characterization Experiments for $\text{Tl}_4\text{InGa}_3\text{Se}_8$ crystal	57
4.3.1. Results of X-Ray Experiments	59
4.3.2. Results of EDSA Experiments	60
4.3.3. Results of Transmission and Reflection Experiments	61
4.3.4. Results of Photoluminescence Experiments	66
4.4. Results of the Structural and Optical Characterization Experiments for $\text{Tl}_4\text{In}_3\text{GaS}_8$ crystal	72
4.4.1. Results of X-Ray Experiments	73

4.4.2. Results of EDSA Experiments	74
4.4.3. Results of Transmission and Reflection Experiments	75
4.4.4. Results of Photoluminescence Experiments	80
4.5. Results of the Structural and Optical Characterization Experiments for Tl ₂ InGaS ₄ crystal	89
4.5.1. Results of X-Ray Experiments	90
4.5.2. Results of EDSA Experiments	91
4.5.3. Results of Transmission and Reflection Experiments	93
4.5.4. Results of Photoluminescence Experiments	97
4.6. Results of the Structural and Optical Characterization Experiments for Tl ₄ InGa ₃ S ₈ crystal	106
4.6.1. Results of X-Ray Experiments	106
4.6.2. Results of EDSA Experiments	108
4.6.3. Results of Transmission and Reflection Experiments	109
4.6.4. Results of Photoluminescence Experiments	113
5. CONCLUSION	121
REFERENCES	126
VITA	133

LIST OF TABLES

TABLES

2.1 The γ values of CdTe luminescence lines	29
4.1 X-ray powder diffraction data for $\text{Tl}_4\text{In}_3\text{GaSe}_8$ crystal	45
4.2 X-ray powder diffraction data for $\text{Tl}_4\text{InGa}_3\text{Se}_8$ crystal	59
4.3 X-ray powder diffraction data for $\text{Tl}_4\text{In}_3\text{GaS}_8$ crystal	73
4.4 X-ray powder diffraction data for $\text{Tl}_2\text{InGaS}_4$ crystals	90
4.5 X-ray powder diffraction data for $\text{Tl}_4\text{InGa}_3\text{S}_8$ crystals	106

LIST OF FIGURES

FIGURES

2.1 Dependence of the energy banding of allowed levels in diamond on the distance between the atoms [48]	9
2.2 Parabolic dependence of the energy on momentum	11
2.3 Energy versus momentum representation in a two level direct gap system	11
2.4 Energy versus momentum representation in a semiconductor having valleys at $k = \langle 000 \rangle$ and $k = \langle 111 \rangle$ directions	12
2.5 The effect of the defect levels on the energy structure of semiconductors	14
2.6 The configurational coordinate model for the band structure	17
2.7 Representation of X-ray diffraction by a crystal lattice	19
2.8 Electronic transitions in a PL experiment by excitation and recombination	25
2.9 Donor-acceptor pair transition and the effect of Coulomb interaction on emission energy	28
2.10 The configurational coordinate model for the band structure with permitted energy levels of ground and excited states [86]	33
3.1 A schematic representation of a typical scanning electron microscope	36
3.2 A schematic representation of a typical X-Ray diffraction experimental setup	37
3.3 Schematic representations of (a) transmission and (b) reflection experimental setups	38
3.4 A schematic representation of a typical PL experimental setup	39
3.5 The transmission spectrum of a typical bandpass filter	40

3.6 An example of deconvolution of the photoluminescence spectra into three Gaussian lineshapes	40
3.7 A simple representation of crystal growth by the Bridgman method	41
4.1 Projection of the unit cell of $\text{Tl}_4\text{In}_3\text{GaSe}_8$ crystal on the [001] plane. The figures indicate heights above this plane	43
4.2 X-ray diffraction pattern of $\text{Tl}_4\text{GaIn}_3\text{Se}_8$ powder sample	44
4.3 The result of EDSA experiment on $\text{Tl}_4\text{In}_3\text{GaSe}_8$ crystal	46
4.4 Dependence of absorption coefficient on photon energy for $\text{Tl}_4\text{In}_3\text{GaSe}_8$ crystal. Inset: Plot of $(\alpha h\nu)^{1/2}$ versus $h\nu$	47
4.5 PL spectra of $\text{Tl}_4\text{In}_3\text{GaSe}_8$ crystal as a function of excitation laser intensity at $T = 30$ K: (a) B-band, 0.0003-0.0873 W cm^{-2} excitation intensity range; (b) A- and B-bands, 0.0873-1.1777 W cm^{-2} excitation intensity range	49
4.6 Dependences of PL intensities at the emission band maxima versus excitation laser intensity at $T = 30$ K. The solid lines show the theoretical fits using equation 2.33	50
4.7 Temperature dependence of PL spectra from $\text{Tl}_4\text{In}_3\text{GaSe}_8$ crystals: (a) B-band, excitation laser intensity $L = 0.0557 \text{ W cm}^{-2}$; (b) A-band, excitation laser intensity $L = 1.1777 \text{ W cm}^{-2}$	52
4.8 Temperature dependence of PL band intensity for A- and B-bands. Circles and triangles are the experimental data and solid curves show the theoretical fit using equation 2.43	53
4.9 Proposed energy-level diagram of $\text{Tl}_4\text{In}_3\text{GaSe}_8$ at $T = 16$ K	54
4.10 Projection of structure of $\text{Tl}_4\text{InGa}_3\text{Se}_8$ and $\text{TlGaS}_2\text{-TlInS}_2$ crystals on (a) ac-plane and (b) ab-plane	57
4.11 X-ray diffraction pattern of $\text{Tl}_4\text{InGa}_3\text{Se}_8$ powder sample	58
4.12 Energy dispersive spectroscopic analysis of $\text{Tl}_4\text{InGa}_3\text{Se}_8$ crystal	60
4.13 The spectral dependence of transmittance and reflectivity for $\text{Tl}_4\text{InGa}_3\text{Se}_8$ crystal at $T = 300$ K	61
4.14 The variation of absorption coefficient as a function of photon energy at $T = 300$ K: the dependence of (a) $(\alpha h\nu)^{1/2}$ and (b) $(\alpha h\nu)^2$ on photon energy	62

4.15	The spectral dependence of transmission for $\text{Tl}_4\text{InGa}_3\text{Se}_8$ crystal in the temperature range of 10-300 K. Inset: the indirect band gap energy as a function of temperature. The solid line represents the fit using equation 2.10	63
4.16	The dependence of refractive index on the wavelength for $\text{Tl}_4\text{InGa}_3\text{Se}_8$ crystal. Inset: plot of $(n^2-1)^{-1}$ versus $(h\nu)^2$. The solid line represents the fit using equation 2.22	64
4.17	Temperature dependence of PL spectra from $\text{Tl}_4\text{InGa}_3\text{Se}_8$ crystals at excitation laser intensity of $L = 55.73 \text{ mW cm}^{-2}$	66
4.18	Temperature dependencies of PL band intensity for $\text{Tl}_4\text{InGa}_3\text{Se}_8$ crystal. Circles are the experimental data. Solid curve shows the theoretical fit using equation 2.40. Inset: temperature dependence of emission band peak energy	67
4.19	PL spectra of $\text{Tl}_4\text{InGa}_3\text{Se}_8$ crystal as a function of excitation laser intensity at $T = 20 \text{ K}$	68
4.20	Excitation laser intensity versus emission band peak energy at $T = 20 \text{ K}$. The dashed curve represents the theoretical fit using equation 2.36. Inset: dependence of PL intensity at the emission band maxima versus excitation laser intensity at $T = 20 \text{ K}$. The solid line shows the theoretical fit using equation 2.33	69
4.21	Proposed energy-level diagram of $\text{Tl}_4\text{InGa}_3\text{Se}_8$ at $T = 20 \text{ K}$	71
4.22	X-ray diffraction pattern of $\text{Tl}_4\text{In}_3\text{GaS}_8$ powder sample	72
4.23	Energy dispersive spectroscopic analysis of $\text{Tl}_4\text{In}_3\text{GaS}_8$ crystal	74
4.24	The spectral dependence of transmittance and reflectivity for $\text{Tl}_4\text{In}_3\text{GaS}_8$ crystal at $T = 300 \text{ K}$	75
4.25	The variation of absorption coefficient of $\text{Tl}_4\text{In}_3\text{GaS}_8$ crystal as a function of photon energy at $T = 300 \text{ K}$. Insets 1 and 2 represent the dependencies of $(ah\nu)^{1/2}$ and $(ah\nu)^2$ on photon energy, respectively	76
4.26	The spectral dependence of transmission for $\text{Tl}_4\text{In}_3\text{GaS}_8$ crystal in the temperature range of 10-300 K. Inset: the indirect band gap energy as a function of temperature. The solid line represents the fit using equation 2.10	77

4.27 The dependence of refractive index on the wavelength for $\text{Tl}_4\text{In}_3\text{GaS}_8$ crystal. Inset: plot of $(n^2-1)^{-1}$ versus $(h\nu)^2$. The solid line represents the fit using equation 2.22	78
4.28 PL spectra of $\text{Tl}_4\text{In}_3\text{GaS}_8$ crystal under excitation of 532 nm line of a continuous frequency-doubled YAG:Nd ³⁺ laser (solid curve) and 406 nm line of Hg-Xe arc lamp (dashed curve). Note that for dashed curve, intensities have been multiplied by a factor of 35	80
4.29 Temperature dependence of PL spectra from $\text{Tl}_4\text{GaIn}_3\text{S}_8$ crystals at excitation laser intensity $L = 183.0 \text{ mW cm}^{-2}$: (a) A- , B- and C-bands in the 26-43 K temperature range and 500-780 nm wavelength region; (b) B-band in the 36-130 K temperature range and 555-620 nm wavelength region	81
4.30 Temperature dependencies of emission A- , B- and C-band peak energies of $\text{Tl}_4\text{In}_3\text{GaS}_8$ crystal	82
4.31 Temperature dependencies of PL band intensities for $\text{Tl}_4\text{In}_3\text{GaS}_8$ crystal. Triangles, stars and circles are the experimental data. Solid curves show the theoretical fits using equation 2.40	83
4.32 PL spectra of $\text{Tl}_4\text{In}_3\text{GaS}_8$ crystal as a function of excitation intensity: (a) A- and C-bands at $T = 26 \text{ K}$; (b) B-band at $T = 50 \text{ K}$	84
4.33 Dependencies of PL intensities at the emission band maxima on the excitation intensities for $\text{Tl}_4\text{In}_3\text{GaS}_8$ crystal. The solid lines show the theoretical fits using equation 2.33	85
4.34 Band model (a) and configurational coordinate (CC) model (b) for $\text{Tl}_4\text{In}_3\text{GaS}_8$ crystal	87
4.35 X-ray diffraction pattern of a $\text{Tl}_2\text{InGaS}_4$ powder sample	89
4.36 Energy dispersive spectroscopic analysis of $\text{Tl}_2\text{InGaS}_4$ crystal	91
4.37 The spectral dependence of transmittance and reflectivity for $\text{Tl}_2\text{InGaS}_4$ crystal at $T = 300 \text{ K}$	92
4.38 The variation of absorption coefficient as a function of photon energy at $T = 300 \text{ K}$. Insets 1 and 2 represent the dependences of $(ah\nu)^{1/2}$ and $(ah\nu)^2$, respectively, on photon energy	93

4.39	The spectral dependence of transmittance for $\text{Tl}_2\text{InGaS}_4$ crystal in the temperature range 10-300 K. Inset: the indirect band gap energy as a function of temperature. The solid line represents the fit using equation 2.10. Experimental data (solid triangles) were taken from Ref. [103]	94
4.40	The dependence of refractive index on the wavelength for $\text{Tl}_2\text{InGaS}_4$ crystal. Inset: plot of $(n^2 - 1)^{-1}$ versus $(h\nu)^2$. The solid line represents the fit using equation 2.22	95
4.41	Temperature dependence of the PL spectra (B-band) from $\text{Tl}_2\text{InGaS}_4$ crystals in the 500-750 nm range. The excitation laser intensity is $L = 0.11 \text{ Wcm}^{-2}$	97
4.42	Temperature dependence of PL spectra (A- and C-bands) from $\text{Tl}_2\text{InGaS}_4$ crystals in the 475-800 nm range. The excitation laser intensity is $L = 56.36 \text{ Wcm}^{-2}$	98
4.43	Temperature dependencies of the A- B- and the C-emission band peak energies. The dotted lines are only guides for the eyes. Experimental data for C-band (solid triangles) were taken from Ref. [96]	98
4.44	Temperature dependencies of the PL intensities at the A- and B-emission bands maxima	99
4.45	PL spectra from $\text{Tl}_2\text{InGaS}_4$ crystals at $T = 15 \text{ K}$ versus excitation intensity: (a) $0.01 - 5.15 \text{ Wcm}^{-2}$, (b) $5.15 - 14.70 \text{ Wcm}^{-2}$, (c) $14.70 - 32.21 \text{ Wcm}^{-2}$, and (d) $32.21 - 100.34 \text{ Wcm}^{-2}$	101
4.46	Dependencies of PL intensities at the emission band maxima versus excitation laser intensity at $T = 15 \text{ K}$	102
4.47	(a) Band model and (b) configurational coordinate (CC) model of a $\text{Tl}_2\text{InGaS}_4$ crystal at $T = 15 \text{ K}$	103
4.48	X-ray diffraction pattern of $\text{Tl}_4\text{InGa}_3\text{S}_8$ powder sample	106
4.49	Energy dispersive spectroscopic analysis of $\text{Tl}_4\text{InGa}_3\text{S}_8$ crystal	107
4.50	The spectral dependence of transmittance and reflectivity for $\text{Tl}_4\text{InGa}_3\text{S}_8$ crystal at $T = 300 \text{ K}$	108
4.51	The variation of absorption coefficient as a function of photon energy at $T = 300 \text{ K}$. Insets 1 and 2 represent the dependences of $(ah\nu)^{1/2}$ and $(ah\nu)^2$ on photon energy, respectively	109

4.52	The spectral dependence of transmittance for $\text{Tl}_4\text{InGa}_3\text{S}_8$ crystal in the temperature range of 10-300 K. Inset: the indirect band gap energy as a function of temperature. The solid line represents the fit using equation 2.10	111
4.53	The dependence of refractive index on the wavelength for $\text{Tl}_4\text{InGa}_3\text{S}_8$ crystal. Inset: Plot of $(n^2-1)^{-1}$ versus $(h\nu)^2$. The solid line represents the fit using equation 2.22	111
4.54	Temperature dependence of PL spectra of $\text{Tl}_4\text{InGa}_3\text{S}_8$ crystal for above bandgap excitation with $\lambda_{\text{exc}} = 325$ nm at an excitation laser intensity of $L = 2476.4$ mW cm^{-2}	113
4.55	Temperature dependence of PL spectra of $\text{Tl}_4\text{InGa}_3\text{S}_8$ crystal for below bandgap excitation with $\lambda_{\text{exc}} = 532$ nm at an excitation laser intensity of $L = 429.7$ mW cm^{-2}	114
4.56	Temperature dependences of PL intensities at emission band maxima for A- and B-bands	115
4.57	Excitation laser intensity dependence of PL spectra of $\text{Tl}_4\text{InGa}_3\text{S}_8$ crystal for below bandgap excitation with $\lambda_{\text{exc}} = 532$ nm at $T = 80$ K. Inset: dependence of B-band PL intensity at the emission band maxima on the excitation laser intensity ($\lambda_{\text{exc}} = 532$ nm)	117
4.58	Proposed band model for $\text{Tl}_4\text{InGa}_3\text{S}_8$ crystal	118

CHAPTER 1

INTRODUCTION

Since the earliest times, luminescence phenomena have existed and been observed in many different forms. The first publication on the luminescent man-made material entitled “De Phoenomenis in Orbe Lunae Novi Telescopii Usu” was written by La Galla in the year of 1612 [1,2]. Later, when elemental phosphorous was discovered in 1669 by Henning Brand, a new term “phosphor” was coined, meaning any “microcrystalline solid luminescent material”, to distinguish it from the elemental phosphorous [2]. Because of its long lasting glow, long-lived luminescence exhibited by the Bolognian stone became known as “phosphorescence” [2]. It was Eilhard Wiedemann to introduce the term “luminescence” to include all light emission not caused solely by a temperature rise, including both fluorescence (short-lived luminescence) and phosphorescence in 1888 [2,3].

The 19th century led to the categorization of the various types of luminescence which was developed to differentiate between the various luminescent excitation methods [2]. By this categorization, the luminescence which results from chemical reactions was labeled as chemiluminescence. To describe the type of chemiluminescence from living things, which is exactly what caused the light emission from the fireflies and glowworms, the term bioluminescence was used. The cause of light emission from thermal excitation was named thermoluminescence. The light generated by using an electric field was called electroluminescence. Radioluminescence had three types: cathodoluminescence (light generated by

electron bombardment), anodoluminescence (excitation by anode rays), and luminescence from γ - and X-rays [2, 4]. Finally, as we come to the process of creating light from a material excited by photons, it was labeled as photoluminescence (PL).

Today, PL spectroscopy is a very widely used technique to study the defect structures of semiconductors. The reason for this is mainly that PL represents a very suitable contactless, nondestructive and sensitive method to probe the defect levels inside forbidden band gap.

The chalcogens are the elements belonging to group VI of the periodic table. Chalcogenides are the compounds that contain at least one chalcogen element. However, in general, when talking about chalcogenides, the oxides (O) are usually excluded as they are far more common and are really their own special class of compounds. This means that the chalcogenides are basically sulphides (S), selenides (Se) and tellurides (Te).

Ternary thallium chalcogenides TlInSe_2 , TlGaSe_2 , TlInS_2 and TlGaS_2 have been studied extensively in recent years [5-9]. These crystals are very important in view of their possible technological applications in optoelectronic devices as a candidate material for optical devices and also for the understanding of their basic physics. This importance mainly comes from their wide transparency range and high photosensitivity in the visible range of spectra.

Changing the compositional parameter x in the formulas of $\text{TlIn}_x\text{Ga}_{1-x}\text{Se}_2$ and $\text{TlIn}_x\text{Ga}_{1-x}\text{S}_2$ crystals over a range from 1 to 0 results in materials with various physical properties. For $\text{TlIn}_x\text{Ga}_{1-x}\text{Se}_2$, changing the value of x from 1 to 0 in an order results in TlInSe_2 ($x = 1$), $\text{Tl}_4\text{In}_3\text{GaSe}_8$ ($x = 0.75$), $\text{Tl}_2\text{InGaSe}_4$ ($x = 0.50$), $\text{Tl}_4\text{InGa}_3\text{Se}_8$ ($x = 0.25$), and TlGaSe_2 ($x = 0$) crystals. Doing the same for $\text{TlIn}_x\text{Ga}_{1-x}\text{S}_2$ results in TlInS_2 ($x = 1$), $\text{Tl}_4\text{In}_3\text{GaS}_8$ ($x = 0.75$), $\text{Tl}_2\text{InGaS}_4$ ($x = 0.50$), $\text{Tl}_4\text{InGa}_3\text{S}_8$ ($x = 0.25$), and TlGaS_2 ($x = 0$) crystals, in the same manner. Among these crystals, TlInSe_2 , TlGaSe_2 , TlInS_2 and TlGaS_2 are referred as the main crystals, which all the others are made of.

If we look at the structures of these four main crystals, TlInSe_2 crystal belongs to a group of semiconductors with the chain structure of the crystal lattice and is analog of thallium selenide ($\text{Tl}^{1+} \text{TI}^{3+} \text{Se}_2$) in which trivalent TI^{3+} ions are replaced with In^{3+} [10]. As we come to the remaining TlGaS_2 , TlInS_2 and TlGaSe_2

crystals, these crystals belong to the monoclinic system, and their space group is C2/c at room temperature. The lattice structure of these crystals is composed of two-dimensional alternating layers arranged parallel to the (001) plane; each layer is followed by another layer rotated by 90^0 with respect to the previous layer. A more detailed analysis for the structures of the remaining crystals not mentioned above will be given in the sections related to crystals' structures in chapter 4.

The photoelectric and optical properties of TlInSe₂ crystals were studied in Ref. D3–8. The fundamental absorption edge is formed by indirect and direct transitions with $E_{gi} = 1.07\text{--}1.23$ eV and $E_{gd} = 1.27\text{--}1.44$ eV, respectively [11-13]. Among the useful properties of TlInSe₂ crystals are negative differential resistance with S-type current–voltage characteristics [11] and high thermoelectric power [14]. Recently, band structure calculations have been reported for isostructural TlInSe₂, TlInTe₂ and TlGaTe₂ chain crystals [15-18]. For the latter crystal, from an angle-resolved photoemission study, a strong temperature-dependent shift of the Fermi level was ascertained [18].

TlGaSe₂ crystal has a high photosensitivity in the visible range of spectra. High birefringence in conjunction with a wide transparency range of 0.6-16 μm makes this crystal especially useful for optoelectronic applications [19]. Optical and photoelectrical properties of TlGaSe₂ crystals were studied in Ref. [9, 20-23]. It was established that the fundamental absorption edge is formed by indirect and direct transitions with $E_{gi} = 1.97$ and $E_{gd} = 2.27$ at $T = 300$ K, respectively. The temperature coefficient of the indirect band gap energy (dE_{gi}/dT) was found to be -3.8×10^{-4} eV K^{-1} [21].

The interest in the optical properties of TlInS₂ has been extensive especially in the last 10 years. The electrical and the optical properties of this ternary thallium chalcogenide have recently become the subject of vast research [24-30]. A high photosensitivity in the visible range of the spectrum, a high birefringence, and a wide transparency range of 0.5–14 μm make this crystal useful for optoelectronic applications [19]. Besides these, both infrared reflection spectroscopy [31, 32] and Raman scattering [33] from TlInS₂ have been studied as a function of temperature. A number of PL bands have been observed at 1.8 K in TlInS₂ single crystals. They were attributed to the radiative recombination of free and bound excitons [34]. In Ref. 35, the PL bands due to excitons have been observed in the temperature range

5.5–100 K. Temperature dependencies of the intensities of these bands were interpreted by a variation in the crystal structure and the coexistence of several polytypes. The forbidden gap of TlInS_2 was measured by both absorption and reflection spectroscopy as a function of temperature and was found $E_{\text{gi}} = 2.27$ and $E_{\text{gd}} = 2.49$ eV at $T = 300$ K, respectively. The temperature and excitation dependencies of radiative excitonic recombination in $\text{TlIn}_x\text{Ga}_{1-x}\text{S}_2$ layered crystals have been also investigated and analysed, where no luminescence was observed below $x = 0.8$ [36].

TlGaS_2 crystal has an indirect band gap of about 2.46 eV at room temperature [37]. The existence of a fine structure in the PL spectra of a TlGaS_2 in the temperature range 1.8-77 K has been reported [38]. It was found that the PL lines in the long-wavelength part of the spectrum (595-610 nm) were separated by $\cong 0.5$ eV from the direct edge exciton absorption peak and were due to recombination of bound excitons. Two broad emission bands in PL spectra of TlGaS_2 at $T = 6$ K due to impurity level-to band radiative transitions at 499 and 590 nm have been observed [39]. The impurity levels of TlGaS_2 crystals in the temperature range 90-350 K have been investigated by thermally stimulated current and photoinduced current transient spectroscopy techniques [28]. The activation energies of the observed four peaks were found to be 0.18, 0.23, 0.36 and 0.66 eV. It was established that the fundamental absorption edge is formed by indirect and direct transitions with $E_{\text{gi}} = 2.49$ and $E_{\text{gd}} = 2.67$ eV at $T = 300$ K, respectively. Besides, some of the electrical and optical properties of TlGaS_2 crystals have also been investigated in Ref. 24, 25.

In addition to these four main crystals, the physical properties of $\text{Tl}_2\text{InGaSe}_4$ and $\text{Tl}_2\text{InGaS}_4$ crystals were also investigated to some extent. For $\text{Tl}_2\text{InGaSe}_4$ crystals, there are only a few studies on the physical properties, namely photoconductivity data [40], Raman spectra [41], optical absorption spectra and temperature dependence of the band gap [42]. It was established that the fundamental absorption edge is formed by indirect and direct transitions with $E_{\text{gi}} = 1.86$ and $E_{\text{gd}} = 2.04$ eV at $T = 300$ K, respectively [43]. When we come to $\text{Tl}_2\text{InGaS}_4$ crystals formed in the $\text{TlIn}_x\text{Ga}_{1-x}\text{Se}_2$ and $\text{TlIn}_x\text{Ga}_{1-x}\text{S}_2$ system, it has been reported that these crystals have indirect band gap of $E_{\text{gi}} = 2.27$ eV and direct band gap of $E_{\text{gd}} = 2.49$ eV at $T = 300$ K, respectively.

As seen from the above survey, layered and chain structured chalcogenides $\text{TlIn}_x\text{Ga}_{1-x}\text{Se}_2$ and $\text{TlIn}_x\text{Ga}_{1-x}\text{S}_2$ attract much interest due to their possible

technological applications in optoelectronic devices in the visible region of the spectrum. For the most part, optoelectronic properties of these materials are dominated by defects of various types and the interactions between them. In this regard, detailed information on the defect levels is very useful for the fabrication of high-quality devices. It is worthwhile to note that most of the work done on these semiconductors has concentrated on the near band edge emission and only a little amount of data exists on shallow and deep PL bands with emission energies below the band gaps of these semiconductors. Particularly, the low-temperature PL spectra of some members of $\text{TlIn}_x\text{Ga}_{1-x}\text{Se}_2$ and $\text{TlIn}_x\text{Ga}_{1-x}\text{S}_2$ crystal systems, namely TlInS_2 , TlGaS_2 , TlGaSe_2 and $\text{Tl}_2\text{InGaSe}_4$ layered crystals, have recently been investigated by some researchers in the 500–860 nm wavelength region and 10–300 K temperature range at different laser excitation intensities [44–47]. The experimentally observed bands in emission spectra were attributed to donor-acceptor pair recombination processes. In spite of the experimental and theoretical efforts devoted to the study on these materials, the optical properties of some members of the $\text{TlIn}_x\text{Ga}_{1-x}\text{Se}_2$ and $\text{TlIn}_x\text{Ga}_{1-x}\text{S}_2$ crystal systems, namely $\text{Tl}_4\text{In}_3\text{GaSe}_8$, $\text{Tl}_4\text{InGa}_3\text{Se}_8$, $\text{Tl}_4\text{In}_3\text{GaS}_8$, $\text{Tl}_2\text{InGaS}_4$ and $\text{Tl}_4\text{InGa}_3\text{S}_8$, have not been studied yet. Therefore, both experimental data and the overall theoretical understanding of them lack a coherent and complete framework for the crystal systems studied.

The main purpose of the present thesis is to report and discuss the results of the PL study on the chain and layered $\text{Tl}_4\text{In}_3\text{GaSe}_8$, $\text{Tl}_4\text{InGa}_3\text{Se}_8$, $\text{Tl}_4\text{In}_3\text{GaS}_8$, $\text{Tl}_2\text{InGaS}_4$, and $\text{Tl}_4\text{InGa}_3\text{S}_8$ selenides and sulfides comprising spectra with emission bands having energies lower than the forbidden band gap, which are related to the shallow and deep defect levels originating from stacking faults induced during the crystal growth and/or uncontrolled impurities. In order to complete the analysis thoroughly, the temperature and excitation power dependent behaviors of PL band intensities and energies have been studied in detail. Besides, for extending the characterization of these crystals, we also present the results of the transmission and reflection experiments (to determine band gap energies and their temperature dependences in a wide range), X-ray experiments (to calculate the lattice parameters), and energy dispersive spectroscopic analysis (EDSA) experiments (to obtain the compositional parameters), as a complementary work.

In line with above purpose, chapter 2 deals with the theoretical bases of these four characterization experiments (PL, transmission-reflection, X-ray and EDSA). In

chapter 3, we describe the experimental systems and the methods governing these experiments to inform the reader. In chapter 4, the results of all experiments are presented, compared and discussed in detail. Finally, in chapter 5, we will make the physical interpretations and conclusions on the results of the experiments done on the crystals studied.

CHAPTER 2

THEORETICAL APPROACH

2.1 Introduction

In this chapter, the basic theoretical knowledge needed for structural and optical characterization of $\text{TlIn}_x\text{Ga}_{1-x}\text{Se}_2$ and $\text{TlIn}_x\text{Ga}_{1-x}\text{S}_2$ crystal systems will be the main subject. Knowing that the optical properties of the semiconductors are directly related to the transitions between various states, it is very reasonable first to sketch how the collection of atoms into an array results in formation of bands consisting of infinitely many allowed states and how these bands are separated by an energy gap. While doing this, we will mainly concentrate on some states having special importance, namely impurity states. After that, some theoretical background for the experiments done to reveal structural properties (X-ray and energy dispersive spectral analysis experiments) and optical properties (transmission-reflection and PL experiments) of the crystals will also be given.

2.2 Theoretical Approach to the Band Structure in Semiconductors

2.2.1 Introduction

In this section, a picture to explain the basic properties of the energy bands in solids and semiconductors will be drawn. First, the structure of the bands in perfect semiconductors will be explained. After that the structure of the energy bands in real semiconductors will be described by introducing the concept of impurity and its effects on the band structure. Then, the configurational coordinate model related to the dynamic lattice structure will be introduced, and finally, the dependence of the band gap of semiconductors on temperature will be discussed.

2.2.2 Band Structure in Perfect Semiconductors

To get an understanding about the nature of the semiconductors, we must first understand what happens when the atoms are brought together to form solids. When two atoms approach to each other, the wave functions of their electrons begin to overlap. According to Pauli's exclusion principle, no two electrons may occupy the same quantum state simultaneously. So, as a result of this bringing together process, all spin-paired electron states gain energies, which are slightly different from the energies they have in the original isolated atom. Thus, if we have N number of atoms brought together, we can say that $2N$ electrons of the same orbital occupy $2N$ different states. So, instead of a discrete energy level, the bands consisting of some number of states very close to each other are created.

The energy distribution of these states depends strongly on the distance between the atoms. This dependence for a collection of carbon atoms is shown in figure 2.1. Here it is worth noticing that some of the lower energy states ($2S$) join the band of higher energy states ($2P$). As a result of this joining, the lower band has as many states as the number of electrons. This lower band is called as valence band and it is completely filled with electrons, whereas the upper band is called as conduction band and it contains no electrons. From these characteristics, we can see that although the conduction band can carry a current under influence of an electric field, the valence band cannot, because it is completely filled.

When the separation between the atoms is nearly equal to the lattice constant in crystal structures, we see that a gap is created between valence and conduction band, called as energy gap. It is obvious that, because there are no allowed energy states in the gap, we do not expect to find any electrons in the solid structure having energies in the range of this gap (for this reason sometimes energy gap is referred as forbidden energy gap). Depending on the size of the energy gap and the relative availability of the electrons, the solid is a conductor, semiconductor or insulator.

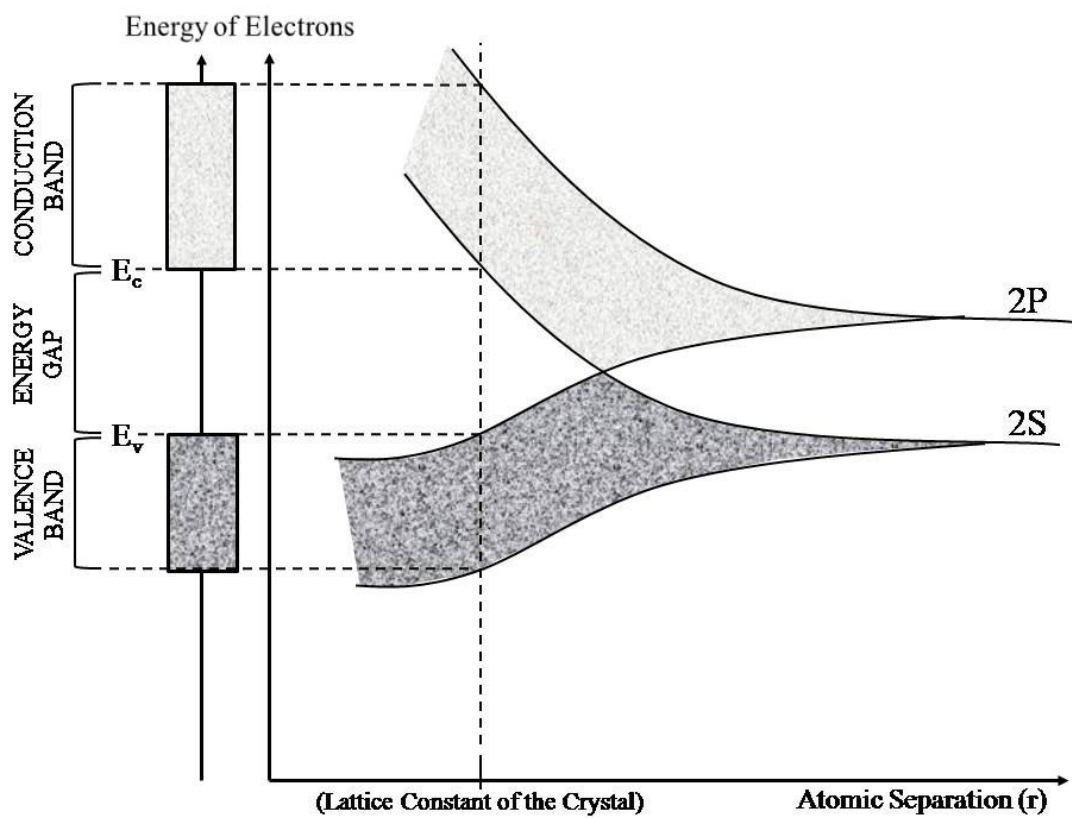


Figure 2.1. Dependence of the energy banding of allowed levels in diamond on the distance between the atoms [48]

In a conductor, conduction band is populated with electrons far above the energy gap and the electron concentration is around 10^{23} cm^{-3} . In a semiconductor, however, the value of the energy gap is around 3 eV and the electron concentration is about 10^{20} cm^{-3} . Finally, in an insulator, the value of the energy gap is usually larger than 3 eV and there is a very negligible electron concentration in the upper band. So, it is rather

obvious that the value of the energy gap in solid structures has a very special importance for it determines the type of the solid.

Now that we have seen the distribution of allowed energy states in position space, we can do the same for momentum space. Momentum space considerations are also very important, since both energy and momentum conservation must be satisfied in an optical transition processes.

The kinetic energy E of an electron is related to its momentum P by the relation

$$E = \frac{P^2}{2m^*}, \quad (2.1)$$

where m^* is the effective mass of the electron. Again, from quantum mechanics, we have

$$\vec{P} = \frac{h\vec{k}}{2\pi}, \quad (2.2)$$

where h is the Planck's constant and \vec{k} is the wave vector. Because the momentum is basically dependent on \vec{k} , it is reasonable to call \vec{k} as the momentum vector. The kinetic energy of the electron then can be expressed as

$$E = \frac{h^2 k^2}{2m^*}. \quad (2.3)$$

If we take the crystal as a square well potential with an infinite barrier and a bottom of width L , then k can be found as

$$k = \frac{n\pi}{L}, \quad (2.4)$$

where n is an arbitrary nonzero integer. If we assume the crystal has a cube shape whose sides has length L , the allowed energies are clearly

$$E = \frac{h^2 n^2}{2m^* L^2} = \frac{h^2}{2m^* L^2} (n_x^2 + n_y^2 + n_z^2). \quad (2.5)$$

Here, E seems to be discrete being dependent on n values. However, because the difference of E values corresponding to each value of n are so small that E actually appears to be quasi-continuous (E values differ from each other with an order of 10^{-18} eV for a volume of 1 cm^3 of a material).

In figure 2.2, the parabolic dependence of E on k is represented with the minimum of the parabola at $k=0$. Such a distribution of states in momentum space is called a parabolic valley and the energy gap is called as direct (E_{gd}). In momentum

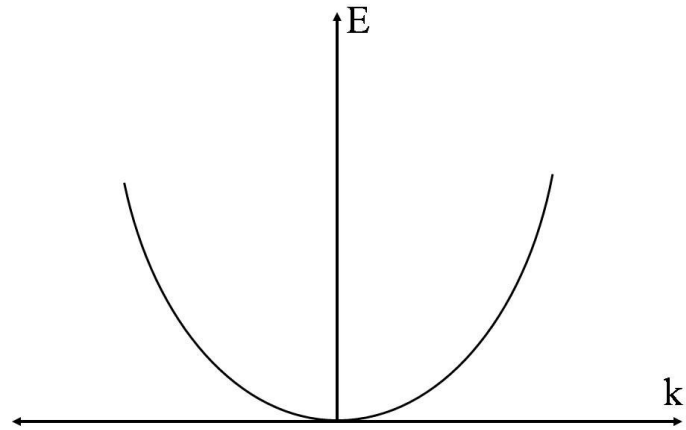


Figure 2.2. Parabolic dependence of the energy on momentum

space representations, usually the top of the valence band is taken as the reference level. Then bottom of the conduction band is placed on the level, which has the value of the energy gap. The placement of valence and conduction bands is shown in figure 2.3.

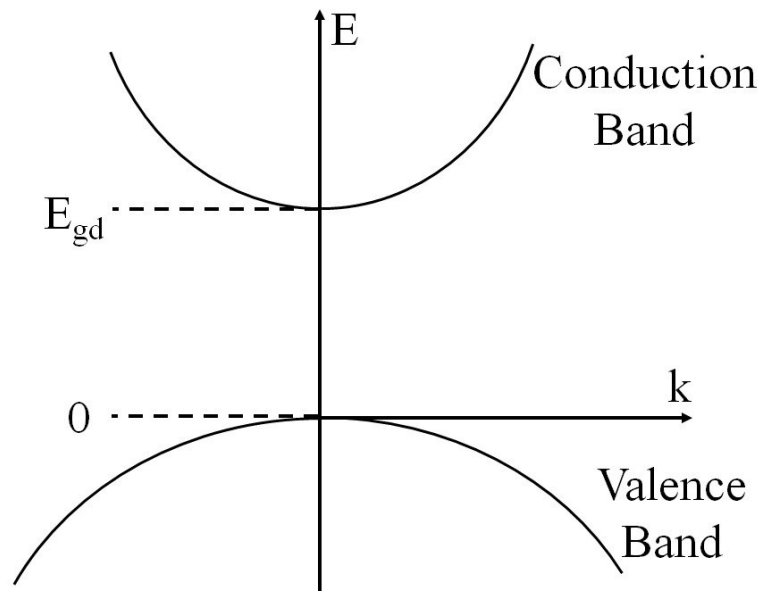


Figure 2.3. Energy versus momentum representation in a two level direct gap system

Besides these, we know that the separation between the nearest atoms varies in each direction in the crystal, so there will be valleys having different energy band

structures corresponding to several directions. Furthermore, in addition to the effects of the nearest neighbors, we can also take the effects of the next-nearest neighbors and all the higher order neighbors into account. As a result of these, it is understandable that there is a possibility of the minimum of the valley not to occur where $k = 0$ but at some other point corresponding to any other crystallographic direction. This time the energy gap is called as indirect (E_{gi}). The pictorial representation of this condition is shown in figure 2.4.

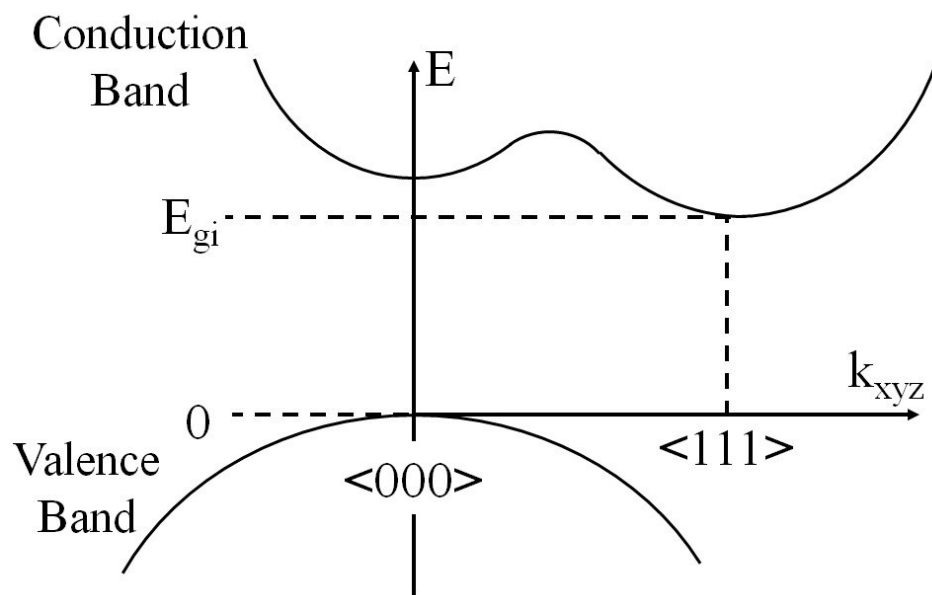


Figure 2.4. Energy versus momentum representation in a semiconductor having valleys at $k = \langle 000 \rangle$ and $k = \langle 111 \rangle$ directions

As a result of the discussion above, we conclude that the representation in figure 2.4 can be used as a complete representation of the band structures in semiconductors, since it involves all basic properties of the bands, including energy values and band shapes.

2.2.3 Impurities and Band Structure in Real Semiconductors

So far, we have discussed the band structure in perfect semiconductors, which are composed of only the same type of the atoms or molecules. But in real life, it is almost impossible to produce such a semiconductor, because there will always be some environmental effects that will allow other elements than you want to enter the composition of the semiconductor, which change the material's structure. Such foreign elements are called impurities.

Impurities have very important role in semiconductors. The presence of impurity atoms in semiconductors determines most of the practical applications of semiconductors [49]. An impurity atom produces several types of interactions when introduced in a lattice. If the impurity atom replaces one of the constituent atoms of the crystal and provides crystal with one or more additional electrons than the atom it replaces, it is called as a donor. The excess electron or electrons have weak bonds. If the impurity atom replaces one of the constituent atoms of the crystal and provides crystal with fewer electrons than the atom it replaces, it is called an acceptor. A missing electron due to impurity is considered as a hole. A hole or holes have also weak bounds and behave as the localized state. An example of donor can be Te atoms on As-site of GaAs crystal. Likewise, an example for an acceptor can be Zn atoms on Ga-site of GaAs crystal.

The impurities may sometimes locate themselves in an interstitial position, instead of replacing constituent atoms of the crystal, which causes another type of impurity. In such a condition, the impurity is always considered as a donor, since its outer-shell electrons are available for conduction. In addition to this, the opposite is also true where a missing atom in the crystal structure may also act like an impurity. In this case, if the missing atom deprives the crystal of one or more electrons, it is considered to be an acceptor. It is very common that interstitial impurities combine to form a molecular impurity, which may be either donor (impurity) or an acceptor (vacancy).

Now that we have the basic information about impurities, we can look at what they do the band structure in semiconductors. Actually, we can say that impurities change band structure by adding new defect levels placed in the forbidden energy gap of the semiconductor. The energy values of these new bands are

determined by knowing that the electron of a donor is essentially free when it is in the conduction band. So the energy level of a donor is thought to be one ionization or binding energy below the conduction band. A similar interpretation can also be made for an acceptor level. We can say that the energy level of an acceptor is thought to be one ionization or binding energy above the valence band. A simple pictorial represent of the effect of defect levels on the energy states of a semiconductor is shown in figure 2.5. It is rather understandable that the impurity may contribute more than one carrier to semiconductor (either electrons or holes). In this case, it is called as a multiple donor or acceptor.

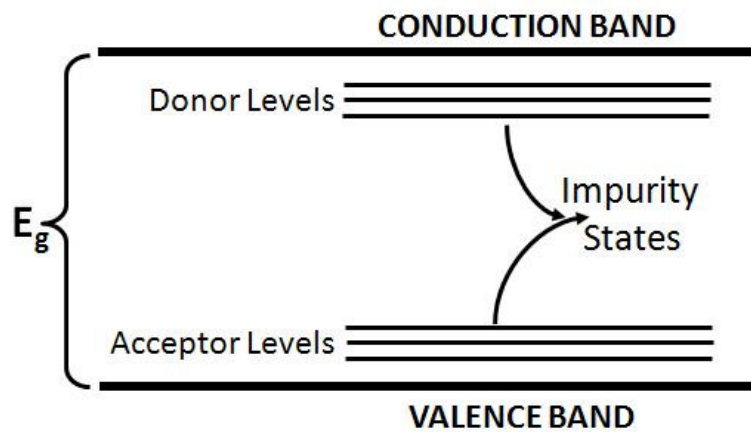


Figure 2.5. The effect of the defect levels on the energy structure of semiconductors

Inside the crystal structure, donors and acceptors can form pairs that can act as stationary molecules that are embedded in the crystal. When a neutral donor and neutral acceptor come closer to each other, it is most likely that the donor's excess electron becomes increasingly shared by the acceptor. This means that the donor and acceptor become more ionized when brought together, which results in lowering of their binding energies. If they become almost fully ionized, binding energies become nearly zero and the corresponding levels become very close to the bands' edges. For such donor-acceptor pairs, the amount of change in their energy levels as isolated impurities is directly the coulomb interaction energy, which can be written as

$$\Delta E = \frac{q^2}{\epsilon r}, \quad (2.6)$$

where q is the charge of the electron, ϵ is the dielectric constant of the medium and r is the donor-acceptor pair separation. So the pair separation energy is

$$E_{\text{pair}} = E_g + E_D - E_A + \frac{q^2}{\epsilon r}, \quad (2.7)$$

where E_g is the band gap energy of the crystal and E_D and E_A are activation energies of donor and acceptor as isolated impurities.

2.2.4 Configurational Coordinate Model for Band Structure

So far, we based our discussions on the assumption that the optical centers responsible for the emission were embedded in a static lattice structure and are fixed at equilibrium positions. However, in real semiconductors, the centers are parts of a vibrating lattice and the environment has a dynamic structure. This means that the neighboring atoms can vibrate about some average positions and these vibrations can affect the electronic states of the atom. Furthermore, the changes in the electronic structure of the atom can also affect the electronic structure of the neighboring atoms, thus forcing them to adopt new average positions. The nature of the vibrations about the new average positions may also be different from their initial electronic states and the shapes of the bands are strongly affected. To account for such a dynamic case, we have to introduce the configurational coordinate model, which has been used for many years to give a qualitative description of the optical processes in luminescent centers. This model is based on two basic approximations:

(i) The first approximation is called as adiabatic approximation, introduced by Born and Oppenheimer [50]. It is based on the consideration that atoms move very slowly in comparison to the valence electrons. Therefore, the electronic motion occurs at a given nuclear coordinate and it is not significantly affected by the changes in the positions of atoms. This approximation is very reasonable, since the nuclei are much heavier than the electrons by 10^3 to 10^5 times and therefore they move much slower. By adiabatic approximation, it is accepted that the nuclear and electronic motions are independent of each other.

(ii) The second approximation is to decrease the number of vibrational modes to only one mode from many possible modes, for simplicity. This single (ideal) mode is usually called as breathing mode in which the neighboring atoms pulsate radially in or out about central atom. Therefore, we only need one nuclear coordinate, called

as configurational coordinate, which corresponds to the distance between the central atom and the neighboring atom. However, it is known that there are many vibrational modes in the crystal. Even so, the idea of having only one mode is still acceptable, since the configuration coordinate can still represent the average amplitude of a linear combination of several modes.

With adiabatic and one-coordinate dynamic center approximations, the solution of the Schrödinger equation leads the ground (initial) and excited (final) state potential energy curves [51], as diagrammatically represented in figure 2.6. Such a diagram is called as configurational coordinate diagram. In the diagram, the solid curves represent interatomic interaction potential energy, while two different points Q_0 and Q'_0 represent equilibrium positions for initial (*i*) and final (*f*) states, respectively. This difference between equilibrium points of ground and excited states is expected since the spatial distributions of an electron orbital for ground and excited states are different from each other. In the excited state, the orbital is more spread out and has less curvature which means that the energy of such an electron orbital depends less on the configuration coordinate. From the figure, it is also seen that the nucleus of the atom stays approximately at the same position throughout the emission process due to its relatively heavier mass, as mentioned before.

The optical absorption starts from the equilibrium position of the ground state. The probability to lose energy by emitting light is at most 10^9 s^{-1} , whereas the probability for an excited electron to lose energy by generating lattice vibration is 10^{12} to 10^{13} s^{-1} [52]. So, it is clear that an electron at state *B* relaxes very fast to the equilibrium position at state *C* before it can emit light. After relaxation, it emits light by the transition from state *C* to state *D* and again relaxes to state *A*, completing a cycle. In this case, the energies of the emitted photons are smaller than that of the absorbed ones due to the transfer of energy to lattice vibrations, which is called as the Stokes shift.

When two configurational coordinate curves intersect with each other, an electron in the excited state can cross the intersection assisted by thermal energy and can reach the ground state nonradiatively. In this case, the model suggests a sudden decrease in luminescence efficiency of a center at elevated temperatures. It is shown by Gurney and Mott [53] that given enough thermal energy E_Q , an electron in the excited state *C* may reach a point *E* and makes the transition to the ground state *A* nonradiatively. In such a case, a photon may not be emitted and the thermal

quenching of the PL spectra may be observed. Furthermore, it is also possible that if the equilibrium position of the excited state C is located outside the configurational coordinate curve of the ground state, the excited state can intersect the ground state while relaxing from B to C , resulting in a nonradiative process.

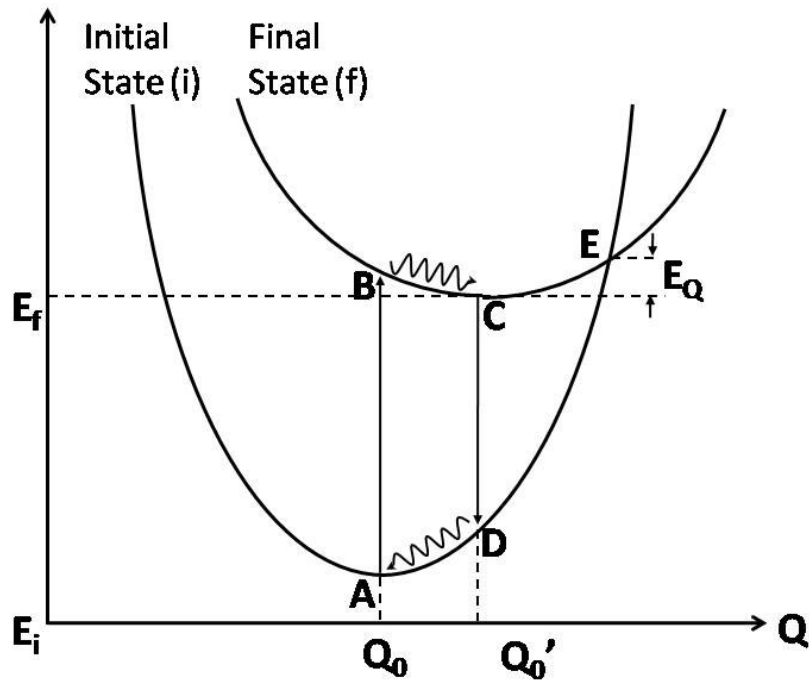


Figure 2.6. The configurational coordinate model for the band structure

Finally, the last significant property of the configurational coordinate model is that the width (generally taken as the full width at half maxima (FWHM)) of the emission spectra of simple systems satisfies the following relation [54],

$$W = W_0 \left[\coth \left(\frac{h\nu_e}{2k_B T} \right) \right]^{\frac{1}{2}}, \quad (2.8)$$

where W_0 is a constant whose value is equal to W as the temperature approaches to 0 K, k_B is the Boltzmann constant and $h\nu_e$ is the energy of the vibrational mode of the excited state. The experimental data for absorption in various alkali halides were found to fit this expression quite well [55].

2.2.5 Effect of Temperature on Band Gap Energy

The effect of temperature on semiconductor structures is a very important concern, since the changes in the structure are directly related to the band structure of the material. An increase in the temperature of a semiconductor causes expansion of the lattice structure and, as a result, an increase in the oscillations of the atoms around their equilibrium lattice points. In addition to the shift of the band edges due to thermal expansion, the increase in the oscillations also results in broadening of the energy levels.

The temperature dependence of the band gap energy for a semiconductor can be expressed in two main parts as,

$$\frac{dE_g}{dT} = \left(\frac{dE_g}{dT} \right)_P + \left(\frac{dE_g}{dT} \right)_{\text{eff}}, \quad (2.9)$$

where the first term is the result of the thermal expansion of the lattice and the second term is from electron-phonon interaction. The first term in the expression may be either positive or negative depending on the band structure of the semiconductor material, whereas the second term is always negative for all semiconductors. Therefore, overall dependence of the band gap of the material on temperature may be either negative or positive depending on the term that contributes more. For Ge, Si and A³B⁵ type materials, it is well-known that the first term is negative. So, the overall behavior of the band gap is a decreasing behavior with increasing temperature. However, for the lead chalcogenides like PbSe, PbS and PbTe, the first term is positive and more contributing term. So, overall behavior of the band gap is an increasing behavior as temperature increases.

Furthermore, the temperature dependence of the bandgap energy for many semiconductors has been defined by [56],

$$E_g(T) = E_g(0) + \frac{\gamma T^2}{(T + \beta)}, \quad (2.10)$$

where $E_g(0)$ is the value of the bandgap at $T = 0$ K, γ is an empirical constant and β is approximately the Debye temperature. It has been also proved that the experimental data for diamond, Si, Ge, 6H SiC, GaAs, InP and InAs were satisfactorily represented by this equation except that the values of β differed markedly from the Debye temperatures [56]. More recent experiments on GaAs and GaP revealed that

the above equation fits successfully to the experimental data with the β values very close to the Debye temperatures over a wide temperature range [57].

To sum up, in most of the semiconductors, the band gap energy of the material decreases with increasing temperature. However, as previously mentioned, the lead chalcogenides are exceptional materials where an increase in the band gap energy with increasing temperature is observed.

2.3 Theoretical Approach to Characterization Experiments

2.3.1 X-Ray Diffraction Experiments

X-rays are a form of electromagnetic radiation having energies between 100 eV and 100 keV (around 10^{-10} m). Only short wavelength X-rays (hard X-rays) in the range of a few angstroms to 0.1 angstrom (1 keV - 120 keV) are used for diffraction experiments due to the fact that the wavelength of these X-rays are comparable to the size of atoms. For this reason, they are ideally suited for investigating the structural arrangement of atoms and molecules for most of materials.

When X-rays are sent to a material, they collide with electrons of atoms and some of them are deflected away from the direction where they originally travel. If the collisions between incident X-rays and the electrons are elastic, the scattered X-rays will have the same wavelengths as the incident ones. These are the X-rays we measure in diffraction experiments, since these scattered X-rays carry information about the atom distribution in materials.

The diffracted X-rays from different atoms can interfere with each other and the resultant intensity distribution is mainly modulated by this interaction. In the case of crystal atoms arranged in a periodic fashion, the diffracted waves will consist of sharp interference maxima depending on the distribution of atoms. Measuring the diffraction pattern, therefore, allows us to reveal the distribution of atoms in a material. In figure 2.7, the deflection of incident X-rays are shown.

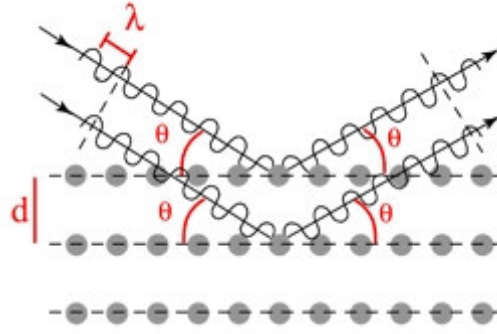


Figure 2.7. Representation of X-ray diffraction by a crystal lattice

The properties of the diffracted X-rays by a lattice plane were studied by Bragg in his paper titled “The Reflection of X-rays by Crystals”, published in 1913 [58]. There, he stated the famous expression named after him,

$$n \lambda = 2 d \sin \theta , \quad (2.11)$$

where n is an integer representing the order of diffraction, λ is the wavelength of the X-rays, θ is the half of the deviation angle of the diffracted X-rays and d is the spacing between the planes in the crystal structure. In addition, the interplanar spacing d can be expressed in most general form by

$$\begin{aligned} \frac{1}{d_{hkl}^2} = & \frac{1}{[1 + 2\cos(\alpha)\cos(\beta)\cos(\gamma) - \cos^2(\alpha) - \cos^2(\beta) - \cos^2(\gamma)]} \\ & \times \left[\frac{h^2 \sin^2(\alpha)}{a^2} + \frac{k^2 \sin^2(\beta)}{b^2} + \frac{l^2 \sin^2(\gamma)}{c^2} \right. \\ & + \frac{2hk}{ab} (\cos(\alpha)\cos(\beta) - \cos(\gamma)) + \frac{2kl}{bc} (\cos(\beta)\cos(\gamma) - \cos(\alpha)) \\ & \left. + \frac{2lh}{ac} (\cos(\gamma)\cos(\alpha) - \cos(\beta)) \right] \quad (2.12) \end{aligned}$$

where a , b and c are lattice constants, h , k and l are the Miller indices and α , β , and γ are the angles for the lattice structure.

2.3.2 Energy Dispersive Spectral Analysis (EDSA) Experiments

Energy dispersive spectral analysis (EDSA, also called EDXA for energy dispersive X-ray analysis) is a predominantly used analytical tool that employs scanning electron microscopy (SEM) for chemical microanalysis. It is a well-known fact that SEM has the capability to provide information both on the surface of the material

and about the composition of the region near the surface of the material. EDSA technique is used in conjunction with SEM and is not a surface science technique.

EDSA is a type of spectroscopy and it includes the investigation of a material through interactions between electrons and the material. It is based on the following physical principles. When an electron beam is scanned across the surface of the material, i.e., a material is bombarded with an electron beam, different interactions occur between the electron beam and the sample. Normally, an atom within the sample contains unexcited electrons situated in shells around the nucleus. However, the incident beam excites an electron in an inner shell, resulting in its ejection and the formation of a hole within the atom's electronic structure. Then, an electron from the outer shell having higher-energy fills this hole. As a result of this process, the excess energy of the electron is emitted from the atom as an X-ray. Collecting these X-rays by measuring their numbers and energies creates spectral lines that are highly specific to individual elements. Since every element has distinctly unique energy levels, each element produces characteristic X-rays, which makes it possible to determine the elemental composition of the sample by analyzing the spectra. Besides these, the amount of each element present in the material can also be determined from the relative counts of the detected X-rays.

In EDSA experiments, the electron beam sent to the material has typically the energy of 5 to 20 keV, for the reason being that the energy holding electrons in atoms (the binding energy) ranges from a few eV up to many keV. Emitted X-rays are generated in a region about 2 microns in depth, which is the reason why EDSA is not accepted as a surface science technique. EDSA can be used to investigate elements which have atomic number greater than 11 (Na). The reason for this inconvenience is that the X-ray detector (Si-Li) is often protected by a Beryllium window which prevents the detection of elements with an atomic number of below 11 due to the absorption of the soft X-rays. However, elements having an atomic number as low as 4 (Be) can be detected by systems without protection windows. EDSA can detect most of the natural elements in concentrations as low as 0.1 percent, depending on the material type.

2.3.3 Transmission and Reflection Experiments

Transmission and reflection spectroscopy, commonly referred to as spectrophotometry, is an analytical technique based on measuring the amount of light transmitted or reflected by a material at a certain wavelength. This technique can be used for solid, liquid, and gas sampling. In transmission and reflection experiments, the light beams are sent to the material. As light beams enter the material, some are absorbed, some are reflected from the surface and some pass through the material. After these processes, the ratio of the intensity of the transmitted light or reflected light to the intensity of the incident light is measured. The resulting spectrum, which depends on the thickness, absorption coefficient and reflectivity of the material, can then be analyzed to reveal several optical properties of the material.

Absorption of light by a semiconductor occurs when the energy of the incoming light wave is equal to or higher than the band gap energy of the material. In absorption process, energy of the incoming light is transferred to the electrons in the material structure. The damping characteristic of light in the material is defined by [49]

$$\frac{I(x)}{I(0)} = \exp(-\alpha x) , \quad (2.13)$$

where $I(0)$ is the intensity of the incident light, $I(x)$ is the intensity of the light after propagating a distance x through the material and α is the absorption coefficient, which is defined as

$$\alpha = \frac{4\pi k}{\lambda} , \quad (2.14)$$

where λ is the wavelength of the light wave and k is the absorption index of the material. Because of the nature of the process, the absorption coefficient can also basically be related to the transition probabilities between the electronic energy levels in the material. By using the transition probability between the valence and conduction bands, found by the help of the perturbation theory, the dependence of the absorption coefficient on photon energy and band gap energy for semiconductors is found in the simplest form as [59],

$$(\alpha h\nu) = A (h\nu - E_g)^p , \quad (2.15)$$

where A is a constant that mainly depends on the transition probability and p is an index which characterizes the optical absorption process, and it is theoretically equal to 2 and 1/2 for indirect and direct allowed transitions, respectively.

The second main process taking place in the material structure is reflection. In reflection process, the incoming light is reemitted by the material on the same side, as a reflected light wave. The reflection coefficient is defined as the ratio of the intensity of the reflected wave to that of incident wave. For normal incidence of light, the reflection coefficient for a material is given by [49],

$$R = \frac{(n - 1)^2 + k^2}{(n + 1)^2 + k^2}, \quad (2.16)$$

where n is the refractive index of the material. When $k = 0$, the refractive index becomes completely real and the material becomes transparent. In this case the reflection coefficient becomes

$$R = \frac{(n - 1)^2}{(n + 1)^2}. \quad (2.17)$$

The last main process taking place in the material structure is transmission. In transmission process, the incoming light is reemitted by the material on the opposite side, as a transmitted light wave. The transmission coefficient is defined as the ratio of the intensity of the transmitted wave to that of incident wave. In general, the transmission coefficient for a material is given by [49]

$$T = \frac{(1 - R)^2 \exp(-\alpha x)}{1 - R^2 \exp(-2\alpha x)}. \quad (2.18)$$

Here, it is easy to notice that when the product αx is very large, the second term in the denominator can be neglected and T becomes

$$T \cong (1 - R)^2 \exp(-\alpha x). \quad (2.19)$$

Knowing R and x , equation 2.18 can be solved for α . Even when R is not known, with the appropriate measurement of transmittance of two samples with different thicknesses, the equation

$$\frac{T_1}{T_2} \cong \exp \{-\alpha(x_1 - x_2)\}, \quad (2.20)$$

where x_1 and x_2 are the thicknesses of two samples, can be used to find α .

Further, if the refractive index n is known, the determination of thickness of the thin sample can be done by using transmission interference fringes at

wavelengths slightly longer than the intrinsic absorption edge, where the sample has relatively high transmission values by using the equation

$$x = \frac{1}{2n} \left(\frac{\lambda_1 \lambda_2}{\lambda_1 - \lambda_2} \right), \quad (2.21)$$

where λ_1 and λ_2 are the positions of the two nearest peaks.

In addition to all these considerations above, one can also analyze the refractive index dispersion data in $h\nu < E_g$ range according to the single-effective-oscillator model proposed by Wemple and DiDomenico [60, 61] to find some optical constants of the material. In single-effective-oscillator model, the refractive index is related to the photon energy by

$$n^2(h\nu) = 1 + \frac{E_{so}E_d}{E_{so}^2 - (h\nu)^2}, \quad (2.22)$$

where E_{so} is the energy of the single effective dispersion oscillator and E_d is the dispersion energy. According to the equation 2.22, plotting $(n^2 - 1)^{-1}$ versus $(h\nu)^2$ graph allows one to determine the oscillator parameters E_{so} and E_d by fitting a linear function to the lower energy data range. Moreover, the zero-frequency refractive index n_0 at zero photon energy can also be estimated by using

$$n_0^2 = 1 + \frac{E_d}{E_{so}}, \quad (2.23)$$

which is derived from equation 2.22. To a close approximation, the oscillator energy E_{so} is an ‘average’ energy gap and it is associated empirically with the lowest direct band gap E_{gd} of the material through the relationship $E_{so} \cong 2.0 E_{gd}$ [62-66]. The single-effective-oscillator model was successfully applied to the experimental data for TlGaSe₂ and TlGaS₂ layered crystals [67, 68].

In addition to these, the refractive index n can also be analyzed to determine the oscillator strength S_{so} for the material. The refractive index can be represented by a single Sellmeier oscillator at low energies by [69]

$$\frac{(n_0^2 - 1)}{(n^2 - 1)} = 1 - \left(\frac{\lambda_{so}}{\lambda} \right)^2, \quad (2.24)$$

where λ_{so} is the oscillator wavelength. Rearranging equation 2.24 results in [63]

$$(n^2 - 1)^{-1} = \frac{1}{S_{so}\lambda_{so}^2} - \frac{1}{S_{so}\lambda^2}, \quad (2.25)$$

where S_{so} can be expressed as

$$S_{so} = \frac{(n_0^2 - 1)}{\lambda_{so}^2}, \quad (2.26)$$

By using these relations, we can also calculate the oscillator strength S_{so} and oscillator wavelength λ_{so} , easily.

2.3.4 Photoluminescence Experiments

2.3.4.1 Introduction

As mentioned before, the PL experiment is the most common method to probe into the material structure. The spectral content of the result of the PL experiment is a direct measure of various important material properties.

In a PL experiment, photo-excitation causes electrons within the material to move into permissible excited states. When these electrons return to their equilibrium states, the excess energy is released and may include the emission of light (a radiative process) or may not (a nonradiative process). The energy of the emitted light or PL is related to the difference in energy levels between the two electron states involved in the transition that is, between the excited state and the equilibrium state. The quantity of the emitted light is related to the relative contribution of the radiative process.

Therefore, in a PL experiment, firstly electron-hole pairs are excited (figure 2.8.A). Then before they recombine radiatively, they reach a quasi-thermal equilibrium among themselves which lasts much shorter than the recombination process. Thus a PL process involves three steps [70]:

- (i) Excitation step, where electron-hole pairs are excited by an external energy source.
- (ii) Thermalization step, where excited pairs relax towards quasi-thermal equilibrium distributions.
- (iii) Recombination step, where the thermalized pairs recombine radiatively to produce emission.

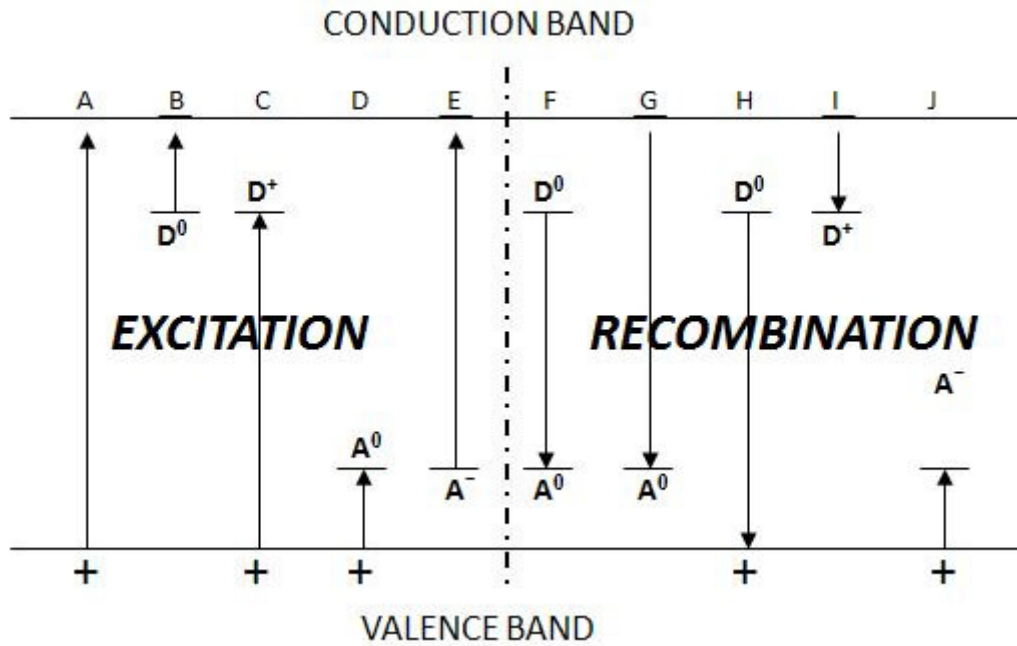


Figure 2.8. Electronic transitions in a PL experiment by excitation and recombination

The most important step among these is the recombination step, since the spectra from the experiment is directly related to the recombination mechanisms involved in the emission process. In the following section, we will deal with the possible recombination mechanisms one might encounter during the experiments.

2.3.4.2 Recombination Mechanisms

Three types of optical transitions that may take place in a semiconductor when it is energized by some external means are band-to-band transitions, free-to-bound transitions and donor-acceptor pair transitions [70].

2.3.4.2.a. Band-to-Band Transitions

These types of transitions, involving free holes and free electrons, are sometimes called free-to-free transitions. In a perfect semiconductor, e-h pairs will thermalize and accumulate at the conduction band and valence band extrema where they tend to recombine. The rate of emission is given by the equation [49]

$$R = n_i n_f P, \quad (2.27)$$

where n_i and n_f are the initial and final densities of states, and P is the probability that 1 carrier/cm³ at the higher energy will make a radiative transition into 1 vacancy/cm³ in the lower state. This probability is proportional to the absorption coefficient.

In a semiconductor having a direct band gap, the recombination of electron-hole pairs occurs radiatively with a high probability. So in such a semiconductor, like GaAs, recombination transition is vertical and radiated photon energy is given by the equation:

$$h\nu = E_f - E_i, \quad (2.28)$$

where E_f and E_i are the final and initial state energies, respectively. In indirect band gap semiconductors, like Si and Ge, electron-hole pairs can recombine via phonon assisted transitions, and the emitted photon has the energy given by the equation:

$$h\nu = E_f - E_i \pm h\Omega, \quad (2.29)$$

where $h\Omega$ is the energy of phonon and the + and - signs correspond to phonon emission or absorption, respectively. As easily seen from above formula, phonon emission can shift the band-to-band spectrum to lower energies.

2.3.4.2.b. Free-to-Bound Transitions

Band-to-band transitions dominate at high temperatures where all impurities are ionized, but at low temperatures, the carriers become frozen on impurities. As an example, we can consider a p -type sample which contains N_A acceptors per unit volume. If we do a PL experiment on this sample, we see that at low photoexcitation, the density of free electrons forming in the conduction band is much smaller than N_A . These electrons can recombine with the holes trapped on the acceptors radiatively or nonradiatively (figure 2.8.G). Transitions like this, which involves a free carrier (an electron in our case) and a charge which is bound to an impurity (a hole in our case), are called as free-to-bound transitions. In such transitions, the energy of the emitted photon is given by $E_G - E_A$, where E_A is the acceptor activation energy.

2.3.4.2.c. Donor-Acceptor Pair Transitions

Semiconductors quite often contain both donors and acceptors. In such semiconductors, under equilibrium conditions, some of the electrons from donors are captured (or compensated) by the acceptors. For this reason, such semiconductors are called as compensated. They contain both ionized donors (D^+) and acceptors (A^-). Electrons and holes can be formed in the conduction and valence bands, respectively, by optical excitation (figure 2.8.A). Then these carriers can be trapped at D^+ and A^- sites and they produce neutral donors (D^0) and acceptors (A^0). In returning the equilibrium, some of the electrons on neutral donors will recombine radiatively with the holes on the neutral acceptors (figure 2.8.F). Such a process is called as donor-acceptor pair transition (DAP). This transition can be represented by

$$D^0 + A^0 = h\nu + D^+ + A^- . \quad (2.30)$$

The photon emitted in such a transition has the energy

$$h\nu = E_G - E_D - E_A , \quad (2.31)$$

where E_G is the band gap energy of the sample, E_D is the activation energy of the donors and E_A is the activation energy of the acceptors as isolated impurities. But in this equation, we see that the Coulomb interaction between ionized donors and acceptors is neglected. So taking the Coulomb interaction into account, our equation becomes

$$h\nu = E_G - E_D - E_A + \frac{q^2}{\epsilon r} , \quad (2.32)$$

where ϵ is the static dielectric constant and r is the distance between ionized donor and acceptor (figure 2.9).

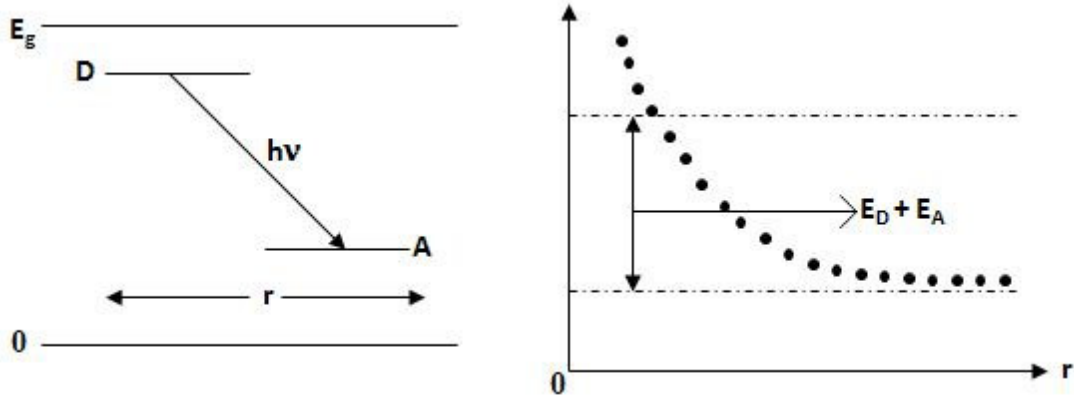


Figure 2.9. Donor-acceptor pair transition and the effect of Coulomb interaction on emission energy

2.3.4.3 Laser Excitation Power Dependence of the Peak Intensity and the Peak Energy of the Photoluminescence Spectra on Semiconductors

As the power of the excitation light source is changed, the variation of PL intensity depending on this power can be used to identify the underlying recombination process [71]. It has been found experimentally that the luminescence intensity I of the PL emission lines is proportional to L^γ , which can be expressed as

$$I \propto L^\gamma, \quad (2.33)$$

where L is the power of the exciting laser radiation and γ is a constant whose value is, between 1 and 2 ($1 < \gamma < 2$) for exciton like transitions and smaller than 1 ($\gamma < 1$) for free-to-bound and donor-acceptor pair transitions [72-75]. The results of some of the experiments on the dependence of the PL intensity on the laser excitation power are shown in table 2.1 [76]. From the table, it is seen that equation 2.33 holds well for several emission lines of CdTe.

In addition to the dependence of the peak intensities on laser excitation power, it is also very important to investigate the dependence of the peak energies on laser excitation power to learn more about the recombination mechanisms in the material that cause emission. In PL experiments, it is generally observed that the emission band peak shifts to higher energies when the laser excitation intensity is

Table 2.1. The γ values of CdTe luminescence lines

	FE	D^0X	A^0X	hD^0	eA^0	D^0A^0	Power Range (W cm^{-2})
Ref. 37	1.2	1.4	1.3		0.7		0.003 – 0.3
Ref. 37	1.0	1.1	1.1	0.7	0.6		0.3-6
Ref. 34	1.25		1.25	1.03			0.001-1
Ref. 33	1.1	1.5	1.5, 1.7		1-1.1		
Ref. 35	1.3	1.4	1.4			0.76	0.4-10

increased. Several attempts were made to formulate this behavior. One of these attempts was done by M. I. Nathan and T. N. Morgan [77], explaining the dependence of the emission band peak energy shift on excitation laser intensity as

$$L(\nu) = L_0 \exp\left(\frac{h\nu}{E_0}\right), \quad (2.34)$$

where $h\nu$ is the peak energy maximum of the PL band, L_0 is a constant and E_0 is a coefficient which depends on the compensation of the sample. The coefficient E_0 becomes very small in non-compensated samples, where there is no shift in emission band peak.

Another attempt was made by D. G. Thomas *et al.* [78] on the dependence of the shift in PL band peak on the laser excitation intensity for GaP sample. In this attempt, laser excitation intensity versus PL band peak energy graph was plotted in logarithmic scale. On this graph, they tried to fit a straight line to the widely scattered experimental data points. However, it has been found that there is an obvious deviation of the experimental data from a straight line [79], which was also observed by P. J. Dean and J. L. Merz in their work for ZnSe sample [80].

The final attempt to derive an analytical expression for the dependence of the peak energy of the PL band on laser excitation intensity was made by E. Zacks and A. Halperin [81]. They considered a sample with dielectric constant ϵ and with donor and acceptor concentrations N_D and N_A , respectively. They also considered one of these concentrations in minority and the other is in majority and made the assumption that the temperature of the crystal is so low that thermal ionization of the

impurities is negligible. Any pair recombination will leave an ionized donor-acceptor pair of separation with the distance of a nearest neighbor pair. Excitation process produces free charge carriers, which are eventually get captured by ionized impurities and turn them back to the neutral state. The light intensity, which is emitted by the recombination of donor-acceptor pairs, should be proportional to the concentration of neutral minority impurities, to the number of majority impurities in the volume element, and to the rate of the pair recombination. On continuous excitation, a steady state will be reached, when the rate of the generation of neutral pairs will just be equal to the rate of their recombination. A given intensity of the exciting light will produce a constant flux of free carriers at steady-state. With these assumptions, the recombination rate is given by a good approximation as

$$W(r) = W_0 \exp\left(\frac{-2r}{R_B}\right), \quad (2.35)$$

where W_0 is a constant, r is the pair separation distance and R_B is the shallow impurity Bohr radius. Then, by using the capture cross sections for pairs, they obtained the expression for L as

$$L = D \frac{(h\nu_m - h\nu_\infty)^3}{h\nu_B + h\nu_\infty - 2h\nu_m} \exp\left(-\frac{2(h\nu_B - h\nu_\infty)}{h\nu_m - h\nu_\infty}\right), \quad (2.36)$$

where $h\nu_B$ is the emitted photon energy of a close donor-acceptor pair separated by R_B , $h\nu_\infty$ is the emitted photon energy of an infinitely distant donor-acceptor pair and $h\nu_m$ is the emission energy of band maxima, respectively. There are three free parameters in equation 2.36, which are D , $h\nu_B$ and $h\nu_\infty$. Here D is a proportionality factor and for this reason its calculated values are not important in physical interpretations. The other two parameters $h\nu_B$ and $h\nu_\infty$, however, have special importance while interpreting the experimental results. Here it should also be noted that as seen from the equation 2.35 the band maximum shifts to higher energies with increasing laser excitation intensity, as expected.

2.3.4.4 Temperature Dependence of the Peak Intensity and the Peak Energy of the Photoluminescence Spectra on Semiconductors

The dependence of the PL spectra on temperature provides a very important understanding of the nature of the emission processes occurring in the material

structure and has been used to obtain information about electronic energy levels in various semiconductors. The changes in the intensities of the band peaks of the luminescence spectra with respect to increasing temperature can be analyzed to explain the origin of the luminescent optical centers in the crystal.

It is found that different processes contribute to the decrease of PL band peak intensity with increasing temperature. When temperature of a material is increased, the most probable situation is the thermal activation of a nonradiative transition channel, decreasing the luminescence efficiency, and thus the band peak intensity. In general, if we assume the probability of the radiative transitions is independent of temperature, the efficiency of the luminescence emission can be expressed in the simplest form as [49]

$$\eta = \frac{P_r}{P_r + P_{nr}}, \quad (2.37)$$

where P_r and P_{nr} are the probabilities for a radiative and nonradiative transitions, respectively. The nonradiative transition probability P_{nr} has temperature dependence [49]

$$P_{nr} = P_{nr0} \exp\left(-\frac{E_t}{k_B T}\right), \quad (2.38)$$

where P_{nr0} is a coefficient independent of the temperature and E_t is the thermal activation energy. As a result, the dependence of the luminescence efficiency on temperature can be expressed as [49]

$$\eta = \frac{1}{1 + C \exp\left(-\frac{E_t}{k_B T}\right)}, \quad (2.39)$$

where C is a constant whose value equals the ratio of the nonradiative transition probability to the radiative one. In addition, the same model can be used to express the temperature dependence of the band peak intensity in the same manner as

$$I = \frac{I_0}{1 + \alpha \exp\left(-\frac{E_t}{k_B T}\right)}, \quad (2.40)$$

where I_0 is proportionality constant and α is the process rate parameter. However, it is noticed that this equation does not fit the experimental data over a large temperature range, especially for the low temperature part. To manage this situation a better fitting function was introduced [82] as

$$I = \frac{I_0}{1 + \sum_n \alpha_n \exp\left(-\frac{E_{tn}}{k_B T}\right)}, \quad (2.41)$$

where the integer n corresponds to the number of the thermal quenching processes and E_{tn} are the thermal activation energies of the electronic energy levels. If the result of a nonlinear fit of equation 2.40 to the experimental data is not satisfying, equation 2.41 gives us the freedom to choose the number of the activation energies for a better fit. However, in general, it has been seen that the equation 2.41 rewritten with $n = 2$ as

$$I = \frac{I_0}{1 + \alpha_1 \exp\left(-\frac{E_{t1}}{k_B T}\right) + \alpha_2 \exp\left(-\frac{E_{t2}}{k_B T}\right)} \quad (2.42)$$

fits well enough to the experimental data for most of the cases. Here, it should be noted that the parameter E_{t1} corresponds to the activation energy at low temperatures, whereas E_{t2} corresponds to the activation energy at high temperatures. In fact, it has been found that E_{t1} is dominant for the temperature values around $T \cong 5 - 60$ K and E_{t2} is dominant for $T > 60$ K [83-85].

Another significant property of the PL spectra is the dependence of the positions of the emission band maxima on temperature. Actually, the position of a band maximum directly corresponds to the PL emission energy, which is the energy of a photon emitted by an electron making transition between two energy levels. Therefore, the shifts of the emission band maxima with increasing temperature can be directly related to the changes in the band structure of the material.

Most generally, an increase in the temperature of a semiconductor causes expansion of the lattice structure, as mentioned in section 2.2.5. Therefore, as a result of the thermal expansion of the lattice structure, the band gap of the semiconductor decreases. Along with the decrease of the band gap, it is very reasonable to expect that the energy levels in the band gap region gets closer to each other and the energy difference between them decreases. This decrease results in the shift of emission band maxima, which corresponds to the energy of the emitted photon, towards lower energies.

In contrast to the above discussion, it is also possible to observe a shift in emission band maxima towards higher energies. Such a behavior is generally explained within the framework of configurational coordinate model, mentioned in section 2.2.4. To observe the temperature-dependent behavior of the emission band

peak energy, the configurational coordinate model is redrawn in figure 2.10, with permitted discrete energy levels of ground and excited states (horizontal lines). According to this model, only the lowest levels of the excited state are occupied at low temperatures [86]. Therefore, in such a situation only transitions from the lowest

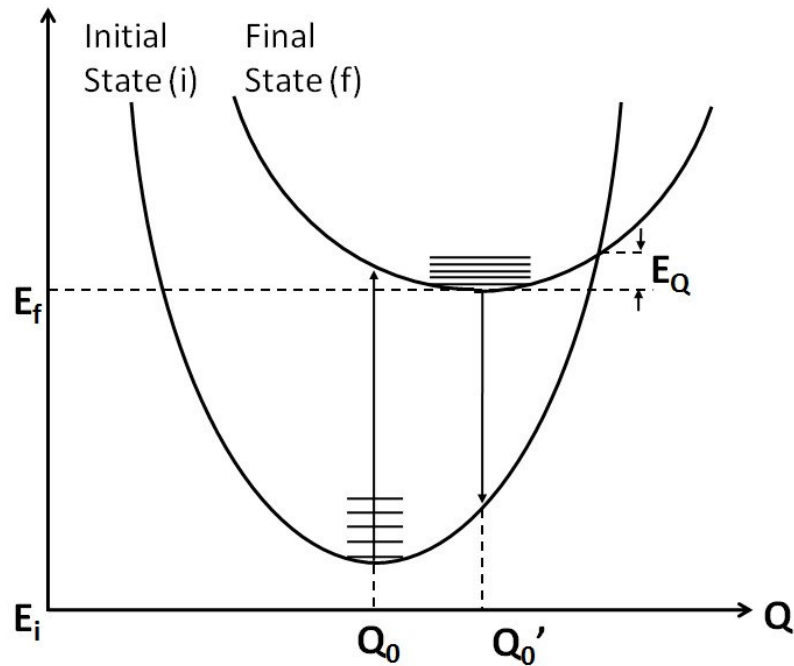


Figure 2.10. The configurational coordinate model for the band structure with permitted energy levels of ground and excited states [86].

level of the excited state to the ground state are possible. As a result, the high energy extent of the emission process is limited. But when the temperature is increased, higher energy levels of the excited state starts to be occupied by electrons [86]. This process gives the electrons a possibility to make transitions from higher energy levels of the excited state to the ground state. The electrons making transitions from higher energy levels of the excited state have obviously more energy to emit as a photon. Besides, as we go higher among the energy levels of the excited state, the number of electrons that can occupy the state increases significantly. This means that the rate of the transitions from an upper level in the excited state to the ground state is much higher than the rate of the transitions from the bottom of the excited state to the ground state. As a consequence of all these, the increasing temperature results in

occupation of higher energy levels in the excited state with increasing number of electrons. A large number of electrons make transitions from the higher energy levels of the excited state to the ground state by emitting high energetic photons. So, the high energy part of the spectra becomes more dominant than low energy part, causing a shift of emission band maxima towards higher energies.

CHAPTER 3

EXPERIMENTAL SETUPS AND TECHNIQUES USED IN THE EXPERIMENTS

3.1 Introduction

In this chapter, all of the experimental setups and techniques used in structural and optical characterization experiments in the scope of this dissertation will be given in detail, since they are a measure of the significance of the experimental results. In addition to the general information, some particular properties of the experimental devices will also be given.

3.2 Energy Dispersive Spectral Analysis Experiments

The EDSA experiments were used to determine the chemical composition of the samples. As mentioned before, this technique employs SEM for chemical microanalysis. In the experiments, a “JEOL JSM-6400” scanning electron microscope equipped with secondary and backscattered electron detectors was used. The diagram that belongs to the experimental setup is shown in figure 3.1. The EDSA experiments were done in 0-10 keV range. The analyses of the experimental results were done with a “NORAN System6 X-ray Microanalysis System” and “Semafore Digitizer”, which are the original equipments of the device. As a result of the analyses, the atomic composition ratios of the investigated samples were found.

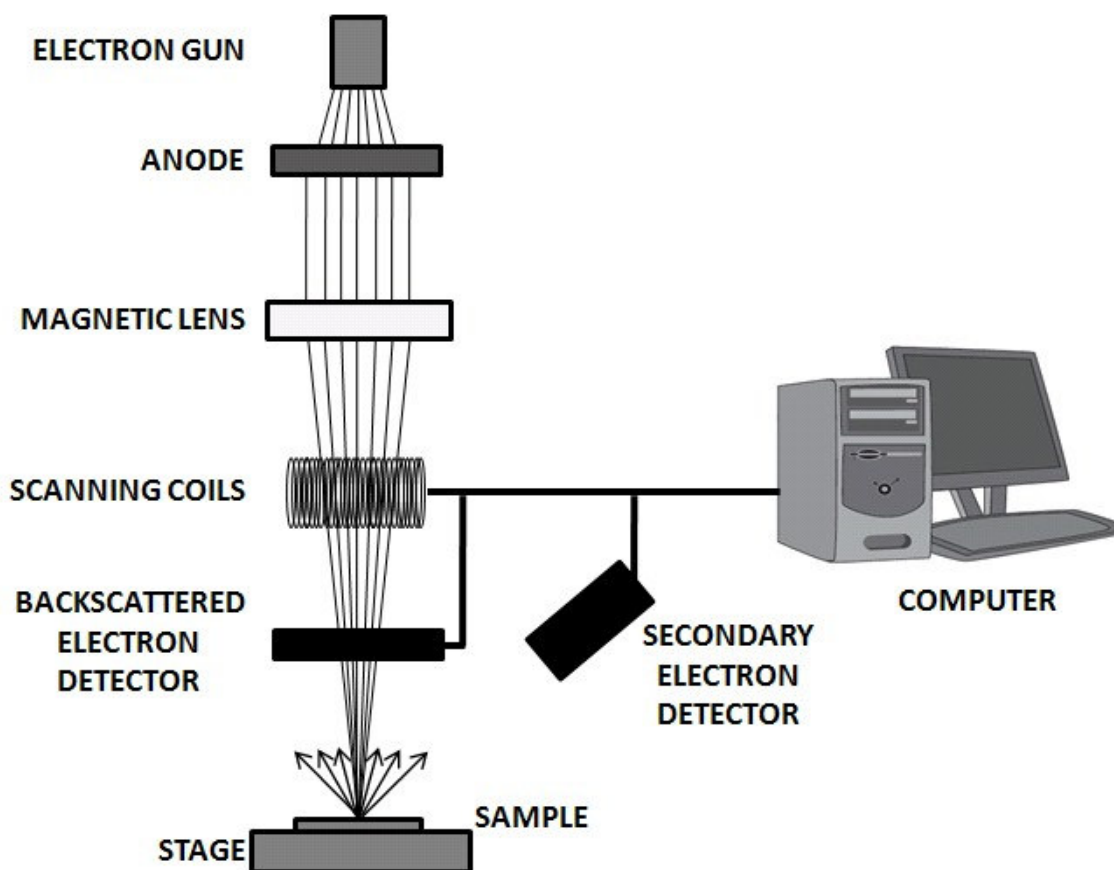


Figure 3.1. A schematic representation of a typical scanning electron microscope

3.3 X-Ray Diffraction Experiments

The structural parameters of the samples used in this study were revealed by X-Ray diffraction experiments. In the experiments, a “Rigaku Miniflex” diffractometer with CuK_α radiation having a wavelength of $\lambda = 0.154049$ nm was used in the $10\text{-}70^\circ$ diffraction angle (2θ) range at a scanning speed of $0.02^\circ \text{ s}^{-1}$. A schematic representation for a typical experimental setup for X-ray diffraction experiments is shown in figure 3.2. The analyses of the experimental data were done by using a least-squares computer program “DICVOL 04”. As the results of the analyses, the lattice parameters of the unit cells for the samples were found.

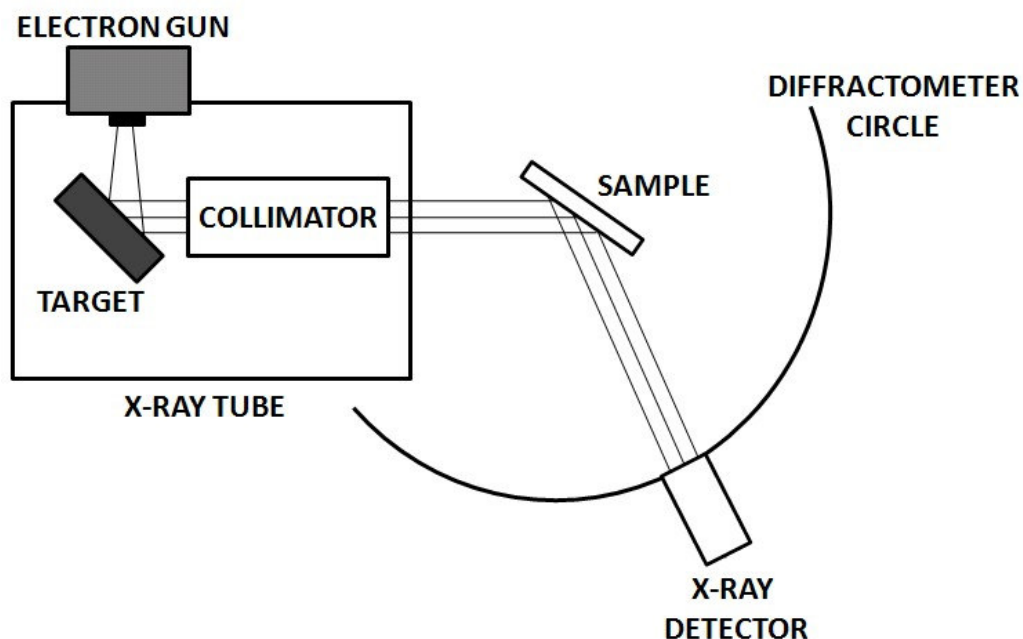


Figure 3.2. A schematic representation of a typical X-Ray diffraction experimental setup

3.4 Transmission and Reflection Experiments

The transmission and reflection experiments were done in the 400-1100 nm wavelength region with a “Shimadzu UV-1201” model spectrophotometer by using a 20 W halogen lamp, a holographic grating, and a silicon photodiode. A schematic representation for a typical experimental setup for transmission and reflection experiments is shown in figure 3.3. The resolution of the spectrophotometer was 5 nm. In addition, the experiments in 900-1200 nm range were done by using a “Bruker Equinox 55” model Fourier Transform Infrared (FTIR) spectrometer. The transmission measurements were carried out under normal incidence of light with polarization direction along the (001) plane, which is perpendicular to the *c*-axis of the crystals. For room temperature reflection experiments, a specular reflectance measurement attachment with 5° incident angle was used. In addition to these, for the temperature dependent measurements, an “Advanced Research Systems, Model CSW-202” closed-cycle helium cryostat was used to cool the sample from room temperature down to 10 K, and the temperature was controlled within an accuracy of ± 0.5 K.

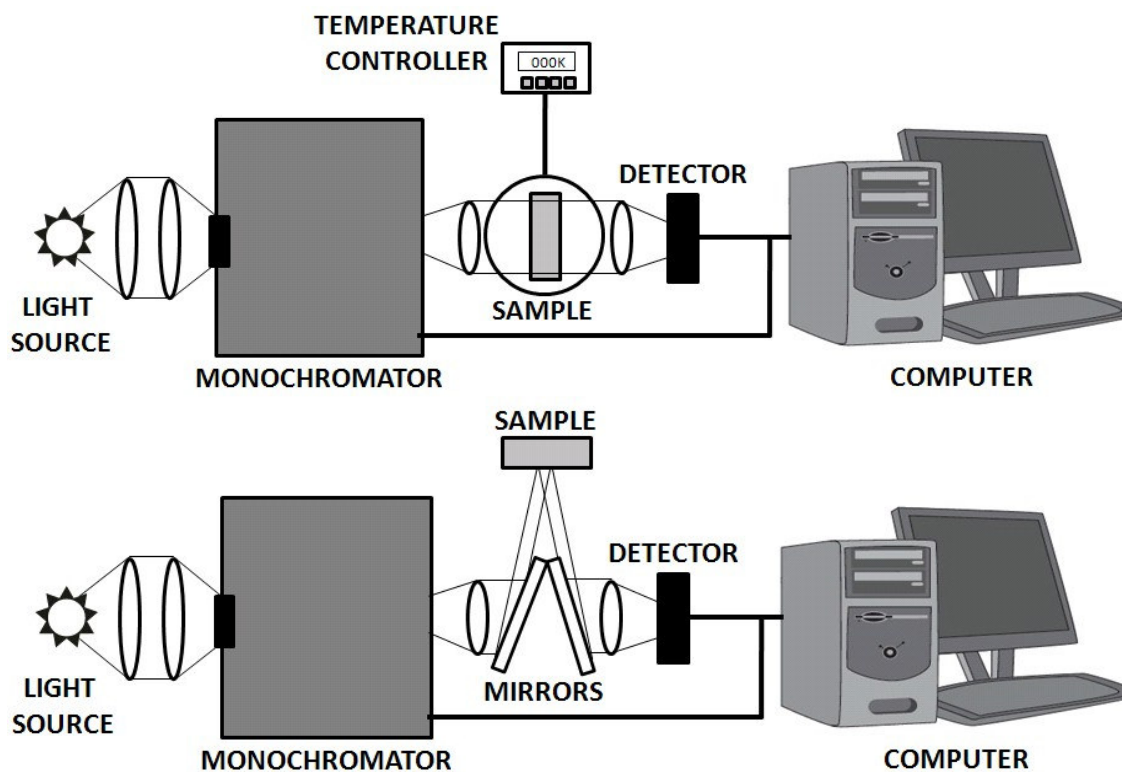


Figure 3.3. Schematic representations of (a) transmission and (b) reflection experimental setups

3.5 Photoluminescence Experiments

In the PL measurements, the surfaces of the crystals were irradiated along the *c*-axis by using the 325 nm line of a He–Cd laser, the 406 nm line of an “Oriel” Hg–Xe arc lamp, the 457.9 nm line of a argon-ion laser, the 532 nm line of a continuous frequency-doubled YAG:Nd³⁺ laser, and the 632.8 nm line of a He–Ne laser depending on the necessities of the experimental situations. The experiments were carried out by collecting the light from the light-illuminated face of the sample in a direction close to the normal of the layer. A “CTI-Cryogenics M-22” closed-cycle helium cryostat was used to cool the sample, and the temperature was controlled within an accuracy of ± 0.5 K. The resulting spectra of the sample were measured using an “Oriel MS257” monochromator with a grating of 1200 grooves mm⁻¹ and 3.22 nm mm⁻¹ dispersion, and a “Hamamatsu S7010-1008 FFT-CCD Image Sensor” with a single-stage electric cooler. In figure 3.4, a schematic representation of a typical PL setup is shown. Here it should also be mentioned that due to the broad

spectrum of Hg-Xe arc lamp, it was inevitable to use a bandpass filter to get a narrow spectrum from the lamp. The transmission spectrum of a typical bandpass filter is shown in figure 3.5. The resolution of the PL experimental system was better than 3 meV (≈ 0.3 nm). In laser intensity dependent measurements, sets of neutral density filters were used to adjust the exciting laser intensity. All of the PL spectra have been corrected for the spectral response of the optical apparatus. All the spectra have been analyzed by using a fitting program 'Peak Fit for Win 32 Version 4'. PL bands were fitted by Gaussian profiles. The procedure yields the peak position, short- and long-wavelength side half-widths, and the intensity of the bands. In the case of coexisting bands, we applied the same program to deconvolute the observed bands, as shown in figure 3.6.

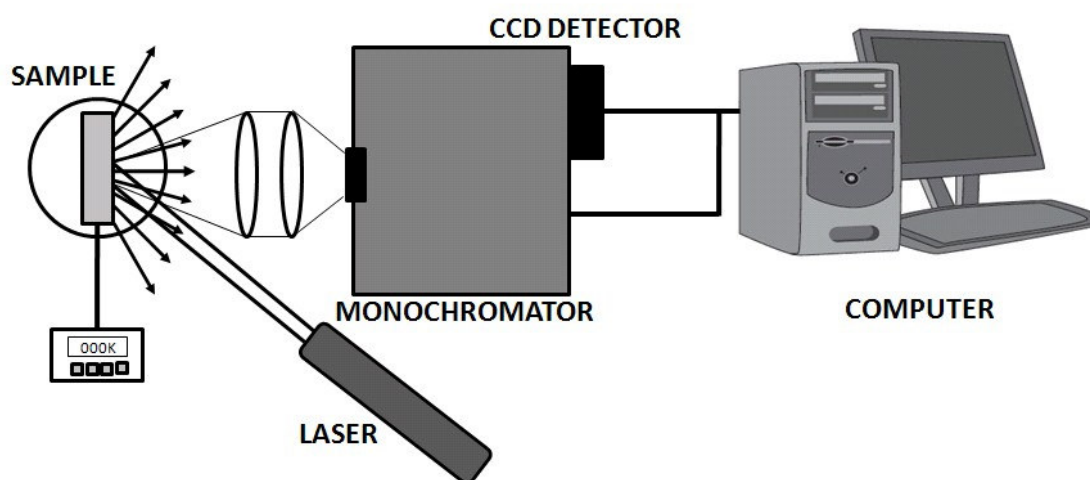


Figure 3.4. A schematic representation of a typical PL experimental setup

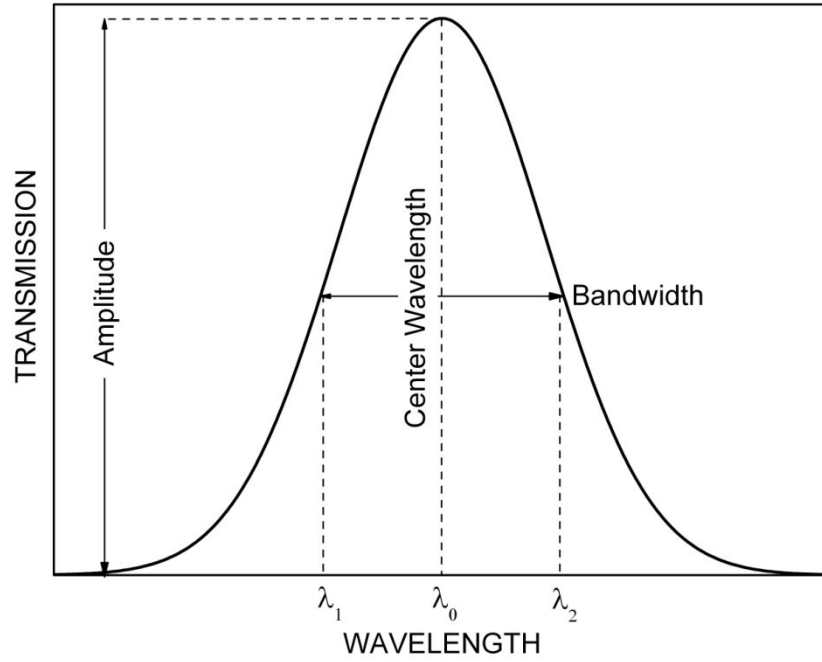


Figure 3.5. The transmission spectrum of a typical bandpass filter

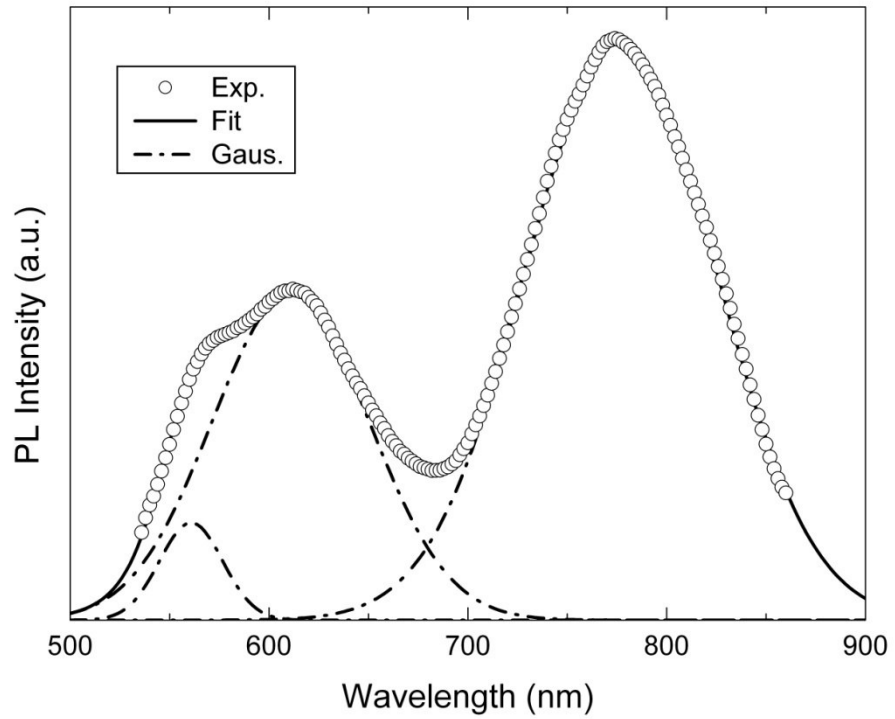


Fig. 3.6. An example of deconvolution of the photoluminescence spectra into three Gaussian lineshapes

3.6 Properties of the Crystals Used in the Experiments

$\text{TlIn}_x\text{Ga}_{1-x}\text{Se}_2$ and $\text{TlIn}_x\text{Ga}_{1-x}\text{S}_2$ crystal systems were synthesized from elements with purities better than 99.999 % taken in stoichiometric proportions. Single crystals were grown by using the Bridgman method from a melt of synthesized materials sealed in evacuated (10^{-5} Torr) silica tubes with a tip at the bottom in the laboratory of Physics Department, Baku State University. A simple representation of crystal growth by the Bridgman method can be seen in figure 3.6. In EDSA and PL measurements, the samples were freshly and gently cleaved with a razor blade from the middle part of the grown ingots and no further polishing and cleaning treatments were required because of the natural mirror-like cleavage planes. In the X-ray experiments, the samples were grinded in order to have them powdered. In reflection measurements the specimens with natural cleavage planes and a thickness such that $\alpha x \gg 1$ were used. For room temperature transmission measurements, the samples were reduced in thickness (by repeated cleaving using transparent adhesive tape) until they were convenient for the measurements ($\approx 10 \mu\text{m}$). Since the thin layered samples were very fragile, they broke into pieces at low temperatures. Therefore, the low-temperature measurements were carried out on thick samples ($\approx 300 \mu\text{m}$).

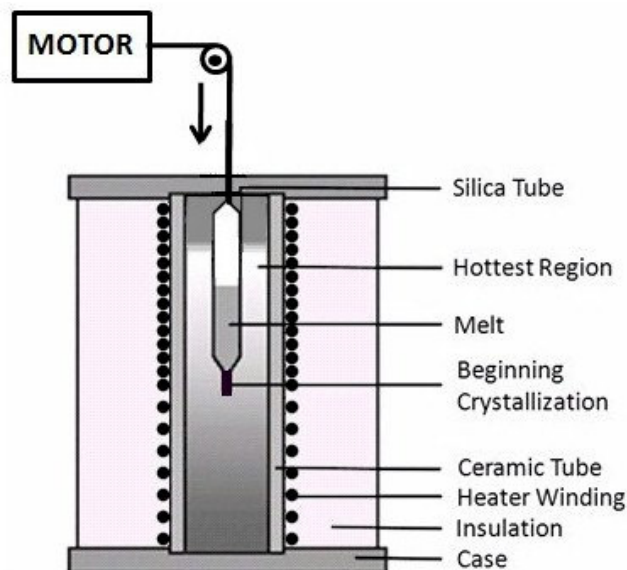


Fig. 3.7. A simple representation of crystal growth by the Bridgman method

CHAPTER 4

RESULTS AND DISCUSSIONS

4.1 Introduction

In this chapter, the results of the structural and optical characterization experiments on chain and layered $\text{Tl}_4\text{In}_3\text{GaSe}_8$, $\text{Tl}_4\text{InGa}_3\text{Se}_8$, $\text{Tl}_4\text{In}_3\text{GaS}_8$, $\text{Tl}_2\text{InGaS}_4$ and $\text{Tl}_4\text{InGa}_3\text{S}_8$ crystals will be the main subject. The analyses and the discussions on the experimental results will also be given in order to reveal the structural and optical properties of these materials. Furthermore, the physical basis of the optical processes taking place in the crystals studied will also be discussed.

4.2 Results of the Structural and Optical Characterization Experiments for $\text{Tl}_4\text{In}_3\text{GaSe}_8$ crystal

The quaternary compound $\text{Tl}_4\text{In}_3\text{GaSe}_8$ belongs to the group of semiconductors with chain crystal structure. This crystal is a structural analogue of TlInSe_2 , in which a quarter of the trivalent indium atoms are replaced by gallium atoms [87, 88]. In the lattice of $\text{Tl}_4\text{In}_3\text{GaSe}_8$ crystal, Ga^{3+} and In^{3+} ions are surrounded each by four selenium ions and form negatively charged chains $[\text{Ga}^{3+}(\text{In}^{3+})\text{Se}_2^-]^{1-}$ along the tetragonal c -axis. These chains are connected by thallium univalent ions Tl^{1+} (figure 4.1). Forces between ions inside chains are covalent and strong, and between chains are ionic and weak.

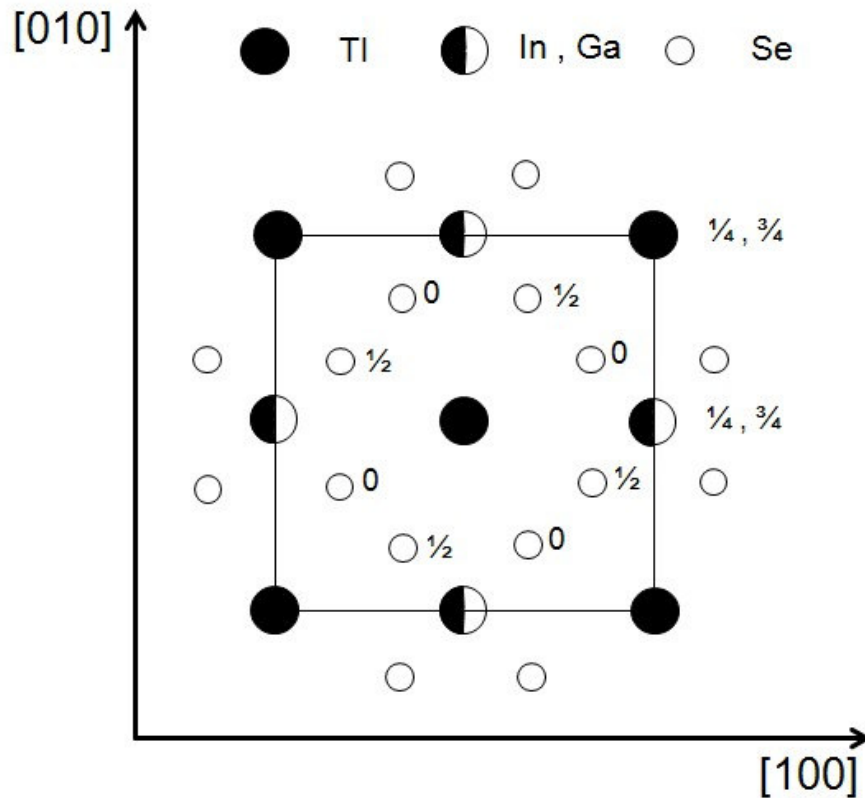


Figure 4.1. Projection of the unit cell of $\text{Tl}_4\text{In}_3\text{GaSe}_8$ crystal on the $[001]$ plane. The figures indicate heights above this plane.

The electrical conductivity of the studied sample was p-type as determined by the hot probe method. Crystals suitable for PL measurements had typical sample dimensions of $9 \times 2 \times 1 \text{ mm}^3$. After cleaving, the resulting ingot appeared grey-black in color and the freshly cleaved surfaces were mirror-like.

4.2.1 Results of X-Ray Experiments

The structure of $\text{Tl}_4\text{In}_3\text{GaSe}_8$ crystals was defined by the X-ray powder diffraction experiments. X-ray diffractogram of $\text{Tl}_4\text{In}_3\text{GaSe}_8$ is shown in figure 4.2. Table 4.1 shows the obtained Miller indices (hkl), the observed and calculated interplanar spacings (d) and the relative intensities (I/I_0) of the diffraction lines.

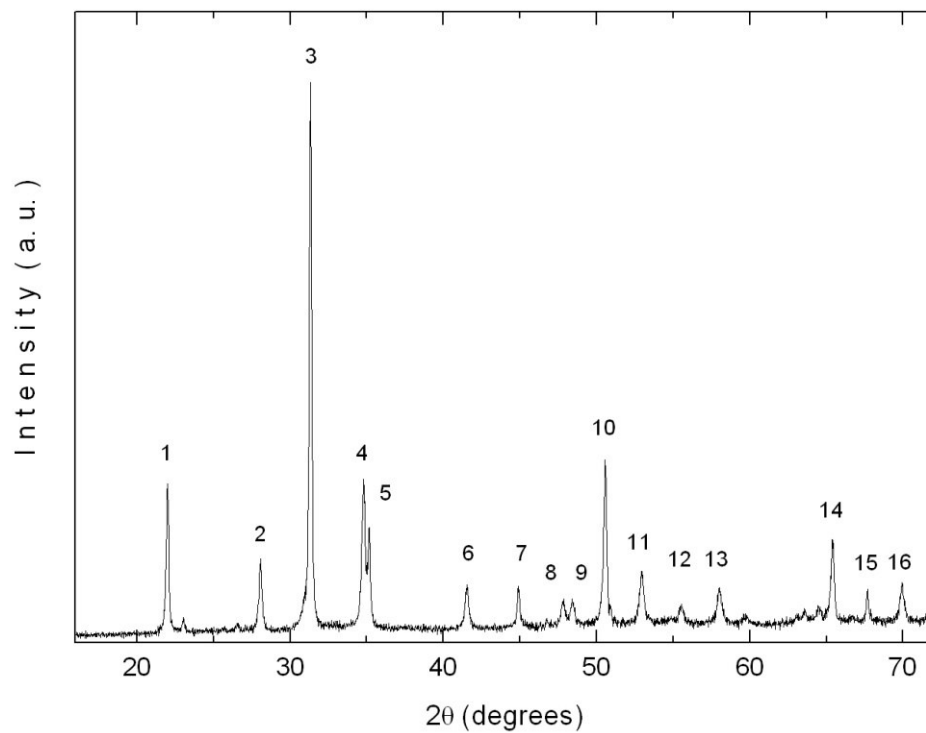


Figure 4.2. X-ray diffraction pattern of $\text{Tl}_4\text{GaIn}_3\text{Se}_8$ powder sample.

The calculated (using equation 2.12) and observed interplanar spacings were found to be in good agreement with each other. The parameters of the tetragonal unit cell for this crystal were found to be $a = 8.066$ and $c = 6.697$ nm.

Table 4.1. X-ray powder diffraction data for $\text{Tl}_4\text{In}_3\text{GaSe}_8$ crystal

No.	$h k l$	d_{obs} (nm)	d_{calc} (nm)	I/I_0
1	2 0 0	0.4032	0.4038	29
2	2 1 1	0.3178	0.3180	15
3	2 2 0	0.2852	0.2856	100
4	2 0 2	0.2576	0.2580	29
5	3 1 0	0.2550	0.2554	21
6	2 2 2	0.2171	0.2174	10
7	4 0 0	0.2017	0.2019	10
8	3 3 0	0.1902	0.1904	8
9	4 1 1	0.1879	0.1880	8
10	4 2 0	0.1803	0.1806	33
11	4 0 2	0.1726	0.1730	13
12	3 3 2	0.1653	0.1655	7
13	4 2 2	0.1589	0.1590	10
14	4 4 0	0.1426	0.1428	19
15	-	0.1379	-	10
16	6 0 0	0.1344	0.1346	11

4.2.2 Results of Energy Dispersive Spectral Analysis (EDSA) Experiments

The chemical composition of $\text{Tl}_4\text{In}_3\text{GaSe}_8$ crystals was determined by EDSA experiments. The result of the EDSA experiment in 0-10 keV energy range is shown in figure 4.3. The composition of the studied samples (Tl:In:Ga:Se) was found to be 25.5:19.1:6.5:48.9, respectively. Moreover, EDSA indicated that silicon impurities were present in the crystal.

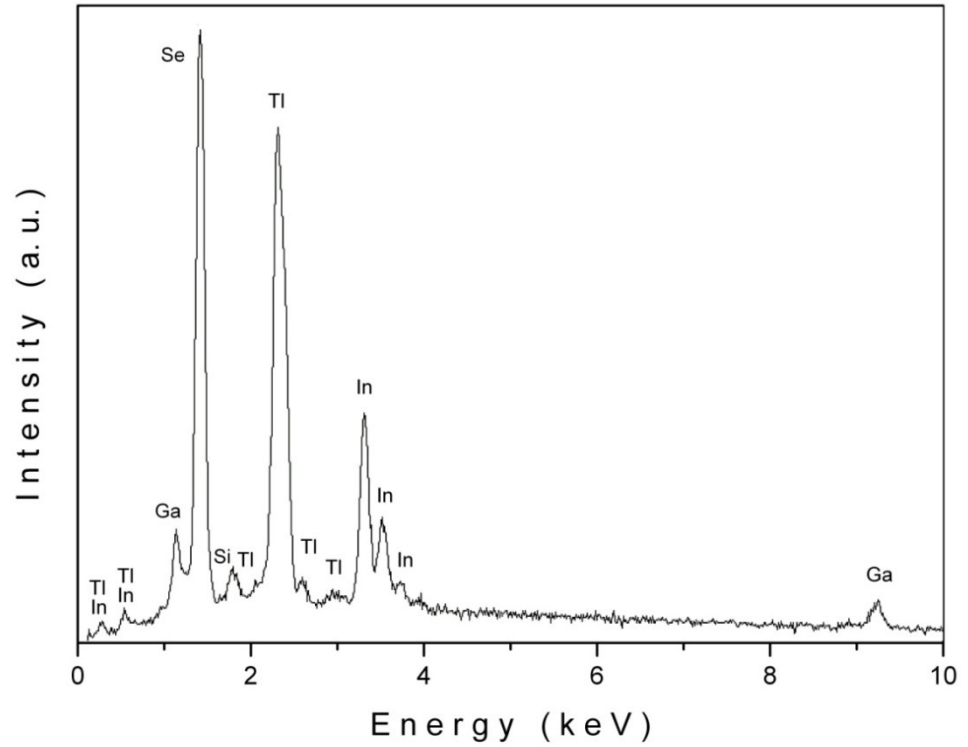


Figure 4.3. The result of EDSA experiment on $Tl_4In_3GaSe_8$ crystal.

4.2.3 Results of Transmission Experiments

For $Tl_4In_3GaSe_8$ single crystals, the transmittance (T) spectra were recorded in the photon energy range of 1.05-1.40 eV. For these measurements, it was difficult to prepare thin platelets, because the samples have easy cleavage along two mutually perpendicular directions, which results in thin needles. Therefore, we had to carry out the transmission experiments on thick samples having thickness about 470 μm . From these spectral data, the absorption coefficient, α , was calculated using equation 2.19, defined previously in chapter 2 as

$$T \cong (1 - R)^2 \exp(-\alpha x) . \quad (2.19)$$

The calculated room temperature data are illustrated in figure 4.4. It is clear from the figure that the absorption coefficient of $Tl_4In_3GaSe_8$ crystals increases with increasing photon energy in the region of 1.10-1.35 eV. The value of α increased from 45 to 160 cm^{-1} in that region. Analysis of the experimental data showed that the

absorption coefficient and the photon energy of $\text{Tl}_4\text{In}_3\text{GaSe}_8$ can be related by equation 2.15 as

$$(\alpha h\nu) = A (h\nu - E_g)^p \quad (2.15)$$

with $p = 2$. Inset of figure 4.4 displays the dependence of $(\alpha h\nu)^{1/2}$ on photon energy. The circles are the experimental data and the solid line is fitted to a linear equation for finding the band gap. A linear dependence for the relation of $(\alpha h\nu)^{1/2}$ versus $h\nu$ is found. As previously mentioned in chapter 2, this proportionality suggests the realization of an indirect allowed transition for the crystal studied. The extrapolation of straight line down to $(\alpha h\nu)^{1/2} = 0$ gives the value of indirect band gap for $\text{Tl}_4\text{In}_3\text{GaSe}_8$ crystal. The energy of indirect band gap deduced from this dependence is evaluated to be 0.94 eV.

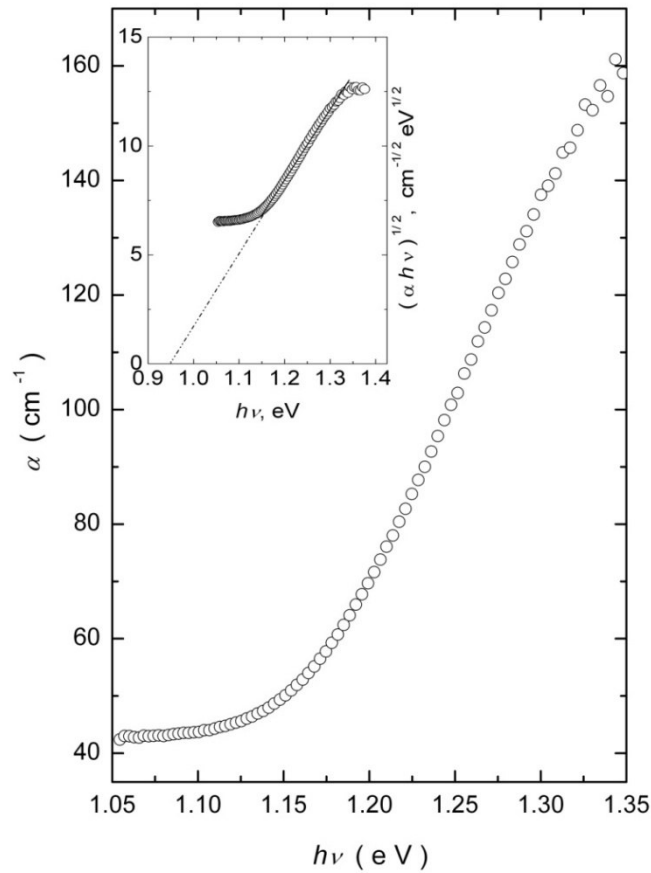


Figure 4.4. Dependence of absorption coefficient on photon energy for $\text{Tl}_4\text{In}_3\text{GaSe}_8$ crystal.

Inset: Plot of $(\alpha h\nu)^{1/2}$ versus $h\nu$.

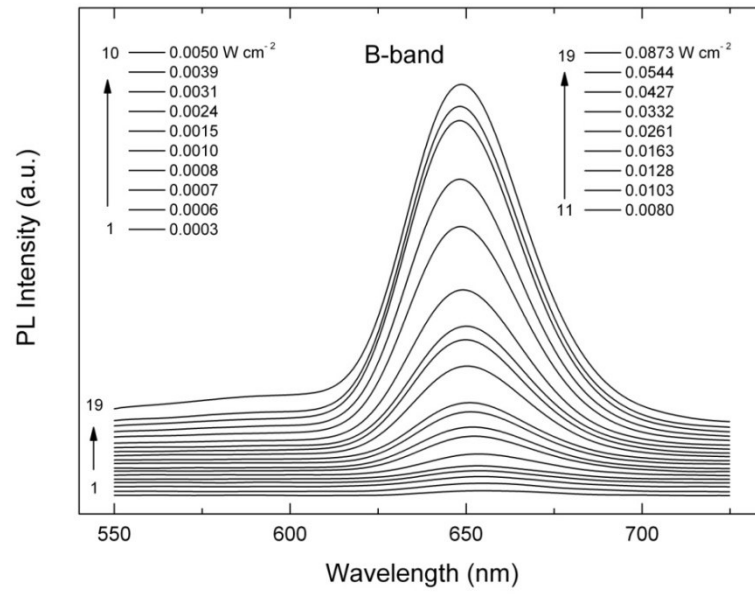
4.2.4 Results of Photoluminescence Experiments

In the PL spectra of $\text{Tl}_4\text{In}_3\text{GaSe}_8$, we observed two bands (labeled as A and B), dominating in the spectra at different excitation intensities. For the analysis, we plotted two different figures to trace the behavior of the PL bands with respect to laser excitation intensity variations. Figure 4.5a shows the PL spectra of the $\text{Tl}_4\text{In}_3\text{GaSe}_8$ crystal measured in the 550-725 nm wavelength and 0.0003-0.0873 Wcm^{-2} laser excitation intensity range at a constant temperature $T = 30$ K for B-band centered at 649 nm (1.91 eV). Likewise, figure 4.5b shows the PL spectra measured in the 550-725 nm wavelength and 0.0873-1.1777 Wcm^{-2} laser excitation intensity range at a constant temperature value $T = 30$ K for A-band centered at 599 nm (2.07 eV). From figure 4.5a, it is seen that the B-band intensity at peak maximum increases with increasing laser excitation intensity values from 0.0003 up to 0.0873 Wcm^{-2} . However, when laser excitation intensity exceeds the value 0.0873 Wcm^{-2} , this behavior drastically changes. In figure 4.5b, we see that while A-band arises and starts to dominate the spectra, the intensity of B-band decreases in the magnitude rapidly. In addition to the previous discussion, from the figures 4.5a and 4.5b, we also see that B-band emission peak shifts slightly towards higher energies with increasing excitation laser intensity, whereas A-band emission peak does not show significant change.

To follow the behavior of both bands more clearly, we plotted the PL emission band maximum intensity versus excitation laser intensity in logarithmic scale (figure 4.6). The common behavior of both bands with respect to excitation laser intensity is clearly demonstrated by this graph. For the analysis, the experimental data for each band in the spectra (the linear part of the curves) were fitted by the power law of the form of equation 2.33, defined in chapter 2, as

$$I \propto L^Y . \quad (2.33)$$

(a)



(b)

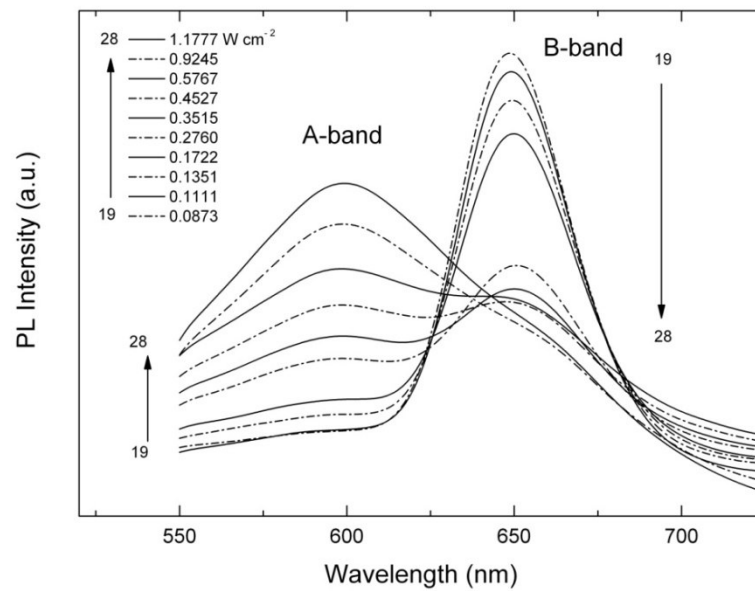


Figure 4.5. PL spectra of $\text{Tl}_4\text{In}_3\text{GaSe}_8$ crystal as a function of excitation laser intensity at $T = 30$ K: (a) B-band, 0.0003 - 0.0873 W cm^{-2} excitation intensity range; (b) A- and B-bands, 0.0873 - 1.1777 W cm^{-2} excitation intensity range.

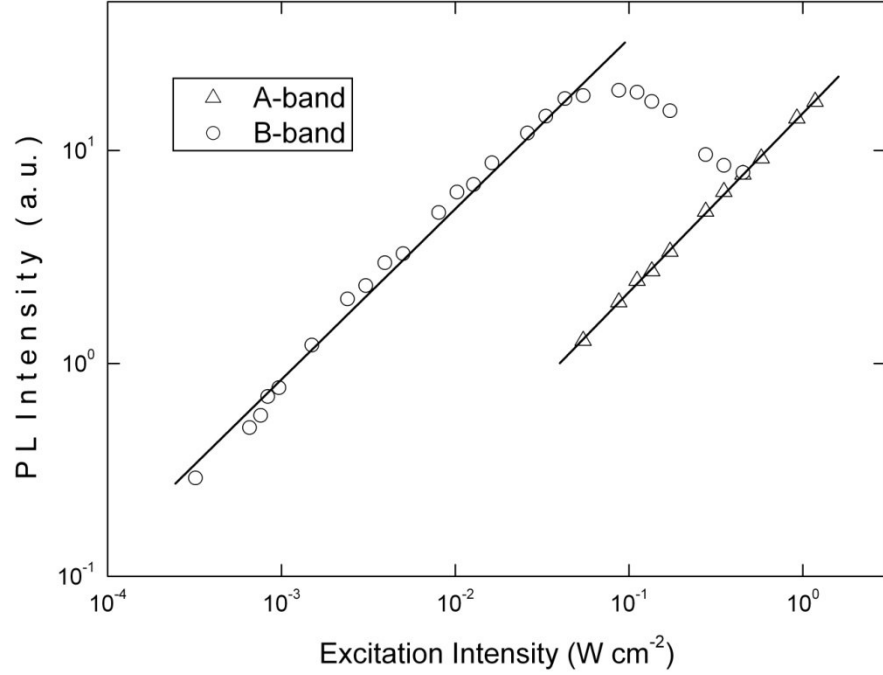


Figure 4.6. Dependences of PL intensities at the emission band maxima versus excitation laser intensity at $T = 30$ K. The solid lines show the theoretical fits using equation 2.33.

We find that PL intensity for both bands increases sublinearly with increasing excitation laser intensity. By fitting the experimental data, we found γ values as 0.84 and 0.80 for A- and B-bands respectively. As mentioned in chapter 2, the exponent γ is generally $1 < \gamma < 2$ for the free- and bound-exciton emission, and $\gamma \leq 1$ for free-to-bound and donor-acceptor pair recombination.

The dependence of the PL spectra on temperature provides a very important understanding of the nature and analysis of luminescence spectra. In order to be able to follow the temperature dependent behaviors of both bands in the PL spectra of $\text{Tl}_4\text{GaIn}_3\text{Se}_8$ crystals more clearly, we chose special excitation intensity values where each band is heavily dominant in the spectra, namely 0.0557 W cm^{-2} for B-band and 1.1777 W cm^{-2} for A-band. The PL spectra of $\text{Tl}_4\text{GaIn}_3\text{Se}_8$ crystals in the 600-700 nm range at constant laser excitation intensity 0.0557 W cm^{-2} for temperature range from 16 up to 46 K are shown in figure 4.7a and the PL spectra in the 535-750 nm range at constant laser excitation intensity 1.1777 W cm^{-2} for temperature range from 16 up to 300 K are shown in figure 4.7b. In figure 4.7a, we observed B-band

centered at 633 nm (1.96 eV) and in figure 4.7b, we observed A-band centered at 589 nm (2.10 eV). As seen from the figures 4.7a and 4.7b, both bands change their intensities and peak positions as the temperature changes: the peak intensities decrease as the temperature is increased and the peak positions show several degrees of red shift with increasing temperature (about 5 and 1 nm for B- and A-bands, respectively). The emission bands have asymmetrical Gaussian line shapes with short- and long-wavelength side FWHM values of 0.172 and 0.261 eV (A-band) and 0.055 and 0.062 eV (B-band), respectively. The observed behavior of the peak energy positions for the A- and B-bands satisfies the temperature dependence expected for free-to-bound recombination [89, 90].

The activation energies for both bands have been obtained by fitting the equation 2.40, defined in chapter 2, to our experimental data as

$$I = \frac{I_0}{1 + \alpha \exp\left(-\frac{E_t}{k_B T}\right)}. \quad (2.40)$$

The emission band maximum intensities with respect to reciprocal temperature are drawn in figure 4.8 in 16-46 K (B-band) and in 16-300 K (A-band) temperature ranges. After a nonlinear least squares fit, the activation energies for A- and B-bands are found to be 0.03 and 0.01 eV, respectively. These shallow levels can be considered as originating from uncontrolled impurities or from point defects due to deviations in stoichiometry. The former may be attributed to the presence of Si impurities introduced into $\text{Tl}_4\text{In}_3\text{GaSe}_8$ during the crystal growth process in ungraphitized ampoules (see figure 4.3).

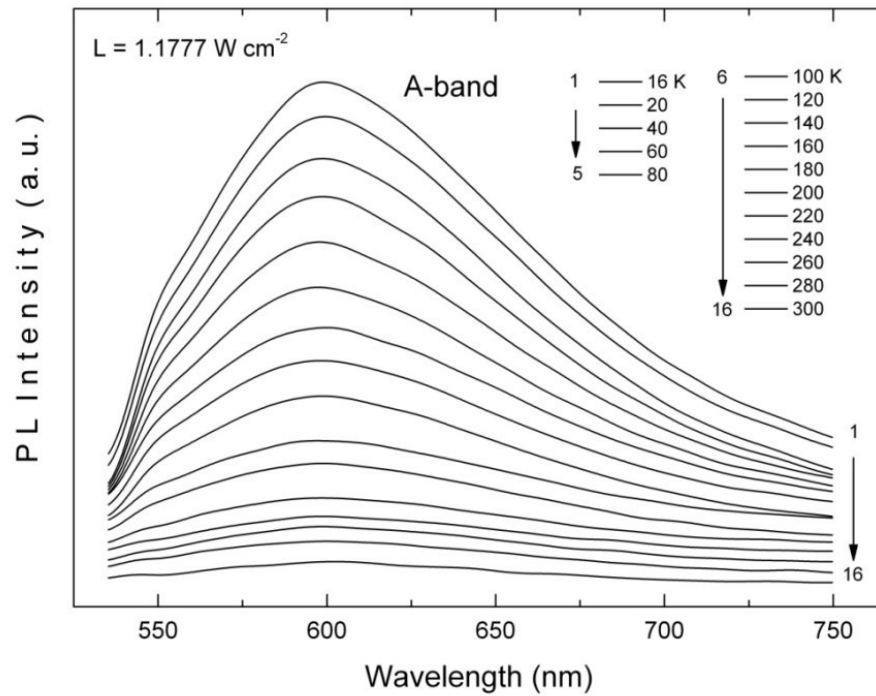
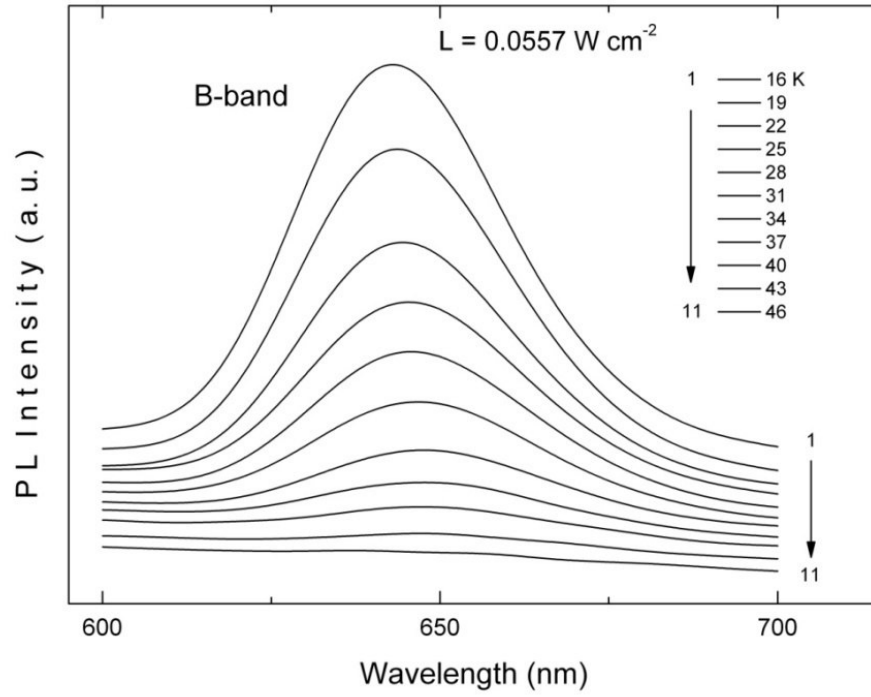


Figure 4.7. Temperature dependence of PL spectra from $\text{Tl}_4\text{In}_3\text{GaSe}_8$ crystals: (a) B-band, excitation laser intensity $L = 0.0557 \text{ W cm}^{-2}$; (b) A-band, excitation laser intensity $L = 1.1777 \text{ W cm}^{-2}$.

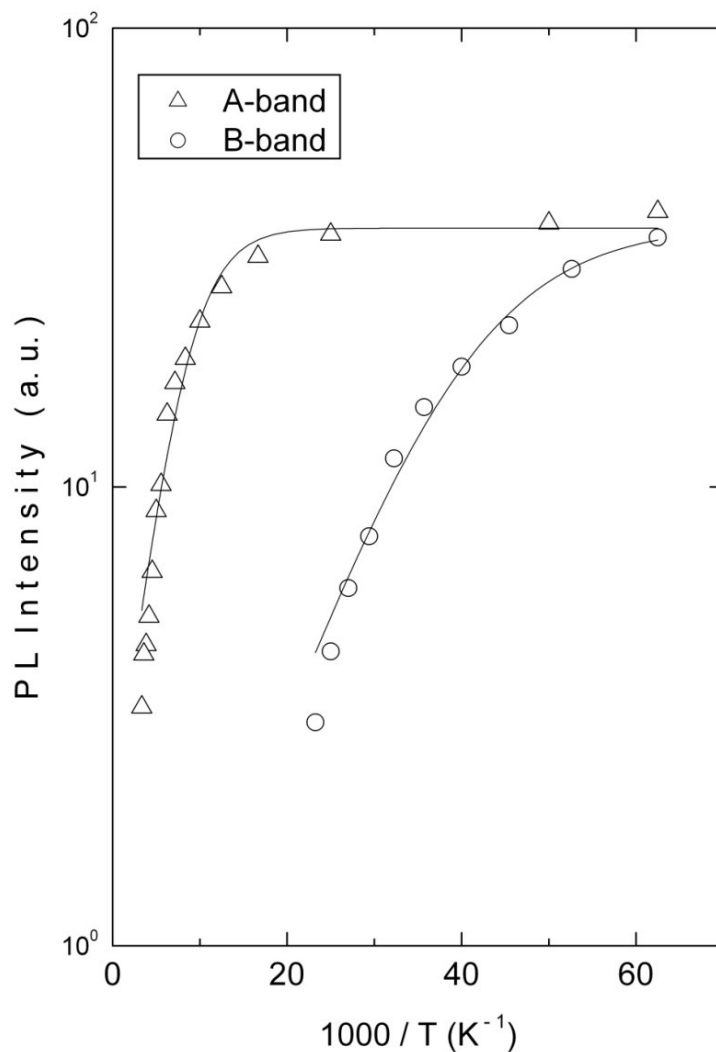


Figure 4.8. Temperature dependence of PL band intensity for A- and B-bands. Circles and triangles are the experimental data and solid curves show the theoretical fit using equation 2.43.

Figure 4.9 shows the energy-level diagram for the PL emission bands of $\text{Tl}_4\text{In}_3\text{GaSe}_8$ crystal. Using the activation energies determined from the temperature dependence of the PL intensity for p-type $\text{Tl}_4\text{In}_3\text{GaSe}_8$ crystal, we placed acceptor levels a_1 and a_2 at 0.03 and 0.01 eV above the valence band. Taking into account the peak energy values of the observed transitions (2.10 and 1.96 eV for A- and B-bands, respectively), the related two initial energy states were then placed at 2.13 and 1.97 eV above the valence band.

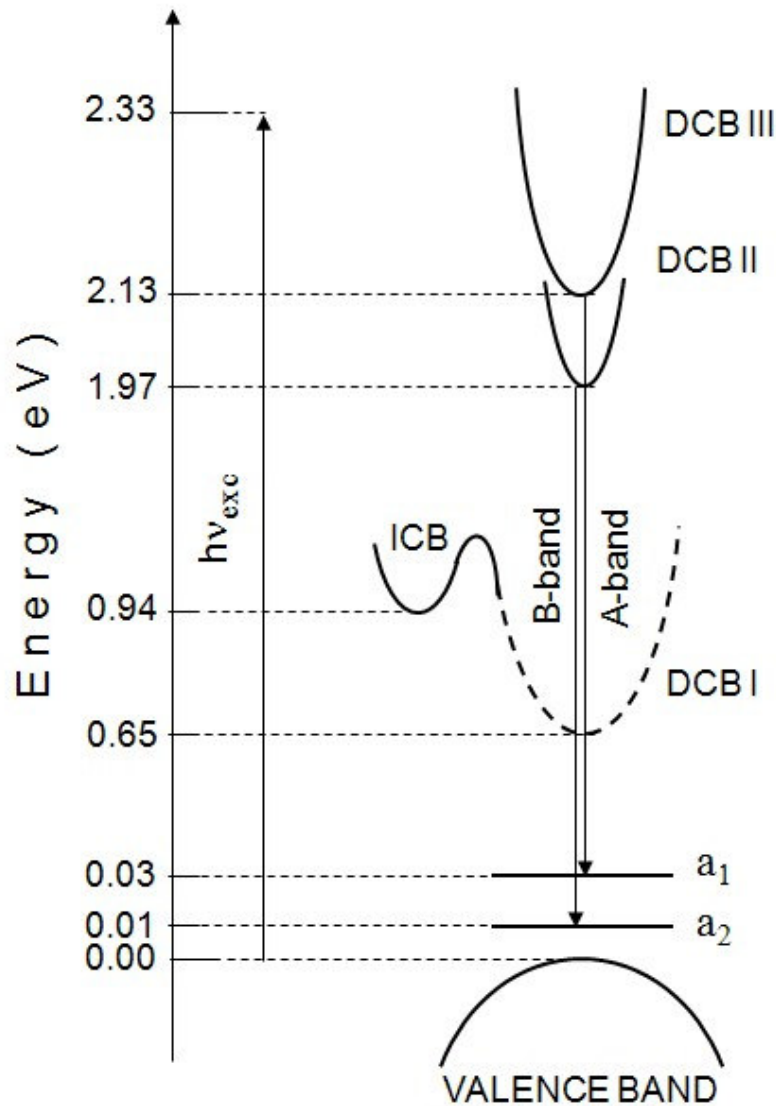


Figure 4.9. Proposed energy-level diagram of $\text{Tl}_4\text{In}_3\text{GaSe}_8$ at $T = 16$ K.

The pseudo-potential method and tight binding model calculations of TlInSe_2 crystal band structure revealed the existence of several conduction bands [16, 91]. The top of the valence band and the bottoms of three lowest conduction bands (DCB I, DCB II, DCB III) are situated on the Brillouin-zone edge and belong to the irreducible representation T_3 . In addition, the first conduction band has the second minimum (ICB) at the Brillouin-zone edge, which belongs to the irreducible representation D_1 . Thus, the indirect band gap in TlInSe_2 crystal (1.28 eV) is formed by $T_3 \rightarrow D_1$ transitions. Three direct band gaps (0.60, 1.82 and 1.94 eV) correspond to $T_3 \rightarrow T_4$, $T_3 \rightarrow T_{10}$ and $T_3 \rightarrow T_6$ transitions, respectively [91]. According to [13],

the direct transitions to the first conduction band (DCB I) in TlInSe₂ crystal is forbidden in the dipole approximation.

Taking into account the results of X-ray, transmission and photoluminescence measurements, we suppose, by analogy with the band structure calculation of TlInSe₂ [70], the existence in Tl₄In₃GaSe₈ crystal of an indirect band gap at 0.94 eV, and the second and third direct band gaps at 1.97 and 2.13 eV, respectively (figure 4.9). As for the first direct band gap, we could not observe this transition experimentally, since it is forbidden. Therefore, the assumed lowest conduction band (DCB I) is shown by a dotted curve in figure 4.9. The values of $\gamma = 0.84$ and 0.80 , obtained from the dependence of the A- and B-band maximum intensities on excitation intensity, are in agreement with our assignment of the observed emission bands in Tl₄In₃GaSe₈ spectra to the free-to-bound recombination [76]. The assumption that the transitions from the minima of the third and second conduction bands to the acceptor levels a_1 and a_2 , respectively, are responsible for the A- and B-emission bands is confirmed by the absence of these emission bands in the PL spectra of Tl₄In₃GaSe₈ crystal with excitation by the red line of the He-Ne laser ($E_{exc} = 1.96$ eV). The presence of the emission bands in the PL spectra at higher energies than the fundamental band gap energy has also been reported for CuGaTe₂ ternary crystals [82]. It was proposed that the transitions from a higher conduction band minimum to defect states are responsible for the observed PL bands.

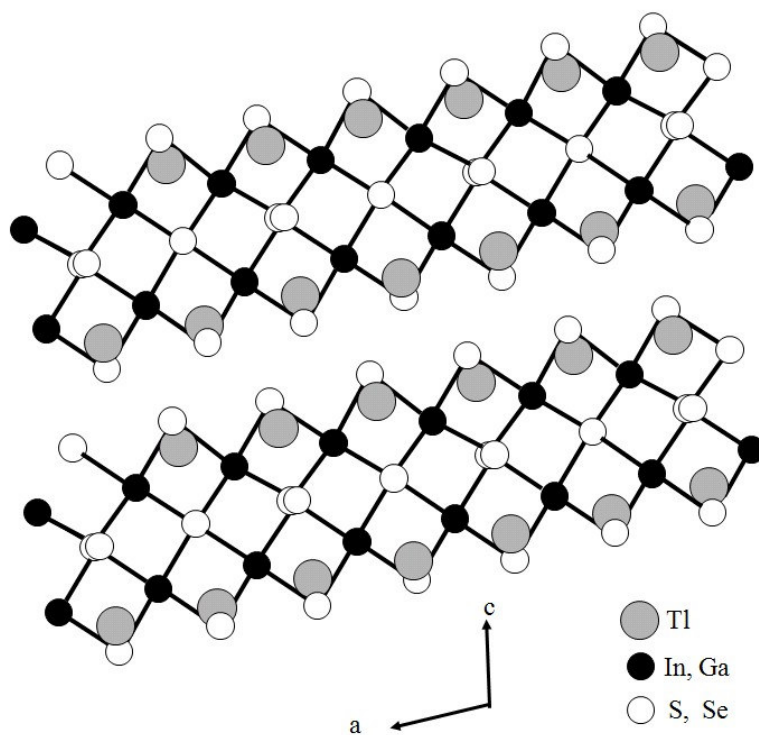
At low excitation intensity ($L < 0.0873$ W cm⁻²) sufficient to observe the B-band emission (figure 4.5a), the quasi-Fermi level for electrons is located above only the minimum of the second conduction band (figure 4.9). With increasing excitation intensity ($L \geq 0.0873$ W cm⁻²), the quasi-Fermi level for electrons is shifted and the number of excited electrons is large enough to fill the third conduction band as well, responsible for the observed A-band emission. Therefore, in the PL spectra we observe A-band emission along with the B-band (figure 4.5b). If the transition probability for electrons from the third conduction band to acceptor level a_1 is much greater than that for electrons from the second conduction band to acceptor level a_2 , then, with increasing excitation intensity ($L > 0.4527$ W cm⁻²), the dominant radiative recombination will occur from the third conduction band (figures 4.5b and 4.9). The decrease in the B-band intensity with increasing excitation intensity may probably be attributed to the activation of a non-radiative recombination channel.

4.3 Results of the Structural and Optical Characterization Experiments for $\text{Tl}_4\text{InGa}_3\text{Se}_8$ crystal

The quaternary $\text{Tl}_4\text{InGa}_3\text{Se}_8$ crystal is a member of the group of layered semiconductors. This compound has a structural similarity to TlGaSe_2 crystal with a difference that a quarter of gallium ions are replaced by indium ions [87, 92]. The lattice structure of $\text{Tl}_4\text{In}_3\text{GaSe}_8$ is composed of rigorously periodic two-dimensional layers arranged parallel to the (001) plane (figure 4.10), and each such consecutive layer is rotated by a right angle with respect to the previous one. The bonding between Tl and Se atoms is of an interlayer type whereas the bonding between (In)Ga and Se is of an intralayer type. The basic structural units of a layer are the $\text{Ga}_4(\text{In}_4)\text{Se}_6$ adamantane-like units connected together by bridging Se atoms. The Tl atoms are in trigonal prismatic voids resulting from the combination of the $\text{Ga}_4(\text{In}_4)\text{Se}_6$ polyhedra into a layer. The Tl atoms form nearly planar chains along the $[110]$ and $[1\bar{1}0]$ directions.

The electrical conductivity of the studied sample was n-type as established by the hot probe method. Crystals suitable for PL measurements had typical sample dimensions of $9 \times 2 \times 1 \text{ mm}^3$. After cleaving, the resulting ingot appeared red in color and the freshly cleaved surfaces were mirror-like.

(a)



(b)

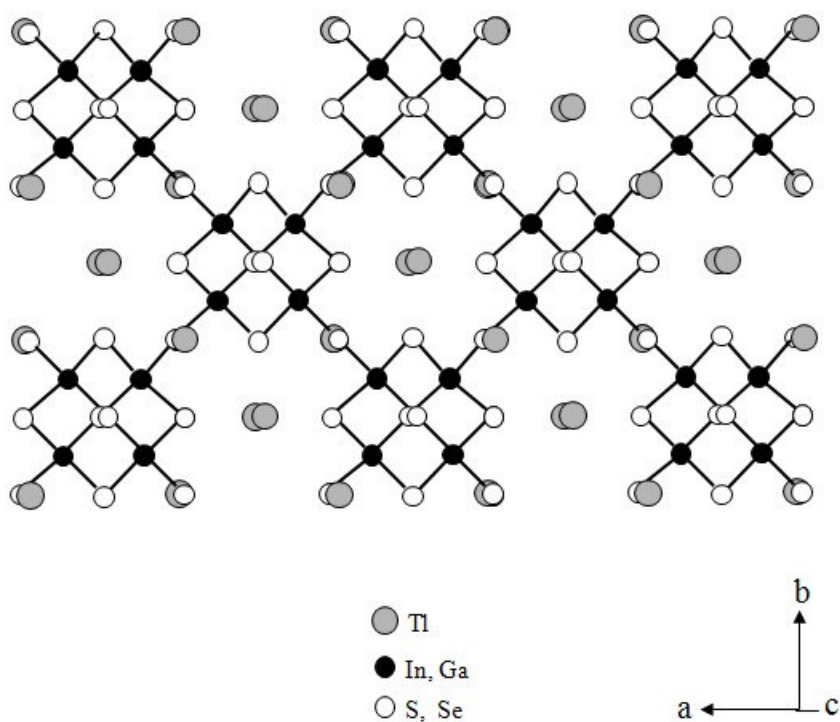
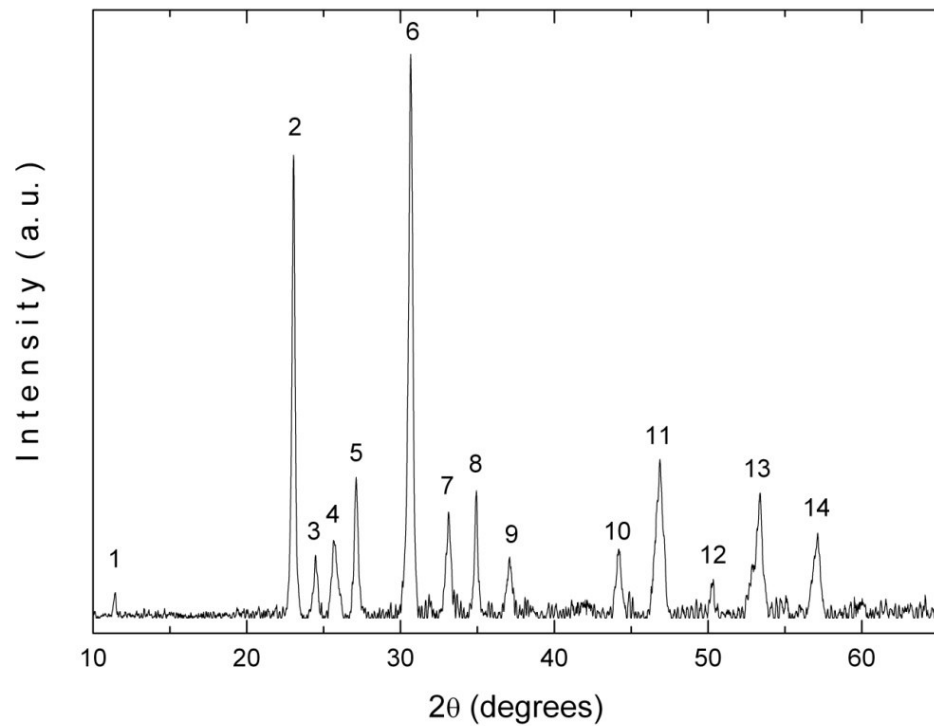


Figure 4.10. Projection of structure of $\text{Tl}_4\text{InGa}_3\text{Se}_8$ and $\text{TlGaS}_2\text{-TlInS}_2$ crystals on (a) ac-plane and (b) ab-plane.

4.3.1 Results of X-Ray Experiments

The X-ray powder diffraction experiments were used to define the structure of $\text{Tl}_4\text{InGa}_3\text{Se}_8$ crystals. Figure 4.11 shows X-ray diffractogram of $\text{Tl}_4\text{InGa}_3\text{Se}_8$. As a result of the analysis, the obtained Miller indices (hkl), the observed and calculated interplanar spacings (d) and the relative intensities (I/I_0) of the diffraction lines are listed in table 4.2.



4.11. X-ray diffraction pattern of $\text{Tl}_4\text{InGa}_3\text{Se}_8$ powder sample.

From the table, it was seen that the calculated (using equation 2.12) and observed interplanar spacings were in good agreement with each other. The lattice parameters of the monoclinic unit cell were found to be $a = 0.7659$, $b = 0.7698$ and $c = 1.0308$ nm, and $\beta = 94.25^\circ$.

Table 4.2. X-ray powder diffraction data for $\text{Tl}_4\text{InGa}_3\text{Se}_8$ crystal

No.	$h k l$	d_{obs} (nm)	d_{calc} (nm)	I/I_0
1	0 0 1	0.7644	0.7644	5
2	0 2 0	0.3852	0.3850	83
3	2 1 1	0.3637	0.3637	12
4	1 0 2	0.3494	0.3498	14
5	1 2 -1	0.3295	0.3294	25
6	2 2 -1	0.2902	0.2903	100
7	0 2 2	0.2713	0.2712	19
8	3 2 0	0.2561	0.2560	22
9	0 1 3	0.2418	0.2418	11
10	3 3 0	0.2053	0.2054	13
11	5 0 1	0.1950	0.1949	29
12	5 2 -1	0.1791	0.1791	6
13	0 2 4	0.1711	0.1711	23
14	2 4 2	0.1614	0.1614	15

4.3.2 Results of EDSA Experiments

EDSA experiments were employed to determine the chemical composition of $\text{Tl}_4\text{InGa}_3\text{Se}_8$ crystals. Figure 4.12 displays the result of the experiment in 0-10 keV energy range. The composition of the studied samples (Tl:In:Ga:Se) was found to be 25.6:6.4:19.3:48.7, respectively. Moreover, the presence of silicon impurities in the crystal was indicated by EDSA.

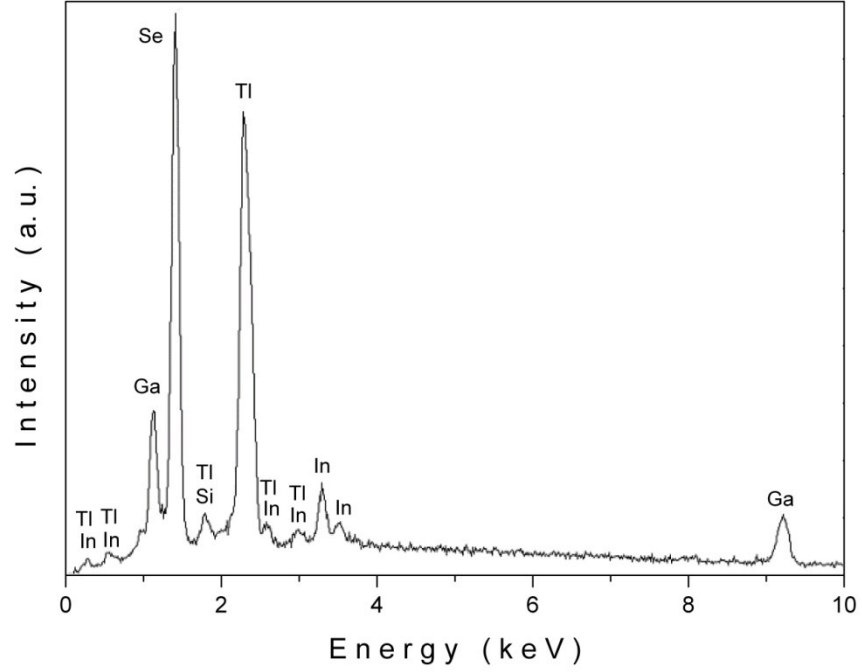


Figure 4.12. Energy dispersive spectroscopic analysis of $Tl_4InGa_3Se_8$ crystal.

4.3.3 Results of Transmission and Reflection Experiments

The transmittance (T) and reflectance (R) spectra of $Tl_4InGa_3Se_8$ single crystals were recorded in the wavelength range of 500-1100 nm (figure 4.13). The reflectivity of the material is given by equation 2.16 as

$$R = \frac{(n - 1)^2 + k^2}{(n + 1)^2 + k^2}, \quad (2.16)$$

The transmittance is represented by equation 2.18 as

$$T = \frac{(1 - R)^2 \exp(-\alpha x)}{1 - R^2 \exp(-2\alpha x)}. \quad (2.18)$$

By the help of these relations, n , k and α can be determined from the reflectivity and transmittance measurements. The reflectivity measurements were done using specimens with natural cleavage planes and a thickness such that $\alpha x \gg 1$. The sample thickness was then reduced by repeated cleaving using transparent adhesive tape until it was useful for transmission measurements. The determination of

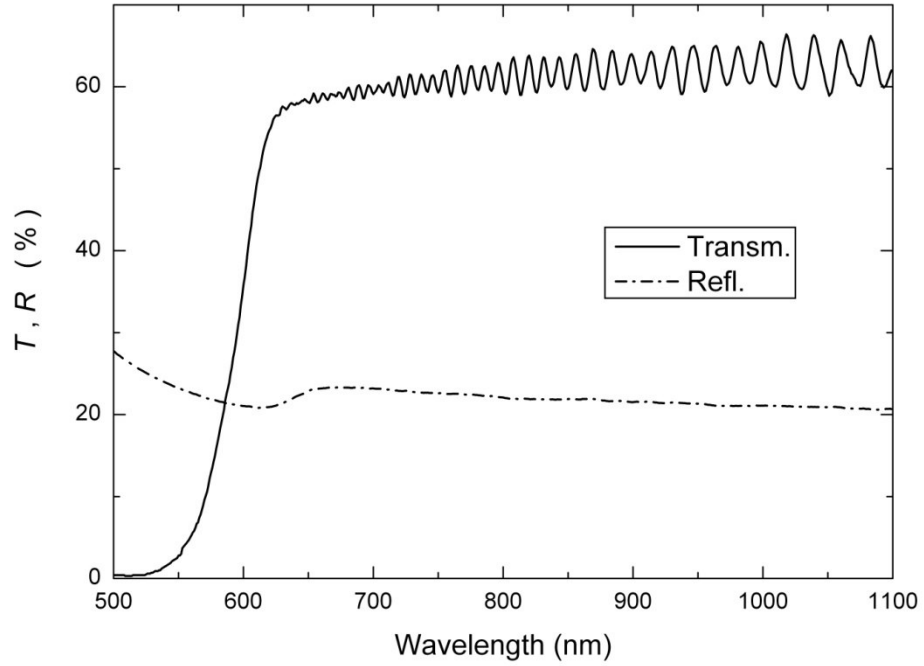


Figure 4.13. The spectral dependence of transmittance and reflectivity for $\text{Tl}_4\text{InGa}_3\text{Se}_8$ crystal at $T = 300$ K.

thickness of the sample was done using transmission interference fringes at wavelengths slightly longer than the intrinsic absorption edge, where the sample has relatively high transmission values (figure 4.13) by the help of equation 2.21. The long-wavelength value of the refractive index $n = 2.67$, found from reflection measurements, was used to determine the thickness of the sample, which turned out to be about $10 \mu\text{m}$ for room temperature transmission measurements in most of the cases.

The analysis of the dependence of absorption coefficient on photon energy in the high absorption regions is carried out to obtain the detailed information about the energy band gaps. As previously mentioned, the relation between the absorption coefficient α and photon energy can be expressed by equation 2.15. As a result of calculations, it was revealed that the room temperature absorption coefficient α for $\text{Tl}_4\text{InGa}_3\text{Se}_8$ crystal changes from 50 to 3930 cm^{-1} with increasing photon energy from 1.90 to 2.40 eV. The analysis of the experimental data showed that the absorption coefficient is proportional to $(h\nu - E_g)^p$ with $p = 2$ in the energy range

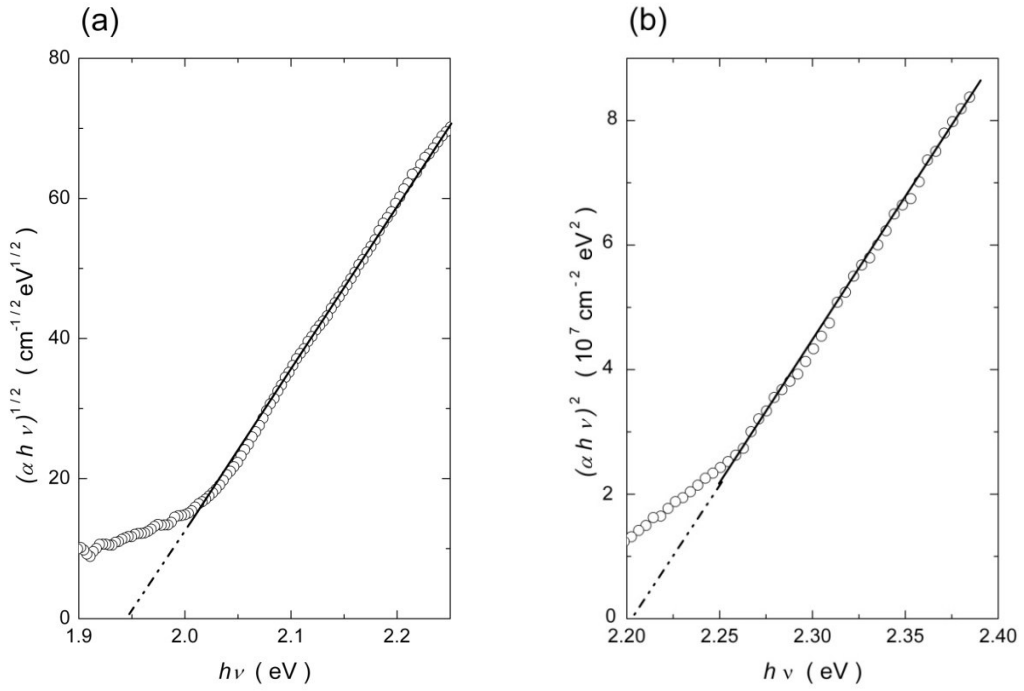


Figure 4.14. The variation of absorption coefficient as a function of photon energy at $T = 300$ K: the dependence of (a) $(\alpha h\nu)^{1/2}$ and (b) $(\alpha h\nu)^2$ on photon energy.

2.00-2.24 eV and $p = 1/2$ in the energy range 2.26-2.40 eV. Figures 4.14a and 4.14b display the dependences of $(\alpha h\nu)^{1/2}$ and $(\alpha h\nu)^2$ on photon energy $h\nu$, respectively. The circles are the experimental data that were fitted to a linear equation (the solid lines) for finding the band gaps. The linear dependencies were observed for the relations $(\alpha h\nu)^{1/2}$ and $(\alpha h\nu)^2$ versus $h\nu$. This suggests the realization of indirect and direct allowed transitions for $\text{Tl}_4\text{InGa}_3\text{Se}_8$ crystal over the ranges 2.00-2.24 and 2.26-2.40 eV, respectively. The values of indirect and direct band gap energies were found by using the extrapolations of the straight lines down to $(\alpha h\nu)^{1/2} = 0$ and $(\alpha h\nu)^2 = 0$ as $E_{\text{gi}} = 1.94 \pm 0.02$ eV and $E_{\text{gd}} = 2.20 \pm 0.02$ eV, respectively.

Figure 4.15 shows the transmission spectra for $\text{Tl}_4\text{InGa}_3\text{Se}_8$ crystal registered in the temperature range of 10-300 K. Since the thin layered samples broke into pieces at low temperatures due to their excessive fragility, the low temperature

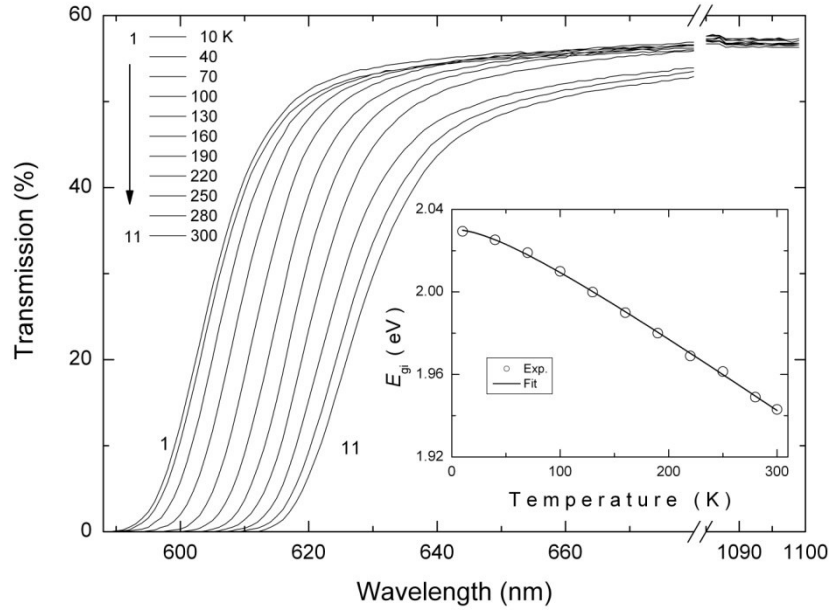


Figure 4.15. The spectral dependence of transmission for $Tl_4InGa_3Se_8$ crystal in the temperature range of 10-300 K. Inset: the indirect band gap energy as a function of temperature. The solid line represents the fit using equation 2.10.

measurements could only be carried out on thick samples having thickness about 300 μm . For this reason, we were only able to analyze the temperature dependence of indirect energy band gap (E_{gi}). Technical reasons did not allow a direct measurement of the reflection at low temperatures. Therefore, for the calculation of absorption coefficient α , the spectral dependence of room temperature reflectivity was uniformly shifted in energy according to the blue shift of the absorption edge.

The value of indirect transition energy gap obtained by the analysis decreases from 2.03 to 1.94 eV with increasing temperature from 10 to 300 K, as illustrated in the inset of figure 4.15. The temperature dependence of the energy band gap can be represented by equation 2.10 as

$$E_g(T) = E_g(0) + \frac{\gamma T^2}{(T + \beta)}. \quad (2.10)$$

The experimental data for the dependence of $E_{gi} - T$ on temperature were fitted using equation 2.10 as shown in the inset of figure 4.15 (solid line corresponds to theoretical fit) and the fitting parameters were found to be $E_{gi}(0) = 2.03$ eV, $\gamma = -4.1 \times 10^{-4}$ eV/K and $\beta = 125$ K. It should be noted that the Debye temperature for

$\text{Tl}_4\text{InGa}_3\text{Se}_8$ crystal was found to be $\beta = 130$ K, estimated by Lindemann's melting rule [93] using X-ray results and melting temperature $T_m = 1075$ K.

Figure 4.16 shows the change of refractive index n calculated using equations 2.14, 2.16 and 2.18 as a function of wavelength. It is clear from this figure that the refractive index gradually decreases from 2.87 to 2.67 in the energy region of $h\nu < E_g$ with increasing wavelength in the range 675-1100 nm. The long wavelength value of refractive index is consistent with the values 2.6 ($\lambda = 1100\text{nm}$) and 2.9 ($\lambda = 1500\text{nm}$) reported for TlGaS_2 [67] and TlGaSe_2 [68] layered single crystals, respectively.

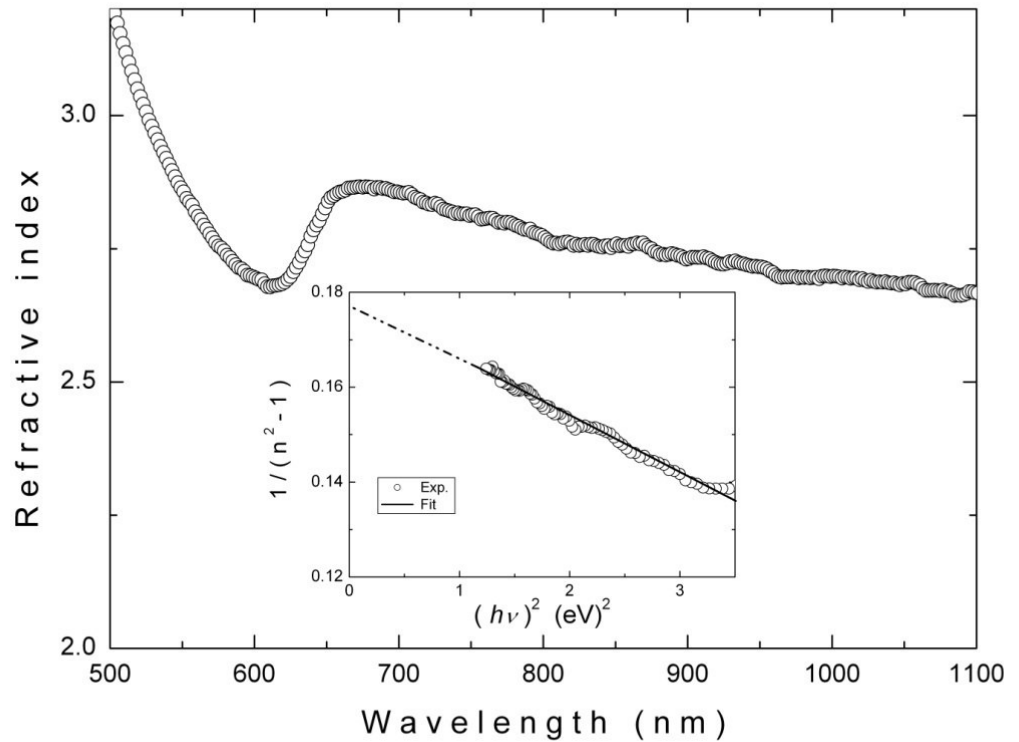


Figure 4.16. The dependence of refractive index on the wavelength for $\text{Tl}_4\text{InGa}_3\text{Se}_8$ crystal. Inset: plot of $(n^2-1)^{-1}$ versus $(h\nu)^2$. The solid line represents the fit using equation 2.22.

The dispersive refractive index data in $h\nu < E_g$ range were analyzed according to the single-effective-oscillator model proposed by Wemple and DiDomenico [60, 61]. In this model, the refractive index is related to photon energy through the equation 2.22 as

$$n^2(h\nu) = 1 + \frac{E_{so}E_d}{E_{so}^2 - (h\nu)^2}. \quad (2.22)$$

The oscillator parameters were calculated by fitting a linear function to the lower energy range (1.13-1.96 eV) of $(n^2-1)^{-1}$ versus $(hv)^2$ graph. The result of the fitting process of the above function is presented in the inset of figure 4.16. The zero-frequency refractive index n_0 is estimated according to the equation 2.23. By using the slope and the intersection with y-axis of the straight line (inset of figure 4.16), the values of the parameters E_{so} and E_d were calculated to be 4.10 and 23.17 eV, respectively. In addition to these, the values of zero-frequency dielectric constant $\epsilon_0 = n_0^2 = 6.65$ and refractive index $n_0 = 2.58$ were evaluated from equation 2.22. As mentioned in chapter 2, the oscillator energy E_{so} is an ‘‘average’’ energy gap and, to a fair approximation, it is associated empirically with the lowest direct band gap E_{gd} by the relationship $E_{so} \cong 2.0 E_{gd}$. The ratio of E_{so}/E_{gd} for $Tl_4InGa_3Se_8$ crystal was calculated as 1.86, in this study.

To determine the oscillator strength S_{so} for $Tl_4InGa_3Se_8$ crystal, the analysis of refractive index n can be used. The refractive index is represented by a single Sellmeier oscillator at low energies by equation 2.25 as

$$(n^2 - 1)^{-1} = \frac{1}{S_{so}\lambda_{so}^2} - \frac{1}{S_{so}\lambda^2}, \quad (2.25)$$

The values of S_{so} and λ_{so} calculated from $(n^2-1)^{-1}$ versus λ^{-2} plot were found to be $6.21 \times 10^{-13} \text{ m}^{-2}$ (95.48 eV^2) and $3.02 \times 10^{-7} \text{ m}$, respectively. Here, it should be noted that the obtained value of oscillator strength is of the same order as those obtained for ZnS, ZnSe, Ag_2S , $GeSe_2$ and $TlGaS_2$ crystals [61, 65, 67, 94].

4.3.4 Results of Photoluminescence Experiments

The dependence of the PL spectra on temperature provides a very important understanding of the nature and analysis of luminescence spectra. Figure 4.17 presents the PL spectra of $Tl_4InGa_3Se_8$ crystals in 17-68 K temperature range at constant laser excitation intensity $L = 55.73 \text{ mW cm}^{-2}$. The observed emission band has asymmetrical Gaussian line shape and centered at 652 nm (1.90 eV) at $T = 17 \text{ K}$. As seen from figure 4.17, emission band changes its peak position, FWHM and intensity as a function of the sample temperature: the peak position shows several degrees of red shift with increasing temperature; the FWHM increases and the peak intensity decreases as temperature is increased. The FWHM rises from 0.09 to 0.12 eV with increasing temperature in the range of 17-68 K.

The experimental data for the temperature dependence of PL band intensity can be fitted by the equation 2.40. Figure 4.18 shows the temperature dependence of the emission band maximum intensity as a function of the reciprocal temperature in the 17-68 K range. The best fit using equation 2.40, demonstrated by the solid curve in figure 4.18, has been achieved with the parameter $E_t = 0.03$ eV. Since $\text{Tl}_4\text{InGa}_3\text{Se}_8$ crystal is a p-type semiconductor, as determined by the hot probe technique, we believe that this level is shallow acceptor level located at 0.03 eV above the top of the valence band. This shallow level can be considered as originating from point defects due to deviations in stoichiometry or from uncontrolled impurities. The latter may be attributed to the presence of Si impurities introduced into $\text{Tl}_4\text{InGa}_3\text{Se}_8$ during the crystal growth process in ungraphitized ampoules. Inset of figure 4.18 illustrates the shift of the peak energy to lower energies with increasing temperature. It is well known that the donor-acceptor pair transition energy decreases along with the band gap energy when the temperature is increased [70].

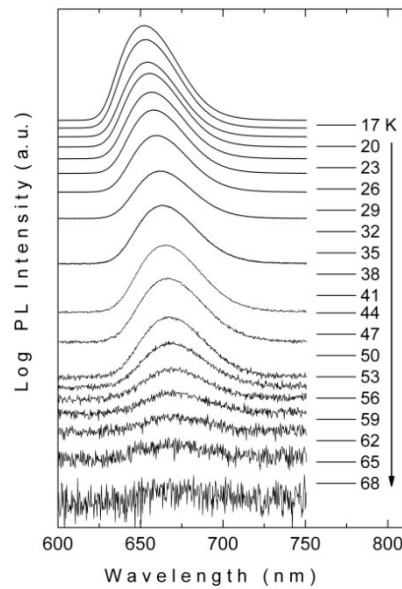


Figure 4.17. Temperature dependence of PL spectra from $\text{Tl}_4\text{InGa}_3\text{Se}_8$ crystals at excitation laser intensity of $L = 55.73 \text{ mW cm}^{-2}$.

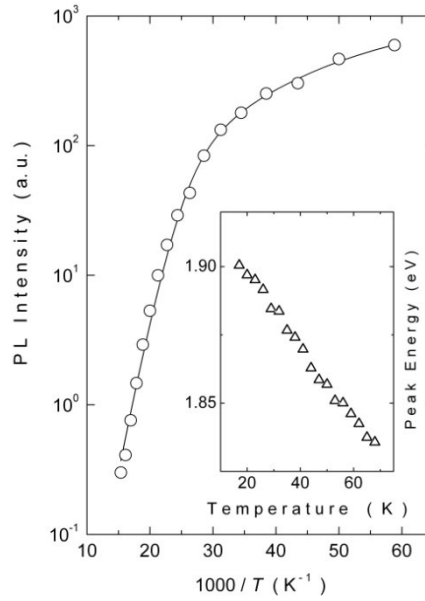


Figure 4.18. Temperature dependencies of PL band intensity for $\text{Tl}_4\text{InGa}_3\text{Se}_8$ crystal. Circles are the experimental data. Solid curve shows the theoretical fit using equation 2.40. Inset: temperature dependence of emission band peak energy.

The laser excitation intensity dependence of PL spectra also provides valuable information about the recombination mechanism responsible for the observed luminescence. Figure 4.19 presents the PL spectra for 22 different laser intensities at $T = 20$ K. From analysis of the spectra, we obtained the information about the peak energy position and intensity for emission band at different laser excitation intensities. Our analysis reveals that the peak energy position changes with laser excitation intensity (blue shift). The behavior of the emission band is in agreement with the idea of inhomogeneously distributed donor-acceptor pairs for which increasing laser excitation intensity leads to blue shift of the band by exciting more pairs that are closely spaced [49, 95]. A careful inspection of the data shows that the emission band maximum slightly shifts towards higher energies ($\Delta E_p = 36$ meV) with increasing excitation laser intensities from 0.13 to 55.73 mW cm^{-2} (i.e., 14 meV per decade of exciting radiation intensity). The magnitude of the observed blue shift is typical of ternary and quaternary chalcogenide compounds such as TlInS_2 [44], $\text{Tl}_2\text{InGaS}_4$ [96], HgInGaS_4 [97], $\text{CuIn}_{1-x}\text{Ga}_x\text{Se}_2$ [98], which are 40, 20, 20, 15 meV per decade of intensity of exciting radiation, respectively.

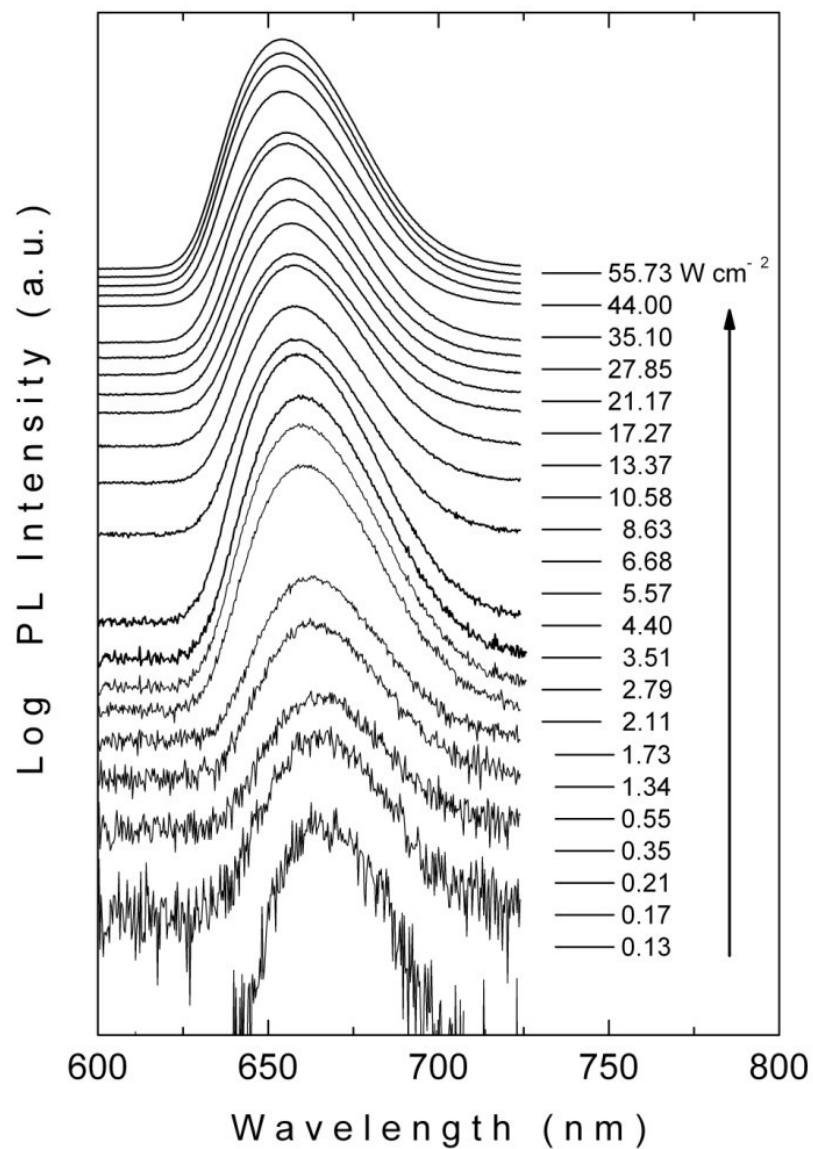


Figure 4.19. PL spectra of $\text{Tl}_4\text{InGa}_3\text{Se}_8$ crystal as a function of excitation laser intensity at $T = 20$ K.

At low excitation laser intensities only a small fraction of the donor and acceptor levels trap carriers. This leads to recombination from distant pairs only. At high enough excitation laser intensities all donors and acceptors are excited, which leads to a contribution from closer pairs as well. The energy of the emitted photon

during a donor-acceptor pair transition has a positive contribution from a Coulombic interaction between ionized impurities. This contribution increases as the separation between the pairs decreases [70]. Furthermore, radiative transition probabilities for different pair separations are different and decrease exponentially as a function of the pair distance [70]. Distant pair recombination (contributing to the low part energy part of a donor-acceptor pair emission band) saturates at high excitation laser intensities, whereas close pairs have larger transition probability and can accommodate more carriers. We, therefore, observe a shift of the emission band peak energy to higher energy as the excitation laser intensity increases.

The dependence of the emission band peak energy (E_p) at $T = 20$ K as a function of excitation laser intensity (L) is given in figure 4.20. The experimental data in figure 4.20 are then fitted by equation 2.36, defined in chapter 2, as

$$L = D \frac{(h\nu_m - h\nu_\infty)^3}{h\nu_B + h\nu_\infty - 2h\nu_m} \exp\left(-\frac{2(h\nu_B - h\nu_\infty)}{h\nu_m - h\nu_\infty}\right). \quad (2.36)$$

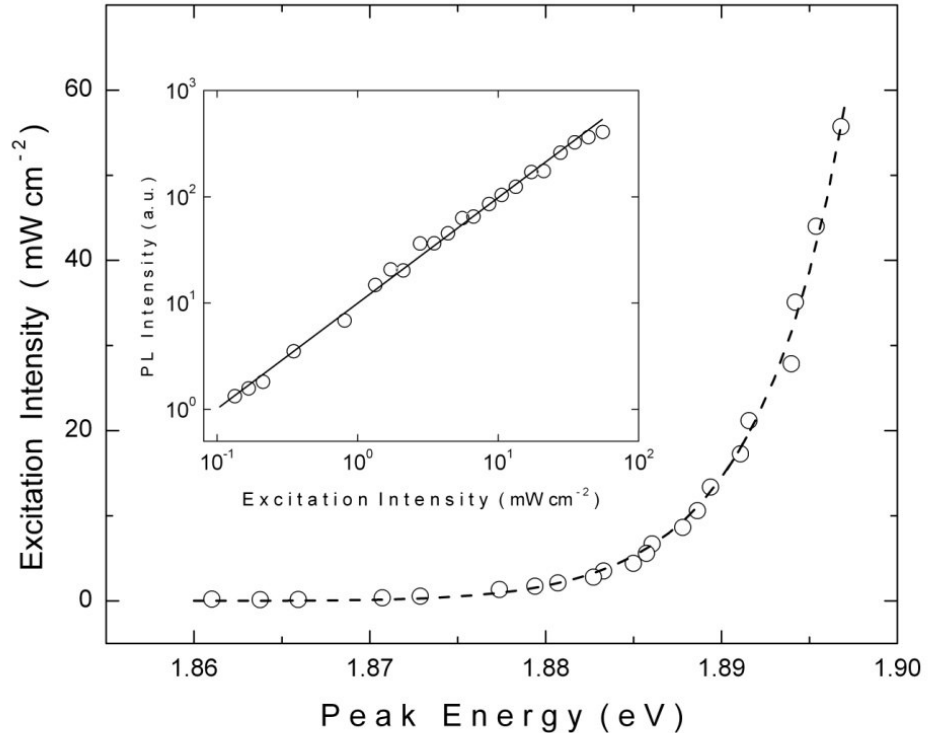


Figure 4.20. Excitation laser intensity versus emission band peak energy at $T = 20$ K. The dashed curve represents the theoretical fit using equation 2.36. Inset: dependence of PL intensity at the emission band maxima versus excitation laser intensity at $T = 20$ K. The solid line shows the theoretical fit using equation 2.33.

From a nonlinear least square fit to the experimental data, the photon energy values for an infinitely distant donor-acceptor pair and a close donor-acceptor pair separated by R_B are found to be $E_\infty = 1.83$ eV and $E_B = 1.99$ eV, respectively. These limiting photon energy values are in good agreement with the band gap energy ($E_{gd} = 2.29$ eV) and the observed values of the peak energy position (i.e., $E_\infty < 1.86$ eV $< E_p < 1.90$ eV $< E_B < E_{gd}$) at $T = 20$ K.

In PL spectra of $Tl_4InGa_3Se_8$ crystal, the increase in the peak intensities of emission band with the increase in the laser excitation intensity was also observed. The logarithmic plot of PL intensity versus laser excitation intensity is given in inset of figure 4.20. Experimental data can be fitted by a simple power law of the form of equation 2.33. We found that PL intensity at the emission band maximum increases sublinearly with increase of excitation laser intensity with the value of $\gamma = 0.96$. As mentioned in chapter 2, the exponent γ is generally $1 < \gamma < 2$ for free- and bound-exciton emission, whereas $0 < \gamma \leq 1$ is typical for free-to-bound and donor-acceptor pair recombination.

The analysis of the PL spectra as a function of temperature and excitation laser intensity allows one to obtain a possible scheme for the states located in the forbidden energy gap of the $Tl_4InGa_3Se_8$ crystal (figure 4.9). In the proposed scheme, shallow acceptor level a is located at 0.03 eV above the top of the valence band. On the basis of equation 2.31 for the emission energy of donor-acceptor pair and taking E_{gd} and E_∞ into account, the sum of the activation energies of the donor (E_d) and acceptor (E_a) levels, involved in the emission band, has been estimated as $E_d + E_a = E_{gd} - E_\infty = 2.29$ eV $- 1.83$ eV = 0.46 eV. Considering that the acceptor level a is located at 0.03 eV above the top of the valence band, this result suggests that the donor level d involved in the emission band is located at 0.43 eV below the bottom of the conduction band. Taking the above considerations into account, the observed emission band in the PL spectra has been attributed to the radiative transitions from the donor level d to the acceptor level a .

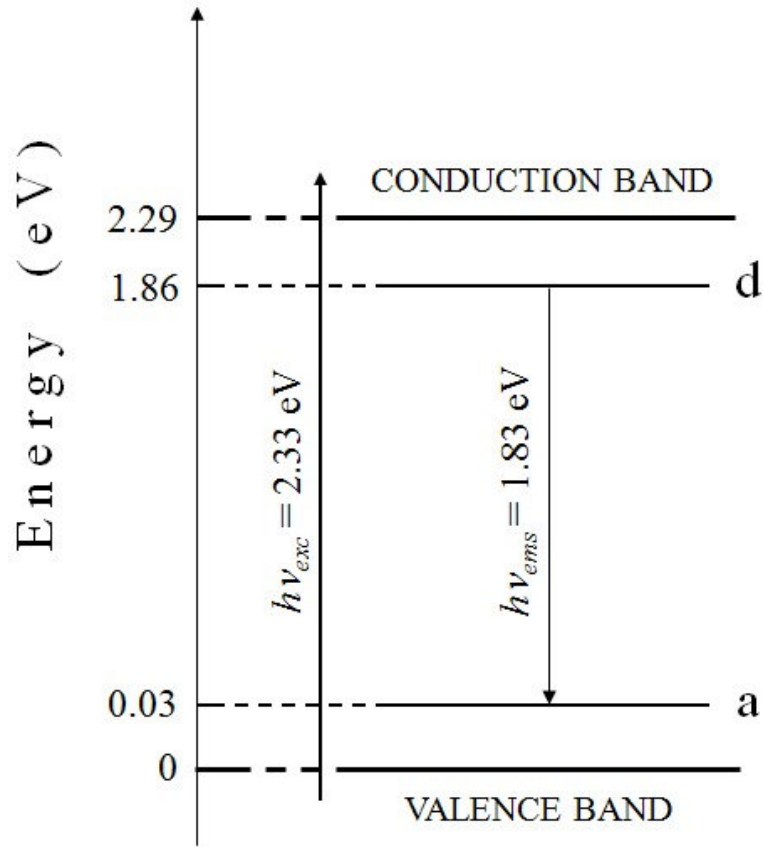


Figure 4.21. Proposed energy-level diagram of $\text{Tl}_4\text{InGa}_3\text{Se}_8$ at $T = 20$ K.

4.4 Results of the Structural and Optical Characterization Experiments for $\text{Tl}_4\text{In}_3\text{GaS}_8$ crystal

The quaternary $\text{Tl}_4\text{In}_3\text{GaS}_8$ crystal belongs to the group of layered semiconductors. This compound is a structural analog of TlInS_2 , in which a quarter of indium ions are replaced by gallium ions [92]. The lattice of $\text{Tl}_4\text{In}_3\text{GaS}_8$ consists of strictly periodic two-dimensional layers arranged parallel to the (001) plane (figure 4.10). Each successive layer is rotated by a right angle with respect to the previous one. Interlayer bonding is formed between Tl and S atoms while the bonding between Ga(In) and S atoms is an intralayer type. The fundamental structural unit of a layer is the $\text{Ga}_4(\text{In}_4)\text{S}_6$ adamantane-like units linked together by bridging S atoms.

The electrical conductivity of the studied sample was determined as n-type by the hot probe method. Crystals suitable for PL measurements had typical sample dimensions of $6 \times 4 \times 1$ mm³. After cleaving, the resulting ingot appears yellow-green in color and the freshly cleaved surfaces were mirror-like.

4.4.1 Results of X-Ray Experiments

The structure of $\text{Tl}_4\text{In}_3\text{GaS}_8$ crystals was defined by the X-ray powder diffraction experiments. X-ray diffractogram of $\text{Tl}_4\text{In}_3\text{GaS}_8$ is shown in figure 4.22. As a result of the analysis, the obtained Miller indices (hkl), the observed and calculated interplanar spacings (d) and the relative intensities (I/I_0) of the diffraction lines are listed in table 4.3.

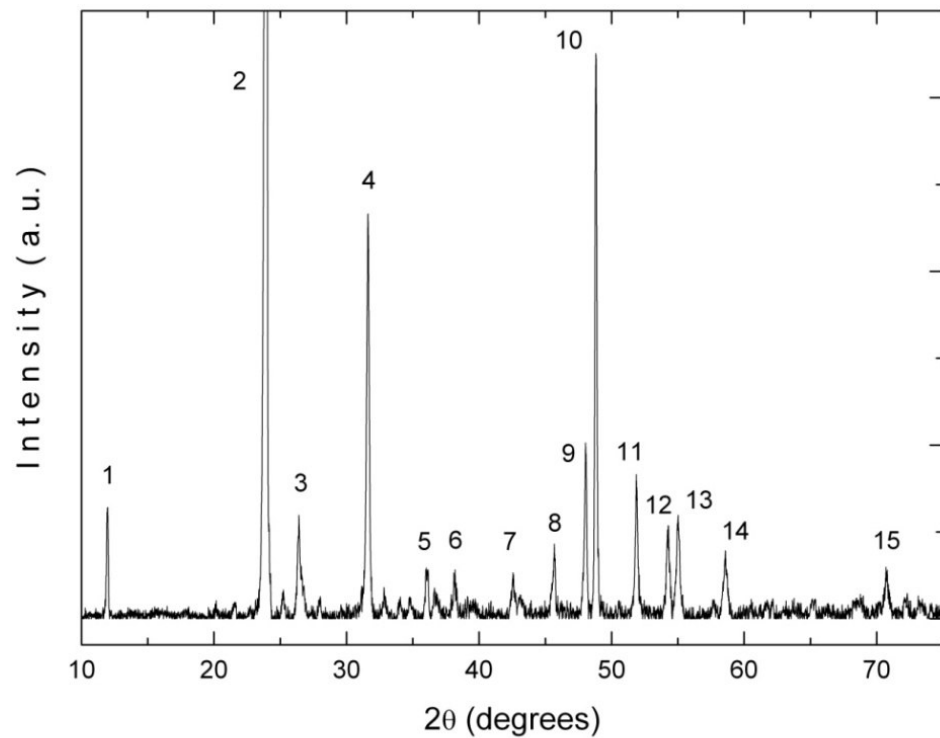


Figure 4.22. X-ray diffraction pattern of $\text{Tl}_4\text{In}_3\text{GaS}_8$ powder sample.

The calculated (using equation 2.12) and observed interplanar spacings were found to be in good agreement with each other. The lattice parameters of the monoclinic unit cell were found to be $a = 0.7376$, $b = 0.4178$, $c = 1.1487$ nm, and $\beta = 101.61^\circ$.

Table 4.3. X-ray powder diffraction data for $\text{Tl}_4\text{In}_3\text{GaS}_8$ crystal

No.	$h k l$	d_{obs} (nm)	d_{calc} (nm)	I/I_0
1	0 0 1	0.7232	0.7241	4
2	3 0 -1	0.3645	0.3646	100
3	2 1 0	0.3360	0.3358	3
4	4 0 0	0.2816	0.2815	13
5	4 0 -2	0.2478	0.2476	2
6	3 1 -2	0.2391	0.2390	2
7	5 0 -2	0.2110	0.2111	2
8	1 2 1	0.1958	0.1958	2
9	6 0 -1	0.1912	0.1912	6
10	2 2 1	0.1858	0.1859	18
11	1 0 4	0.1732	0.1731	4
12	6 1 0	0.1711	0.1712	3
13	4 2 -1	0.1680	0.1679	4
14	3 2 2	0.1569	0.1569	2
15	4 1 4	0.1326	0.1326	2

4.4.2 Results of EDSA Experiments

EDSA experiments were used to establish the chemical composition of $\text{Tl}_4\text{In}_3\text{GaS}_8$ crystals. Figure 4.23 shows the result of the EDSA experiment in 0-10 keV energy range. The composition of the studied samples (Tl:In:Ga:S) was estimated as 25.8:19.2:6.6:48.4, respectively. Furthermore, EDSA indicated that silicon impurities were present in the crystal.

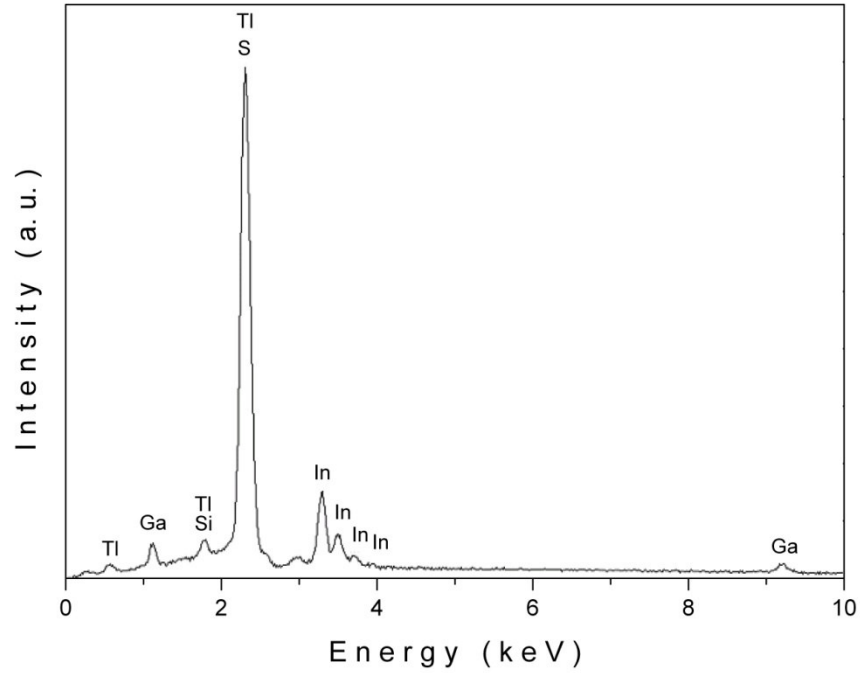


Figure 4.23. Energy dispersive spectroscopic analysis of $\text{Tl}_4\text{In}_3\text{GaS}_8$ crystal.

4.4.3 Results of Transmission and Reflection Experiments

The results of the transmission and reflection experiments for $\text{Tl}_4\text{In}_3\text{GaS}_8$ single crystals in 450-1100 nm wavelength range were presented in figure 4.24. As mentioned in section 2, n , k and α can be determined from the reflectivity and transmittance measurements by using equations 2.16 and 2.18. The reflectivity is measured using samples with natural cleavage planes and a thickness such that $\alpha x \gg 1$. The sample was then cleaved repeatedly using transparent adhesive tape to reduce its thickness until it was convenient for transmission measurements. The thickness was determined using transmission interference fringes at wavelengths slightly longer than the intrinsic absorption edge, i.e., in a region with relatively high transmission (figure 4.24) by the help of equation 2.21. For this purpose, the long wavelength value of the refractive index $n = 2.62$, obtained from the reflection measurements was used. In most cases the sample thickness was about 10 μm for room temperature transmission measurements.

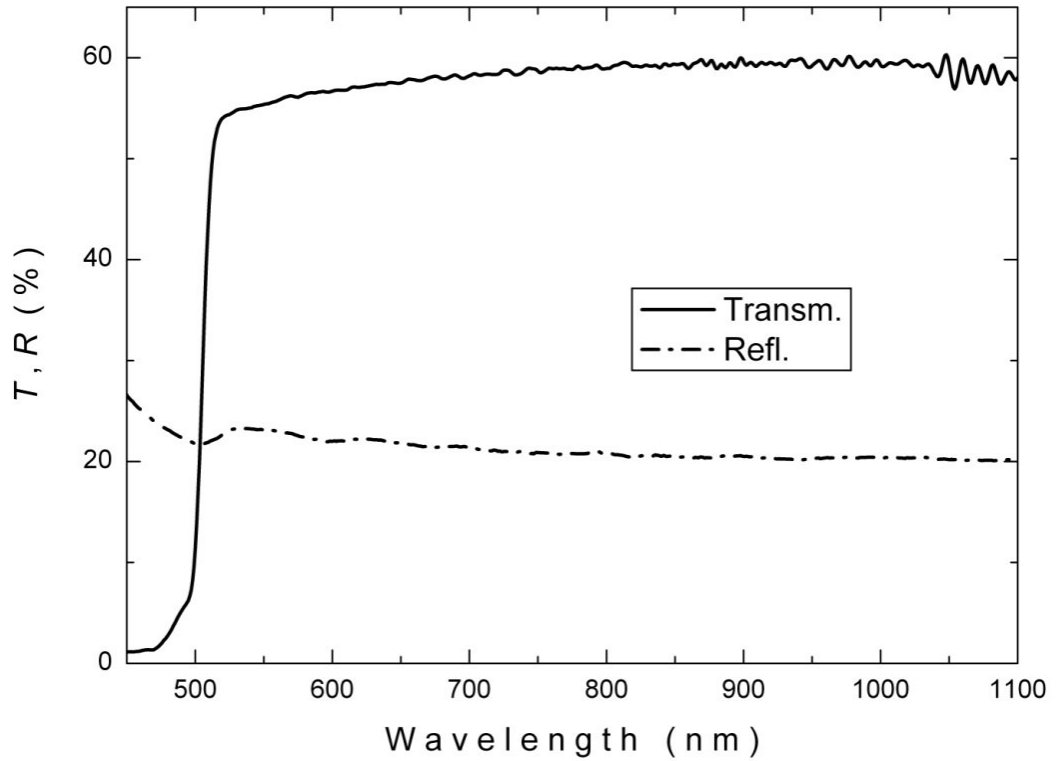


Figure 4.24. The spectral dependence of transmittance and reflectivity for $\text{Tl}_4\text{In}_3\text{GaS}_8$ crystal at $T = 300$ K.

The dependence of absorption coefficient on photon energy is analyzed in the high absorption regions to obtain the detailed information about the energy band gaps. As mentioned in chapter 2, the absorption coefficient α and photon energy can be related by equation 2.15. Figure 4.25 shows the calculated room temperature absorption coefficient α for $\text{Tl}_4\text{In}_3\text{GaS}_8$ crystal in the photon energy range 2.30-2.80 eV. It was revealed that α changes from 100 to 5060 cm^{-1} with increasing photon energy from 2.30 to 2.80 eV. Analysis of the experimental data shows that the absorption coefficient is proportional to $(h\nu - E_g)^p$ with $p = 2$ and $1/2$ for ranges 2.35-2.44eV and 2.58-2.76 eV, respectively. The dependencies of $(\alpha h\nu)^{1/2}$ and $(\alpha h\nu)^2$ on photon energy $h\nu$ are shown in the insets 1 and 2 of figure 4.25, respectively. The circles show the experimental data fitted to a linear equation (the solid lines) for finding the band gaps. The linear dependencies for the relations $(\alpha h\nu)^{1/2}$ and $(\alpha h\nu)^2$ versus $h\nu$ suggests the realization of indirect and direct allowed transitions for

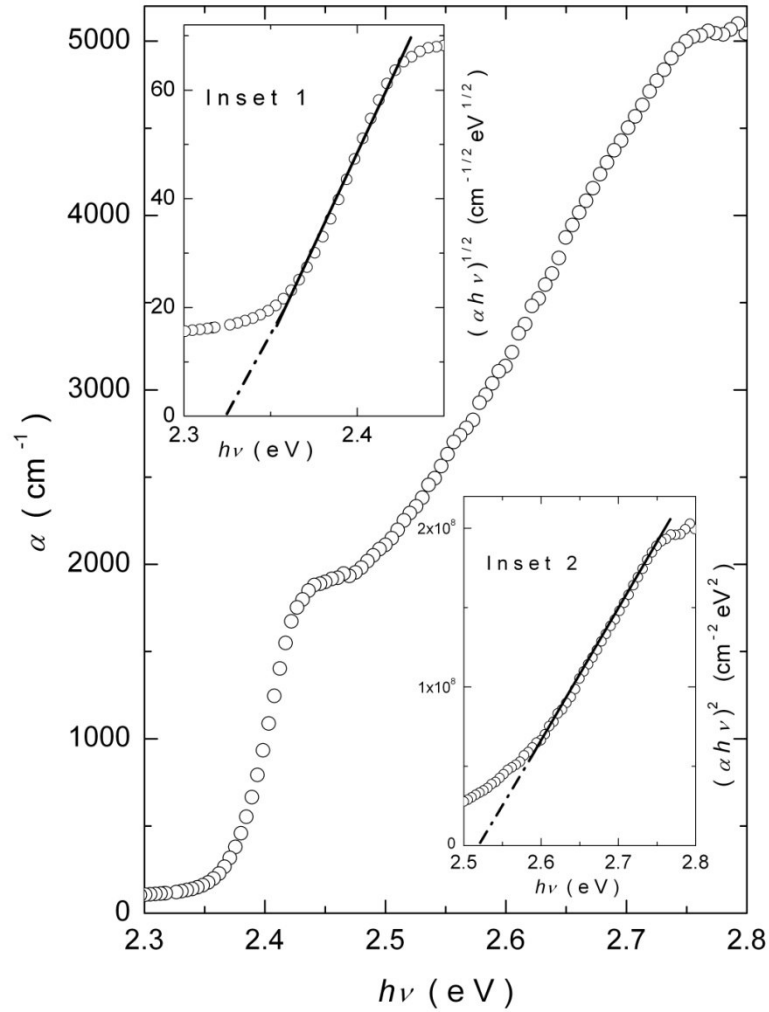


Figure 4.25. The variation of absorption coefficient of $\text{Tl}_4\text{In}_3\text{GaS}_8$ crystal as a function of photon energy at $T = 300$ K. Insets 1 and 2 represent the dependencies of $(ah\nu)^{1/2}$ and $(ah\nu)^2$ on photon energy, respectively.

$\text{Tl}_4\text{In}_3\text{GaS}_8$ crystal over the ranges 2.35-2.44eV and 2.58-2.76 eV, respectively. The extrapolations of the straight lines down to $(ah\nu)^{1/2} = 0$ and $(ah\nu)^2 = 0$ give the values of indirect and direct band gap energies $E_{\text{gi}} = 2.32 \pm 0.02$ eV and $E_{\text{gd}} = 2.52 \pm 0.02$ eV, respectively.

The transmission spectra for $\text{Tl}_4\text{In}_3\text{GaS}_8$ crystal registered in the temperature range of 10-300 K is shown in Figure 4.26. Since the thin layered samples were very

fragile, they broke into pieces at low temperatures. Therefore, the low-temperature measurements were carried out on thick samples (about 300 μm). Hence, the temperature dependence of only the indirect energy band gap (E_{gi}) could be analyzed. Technical reasons did not allow a direct measurement of the reflection at low temperatures. Hence, for the calculation of absorption coefficient α , the spectral dependence of room temperature reflectivity was uniformly shifted in energy according to the blue shift of the absorption edge.

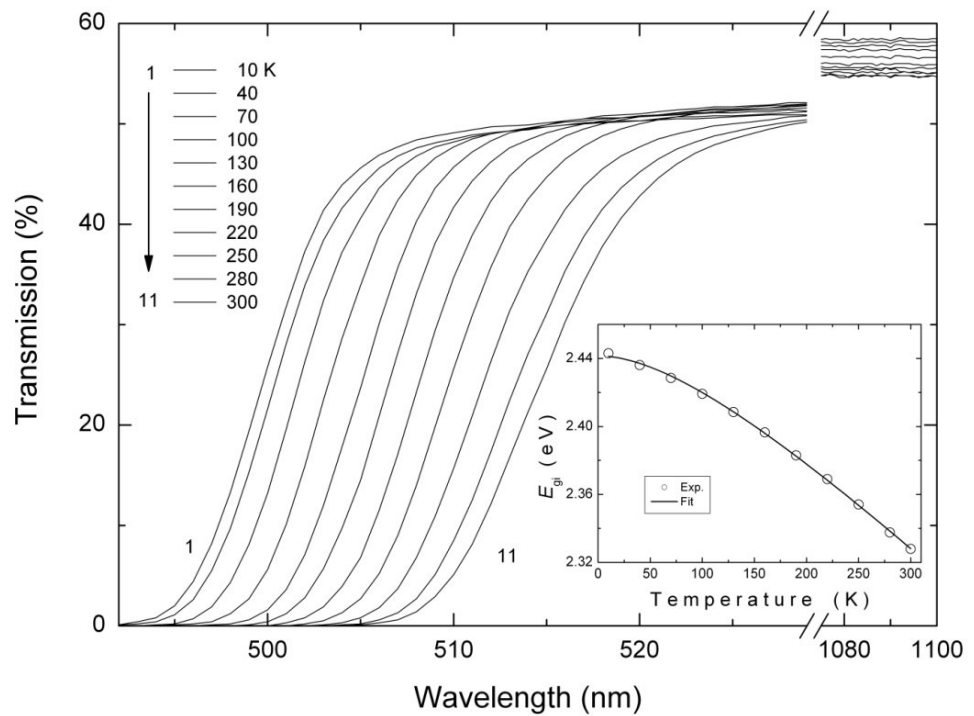


Figure 4.26. The spectral dependence of transmission for $\text{Tl}_4\text{In}_3\text{GaS}_8$ crystal in the temperature range of 10-300 K. Inset: the indirect band gap energy as a function of temperature. The solid line represents the fit using equation 2.10.

The inset of figure 4.26 shows the decrease in the obtained value of indirect transition energy gap with increasing temperature. Namely, it shifts from 2.44 to 2.32 eV as temperature increases from 10 to 300 K. The data of the $E_{gi} - T$ dependence (inset of figure 4.26) were fitted using equation 2.10, as done before. The fitting is represented by the solid line that revealed the fitting parameters as $E_{gi}(0) = 2.44$ eV, $\gamma = -6.0 \times 10^{-4}$ eV/K and $\beta = 180$ K. As a result of calculations with Lindemann's

melting rule [93], the Debye temperature for $\text{Tl}_4\text{In}_3\text{GaS}_8$ crystal was estimated to be $\beta = 173$ K, using X-ray results and the melting temperature $T_m = 1075$ K.

The refractive index n calculated using equations 2.14, 2.16 and 2.18 as a function of wavelength is shown in figure 4.27. The refractive index in the energy region of $h\nu < E_g$ gradually decreases from 2.86 to 2.62 with increasing wavelength in the range 538-1100 nm. The long wavelength value of refractive index is consistent with the values 2.7 ($\lambda = 800$ nm), 2.6 ($\lambda = 1100$ nm) and 2.6 ($\lambda = 1100$ nm) reported for TlInS_2 [99], TlGaS_2 [67] and $\text{Tl}_2\text{InGaS}_4$ [100] single crystals, respectively.

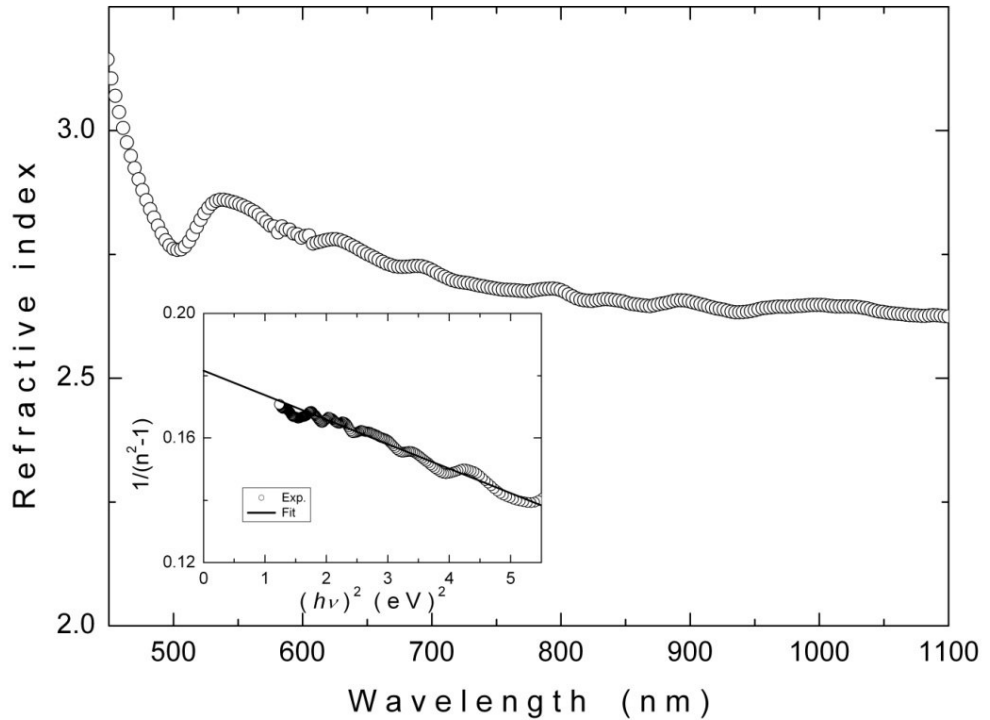


Figure 4.27. The dependence of refractive index on the wavelength for $\text{Tl}_4\text{In}_3\text{GaS}_8$ crystal. Inset: plot of $(n^2-1)^{-1}$ versus $(h\nu)^2$. The solid line represents the fit using equation 2.22.

As before, the dispersive refractive index data in $h\nu < E_g$ range were analyzed according to the single-effective-oscillator model proposed by Wemple and DiDomenico [60, 61], in which the refractive index is related to photon energy through the equation 2.22. Plotting $(n^2-1)^{-1}$ versus $(h\nu)^2$ allows the determination of

the oscillator parameters by fitting a linear function to the lower energy data range (1.13-2.32 eV). The fitting of the above reported function is presented in inset of figure 4.27. The zero-frequency refractive index n_0 is estimated by using equation 2.23. The values of the parameters E_{so} and E_d were calculated from the slope and the intersection with y-axis of the straight line (inset of figure 4.27) as 4.87 eV and 26.76 eV, respectively. Moreover, the values of zero-frequency dielectric constant $\epsilon_0 = n_0^2 = 6.50$ and refractive index $n_0 = 2.55$ were evaluated by means of equation 2.22. As mentioned before, the oscillator energy E_{so} is related empirically with the lowest direct band gap E_{gd} by the relationship $E_{so} \cong 2.0 E_{gd}$. The ratio E_{so}/E_{gd} for $Tl_4In_3GaS_8$ crystal, determined in this study, was found to be 1.93.

The refractive index n can be analyzed to determine the oscillator strength S_{so} for $Tl_4In_3GaS_8$ crystal. The refractive index can be represented by a single Sellmeier oscillator at low energies by using equation 2.25. The values of S_{so} and λ_{so} were calculated from $(n^2-1)^{-1}$ versus λ^{-2} plot as $8.48 \times 10^{13} \text{ m}^{-2}$ (130.37 eV^2) and $2.55 \times 10^{-7} \text{ m}$, respectively. As before, it is noticed that the obtained value of oscillator strength is of the same order as those obtained for ZnS, ZnSe, Ag_2S , $GeSe_2$ and $TlGaS_2$ crystals [61, 65, 67, 94].

4.4.4 Results of Photoluminescence Experiments

PL measurements in $Tl_4In_3GaS_8$ crystal were carried out by using two different excitation sources. Since our sample has a direct band gap of $E_{gd} = 2.64 \text{ eV}$ at $T = 26 \text{ K}$, 406 nm (3.05 eV) line of Hg-Xe arc lamp and a YAG:Nd³⁺ laser having a wavelength of $\lambda_{exc} = 532 \text{ nm}$ (2.33 eV) were used as the intrinsic and extrinsic excitation sources, respectively. The results of PL measurements done at $T = 26 \text{ K}$ with the excitation power of 17.7 mW cm^{-2} for intrinsic and 183.0 mW cm^{-2} for extrinsic excitation processes are presented in figure 4.28 for comparison. The figure reveals the presence of three PL bands centered at 514 nm (2.41 eV, A-band), 588 nm (2.11 eV, B-band) and 686 nm (1.81 eV, C-band) for extrinsic excitation. On the other hand, from the figure, we see that C-band is absent from the spectra of intrinsic excitation, although both A- and B-bands appear in it. Due to its more informative feature, we continued our experiments and analysis with the extrinsic excitation source only.

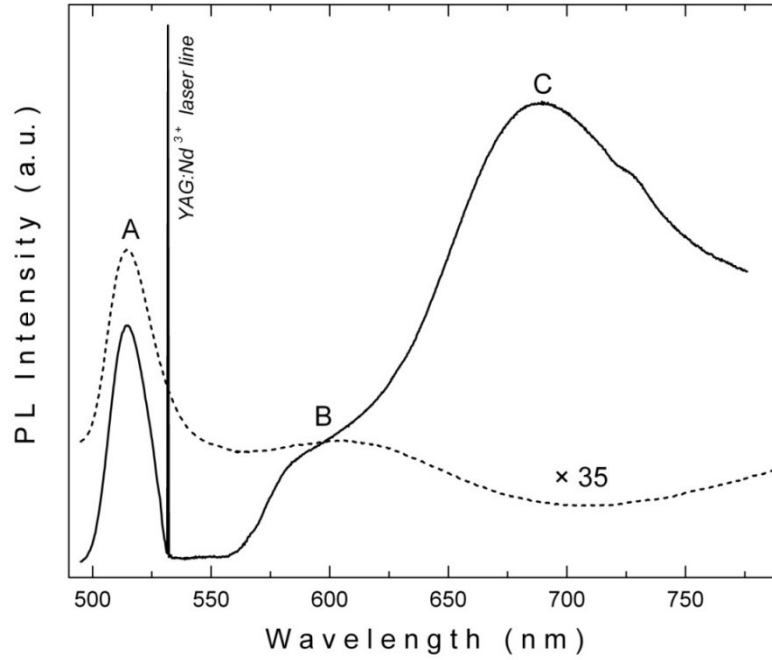


Figure 4.28. PL spectra of $\text{Tl}_4\text{In}_3\text{GaS}_8$ crystal under excitation of 532 nm line of a continuous frequency-doubled YAG:Nd^{3+} laser (solid curve) and 406 nm line of Hg-Xe arc lamp (dashed curve).

Note that for dashed curve, intensities have been multiplied by a factor of 35.

The dependence of the PL spectra on temperature provides important understanding of the nature and analysis of luminescence spectra. Therefore, temperature-dependent measurements were done in 500-780 nm wavelength range at a constant laser excitation intensity of $L = 183.0 \text{ mW cm}^{-2}$. The temperature-dependent spectra are separated into two parts as figure 4.29a, corresponding to 26-43 K temperature range, and figure 4.29b, corresponding to 36-130 K temperature range, in order to trace the behaviors of all bands clearly. In figures 4.29a and 4.29b, as previously mentioned, we observe three emission bands labeled as A-, B- and C-band having the full-width at half maximum (FWHM) values of 0.08, 0.18 and 0.28 eV, respectively. The figures show that the increasing temperature results in the variations of both peak energies and intensities for all bands. The peak energy variations of all bands are shown in figure 4.30. It is possible to observe that the peak intensities of A- and C-bands show a decreasing behavior and the peak energies

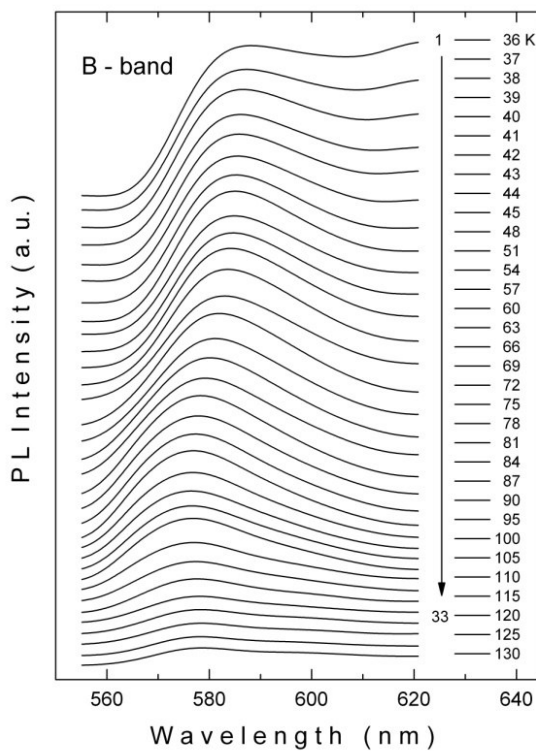
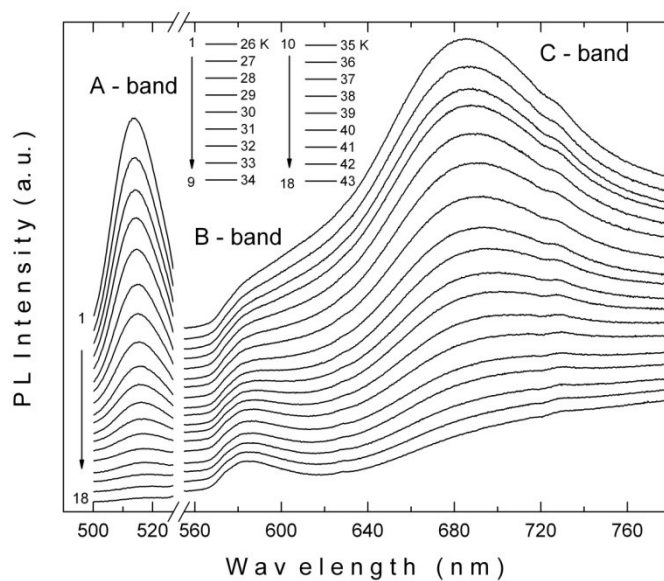


Figure 4.29. Temperature dependence of PL spectra from $Tl_4GaIn_3S_8$ crystals at excitation laser intensity $L = 183.0 \text{ mW cm}^{-2}$: (a) A-, B- and C-bands in the 26-43 K temperature range and 500-780 nm wavelength region; (b) B-band in the 36-130 K temperature range and 555-620 nm wavelength region.

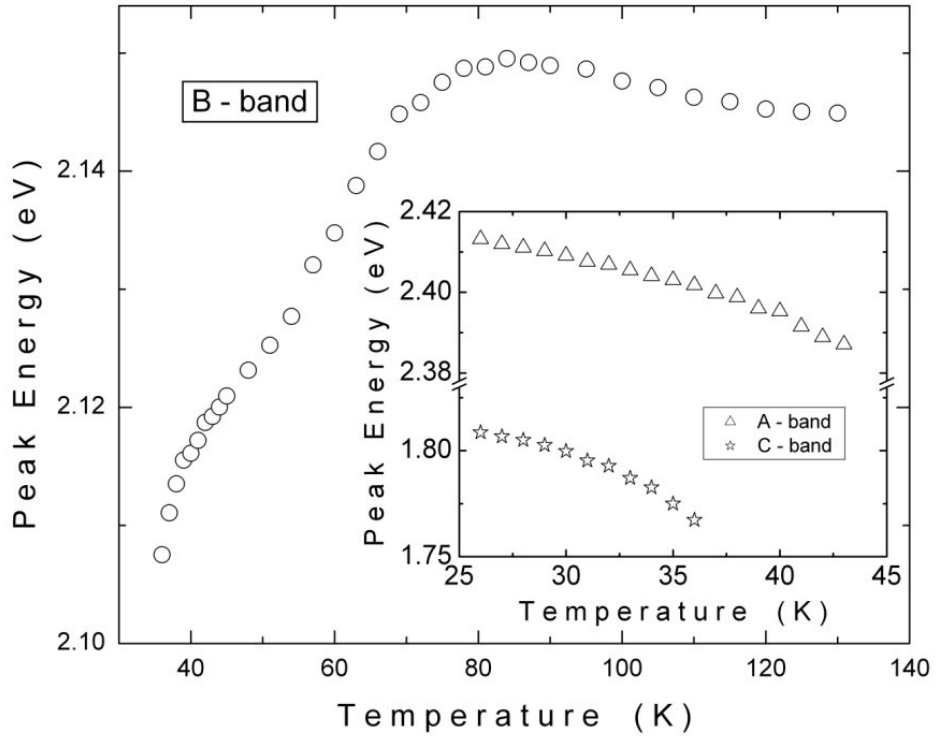


Figure 4.30. Temperature dependencies of emission A-, B- and C-band peak energies of $\text{Tl}_4\text{In}_3\text{GaS}_8$ crystal.

shift to lower energies with increasing temperature. However, the temperature behavior of the B-band is somewhat different from that of the other bands; its intensity decreases with increasing temperature, whereas its peak energy increases up to a maximum value at $T = 84$ K and then starts to decrease. The experimental data for the temperature dependence of PL band intensity can be fitted by the equation 2.41. Figure 4.31 shows the temperature dependence of the emission band maximum intensities of all bands as a function of the reciprocal temperature in the 26-130 K range. After a nonlinear least squares fit, the quenching activation energies for emission bands are found to be 0.03, 0.02 and 0.01 eV for A-, B- and C-bands, respectively. Since $\text{Tl}_4\text{In}_3\text{GaS}_8$ crystal is an n-type semiconductor, we consider that the activation energies of 0.03 and 0.01 eV belonging to A- and C-bands are associated with donor levels located below the bottom of the conduction band.

The most striking feature of the emission spectra is the temperature dependence of B-band peak energy (figure 4.30). In contrast with the peak energy behavior of the A-

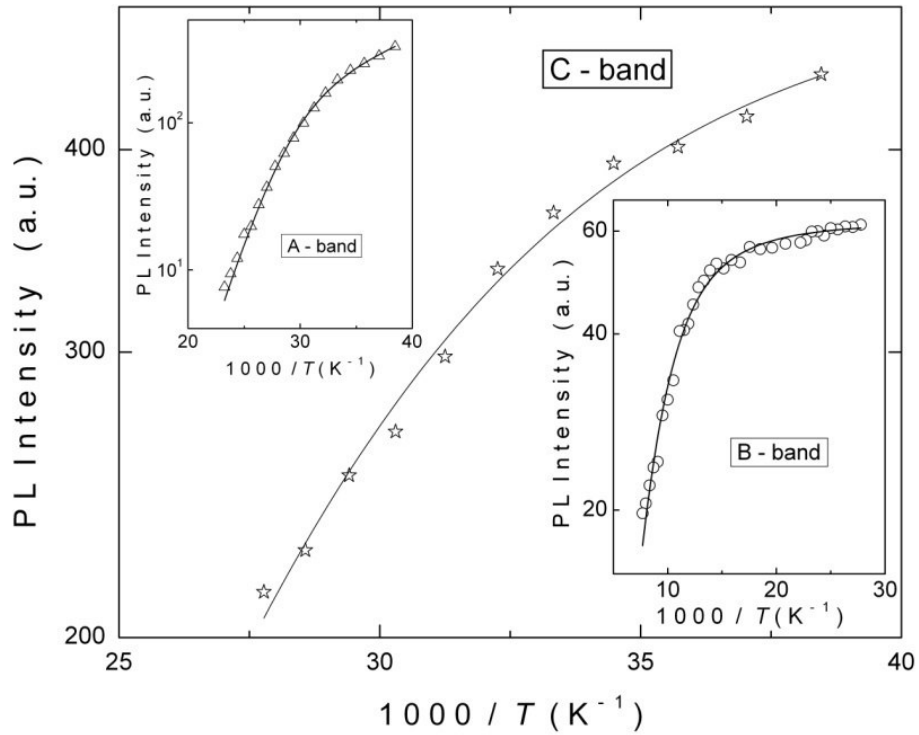


Figure 4.31. Temperature dependencies of PL band intensities for $\text{Tl}_4\text{In}_3\text{GaS}_8$ crystal. Triangles, stars and circles are the experimental data. Solid curves show the theoretical fits using equation 2.40.

and C-bands, the peak energy of the B-band blue shifts by almost 42 meV until 84 K. Such behavior is typically understood in terms of a configurational coordinate (CC) model of defects [54]. As will be shown later on, the activation energy corresponding to B-band is actually associated with the difference between the minimum of the excited state and the intersection point of the excited and ground state CC curves rather than the difference between the minimum of conduction band and a shallow donor level.

The laser excitation intensity dependence of PL spectra also provides valuable information about the recombination mechanism responsible for the observed luminescence. Excitation intensity-dependent PL measurements were done at two different temperatures, namely 26 K (A- and C-bands) and 50 K (B-band). For the analysis, we plotted two different figures to trace the behaviors of the PL bands with respect to excitation laser intensity variations clearly. Figures 4.32a and 4.32b show the PL spectra of the $\text{Tl}_4\text{In}_3\text{GaS}_8$ crystal measured in the 0.9-183.0 and 4.4-

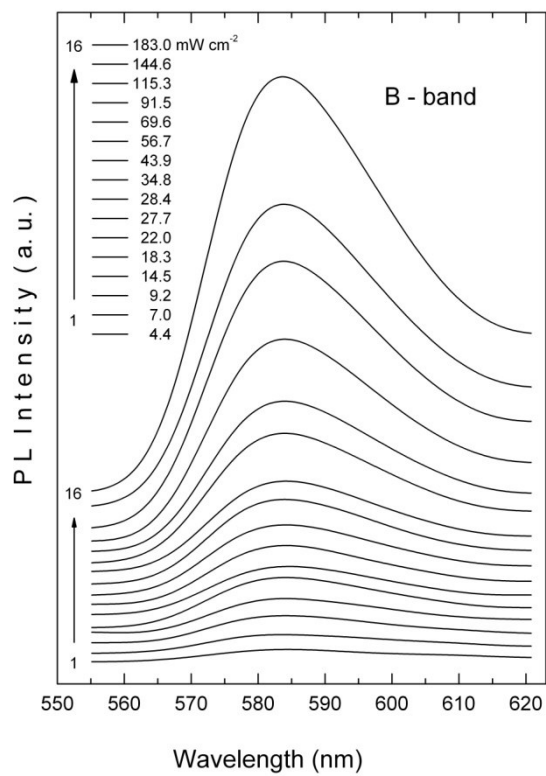
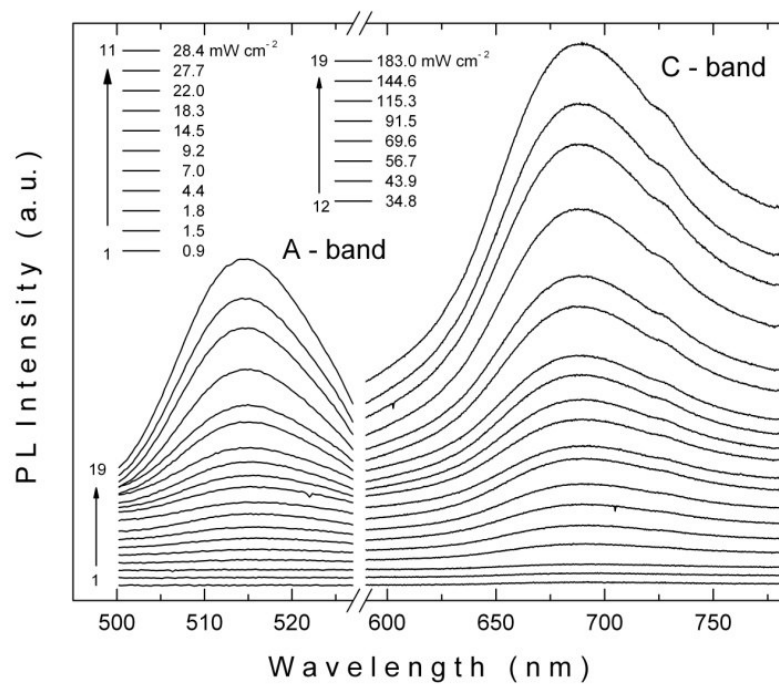


Figure 4.32. PL spectra of $\text{Tl}_4\text{In}_3\text{GaS}_8$ crystal as a function of excitation intensity: (a) A- and C-bands at $T = 26$ K; (b) B-band at $T = 50$ K.

183.0 mW cm⁻² laser excitation intensity ranges, respectively. From these spectra, we obtained the information about the peak energy and intensity for emission bands at different laser excitation intensities. A detailed analysis of emission bands as a function of the laser excitation intensity did not yield any variation of the peak energies. We, therefore, concentrated on the analysis of the band intensities as a function of the excitation laser intensity. It is seen that the band intensities of all bands at peak maximum increases with increasing laser excitation intensity values. To follow the behavior of emission bands more thoroughly, we plotted the PL emission band maximum intensity versus excitation laser intensity graphs in logarithmic scale (figure 4.33). The common behaviors of the emission bands with respect to excitation laser intensity are clearly demonstrated by this graph. For the analysis, the experimental data for emission bands in the spectra were fitted by the power law of the form of equation 2.33. We found that PL intensity for all bands increase sublinearly with increasing excitation intensity. From the fit of the experimental data, we obtained γ values as 0.95, 0.94 and 0.95 for A-, B- and C-bands, respectively. As mentioned in chapter 2, the exponent γ is generally $1 < \gamma < 2$ for free- and bound-exciton emission, whereas $0 < \gamma \leq 1$ is typical for free-to-bound and donor-acceptor pair recombination.

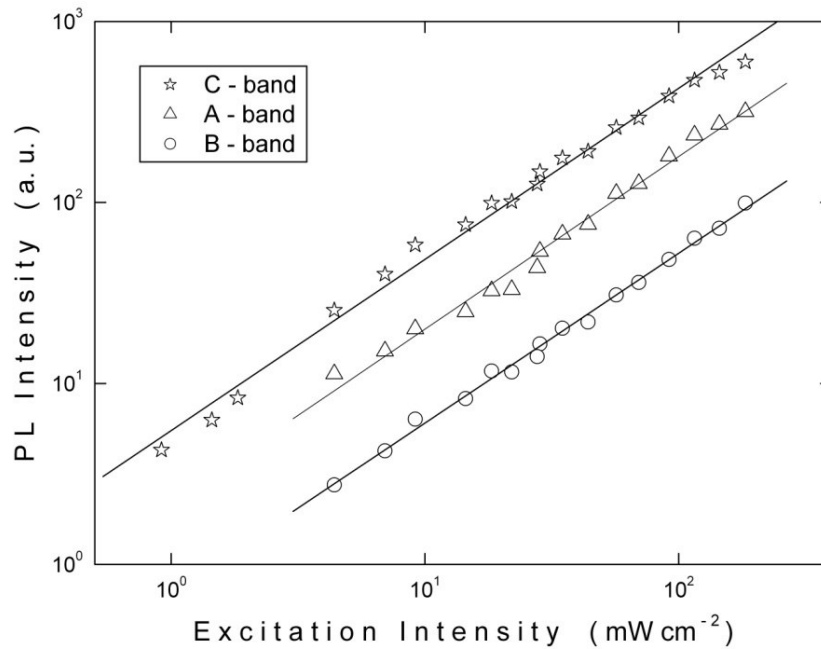


Figure 4.33. Dependencies of PL intensities at the emission band maxima on the excitation intensities for Tl₄In₃GaS₈ crystal. The solid lines show the theoretical fits using equation 2.33.

The analysis of the PL spectra as a function of temperature and excitation intensity allows one to obtain a possible scheme for the donor-acceptor levels involved in the radiative recombination processes observed in this study. Figure 4.34 shows this proposed model. As seen from the figure, two shallow donor levels responsible for the appearance of the A- and C-bands are placed at $E_{d1} = 0.03$ eV and $E_{d3} = 0.01$ eV below the bottom of the conduction band. For the emission energy of the donor-acceptor pair, we recall equation 2.7, defined in chapter 2, as

$$E = E_g - E_a - E_d + \frac{e^2}{\epsilon r}. \quad (2.7)$$

The fourth term in the expression is a correction for Coulomb interaction between pairs and may be effective only at short distances and so can be neglected. Neglecting this term, we revealed the acceptor levels located above the top of the valence band at $E_{a1} = 0.20$ eV and $E_{a3} = 0.82$ eV. The high resistivity of our samples indicates that the concentration of acceptors is high enough to efficiently compensate the donors. Taking the above considerations into account, the observed A- and C-bands in the emission spectra has been attributed to the radiative recombination of electrons occupying the donor levels $E_{d1} = 0.03$ eV and $E_{d3} = 0.01$ eV with the holes occupying the acceptor levels $E_{a1} = 0.20$ eV and $E_{a3} = 0.82$ eV, respectively. It is well-known that for donor-acceptor pair transitions, the emission energy decreases along with the band gap energy when the temperature is increased [70]. At low temperatures, photoexcited charge carriers are bound to donors and acceptors and recombine with closest neighbors. Due to thermal emission of carriers bound to acceptor and donor levels, an increase in the pair separation R with increasing temperature is expected. As a result of this increase, the pairs that are apart also play role in the recombination process. As equation 2.7 makes it clear, contributions from the distant pairs result in red shift of the peak energy of the bands (figure 4.30).

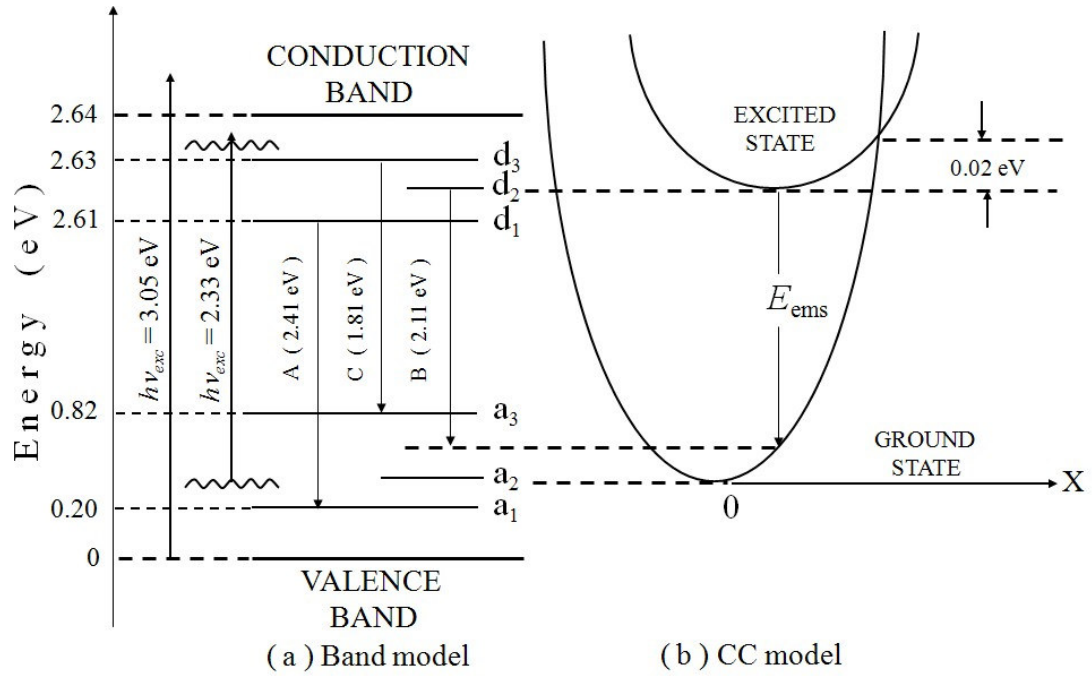


Figure 4.34 Band model (a) and configurational coordinate (CC) model (b) for $\text{Tl}_4\text{In}_3\text{GaS}_8$ crystal.

In addition to temperature-dependent analysis, sublinear variation of PL intensity with excitation laser intensity is also consistent with donor-acceptor recombination. Our analysis shows that the peak energy positions of the observed bands do not shift with increasing laser excitation intensity in line with the fact that the states involved in the recombination are indeed close pairs. If the donor-acceptor pair distances were heterogeneous in nature, then according to equation 2.7, increasing the excitation laser intensity would result in blue shift of the peak energies of the observed PL bands, which clearly was not observed.

In figure 4.34, we also present CC model for the B-band in PL spectra. In this model, it was assumed that the ground state of localized center is derived from an acceptor level a_2 , while the excited state originates from a sulfur vacancy donor level d_2 , and zero point of both states lies within the band gap. Since $\text{A}^{\text{III}}\text{B}^{\text{VI}}$ -type layered crystals are more polar than covalent [101], the displacement of the excited state minimum is expected to be reasonably large. Therefore, the observed quenching of the B-band with increasing temperature is due to an increased electron population of the excited state at higher displacement coordinates. The electrons involved in this process return to the ground state through a nonradiative process. Thus, the

activation energy of 0.02 eV, obtained from thermal quenching of the B-band, is the difference between the minimum of the excited state and the intersection point of the excited and ground state CC curves. Generally, in compound semiconductors a deviation from stoichiometry generates donors in the case of anion vacancies. The acceptor level a_2 above the top of valence band may be linked, as in the case of GaSe crystals [102], to the uncontrolled impurities, point defects, and stacking faults, which are due to the weak interlayer interactions in studied crystals. Electron transitions from the excited states of the donor level to the ground states of the acceptor level give rise to the PL with photon energy E_{ems} .

Another striking feature of the PL spectra of the $\text{Tl}_4\text{In}_3\text{GaS}_8$ crystal is the absence of the C-band in the case of intrinsic excitation process, as seen in figure 4.28. For intrinsic excitation case ($\lambda_{\text{exc}} = 406 \text{ nm}$) with low laser excitation intensity of $L = 17.7 \text{ mW cm}^{-2}$, it is probable that the quasi-Fermi level for electrons is located above only the donor states d_1 and d_2 (figure 4.34), which is sufficient to observe A- and B-bands in the PL spectra (figure 4.28). On the other hand, for extrinsic excitation ($\lambda_{\text{exc}} = 532 \text{ nm}$) with high laser excitation intensity of $L = 183.0 \text{ mWcm}^{-2}$, the quasi-Fermi level for electrons is shifted, and the number of excited electrons is large enough to fill in the donor level d_3 as well, responsible for the observed C-band emission (figure 4.33). Therefore, we could observe C-band emission along with the A- and B-bands in the PL spectra (figure 4.28).

4.5 Results of the Structural and Optical Characterization Experiments for $\text{Tl}_2\text{InGaS}_4$ crystal

The compound $\text{Tl}_2\text{InGaS}_4$ belongs to the layered semiconductors group. This crystal is a structural analogue of TlInS_2 and TlGaS_2 , in which half of the indium (gallium) atoms are replaced by gallium (indium) atoms [5, 92]. The crystal lattice consists of alternating two-dimensional layers arranged parallel to the (001) plane. Interlayer bonding in $\text{Tl}_2\text{InGaS}_4$ is formed between Tl and S atoms while the bonding between In(Ga) and S atoms is of the intralayer type. The projections of the crystal structure on the ac - and ab -planes are presented in figure 4.10. The fundamental structural unit of a layer is the $\text{In}_4(\text{Ga}_4)\text{S}_{10}$ polyhedron representing a combination of four elementary tetrahedral $\text{In}(\text{Ga})\text{S}_4$ linked together by bridging S atoms. The thallium

atoms are located in trigonal prismatic voids resulting from the combination of the $\text{In}_4(\text{Ga}_4)\text{S}_{10}$ polyhedra into a layer.

The electrical conductivity of the studied sample was n-type as established by the hot probe method. Crystals suitable for PL measurements had typical sample dimensions of $4 \times 3 \times 0.7 \text{ mm}^3$. After cleaving, the resulting ingot appears yellow-green in color and the freshly cleaved surfaces were mirror-like.

4.5.1 Results of X-Ray Experiments

The structure of $\text{Tl}_2\text{InGaS}_4$ crystals was defined by the X-ray powder diffraction experiments. X-ray diffractogram of $\text{Tl}_2\text{InGaS}_4$ is shown in figure 4.35. As a result of the analysis, the obtained Miller indices (hkl), the observed and calculated interplanar spacings (d) and the relative intensities (I/I_0) of the diffraction lines are listed in table 4.4.

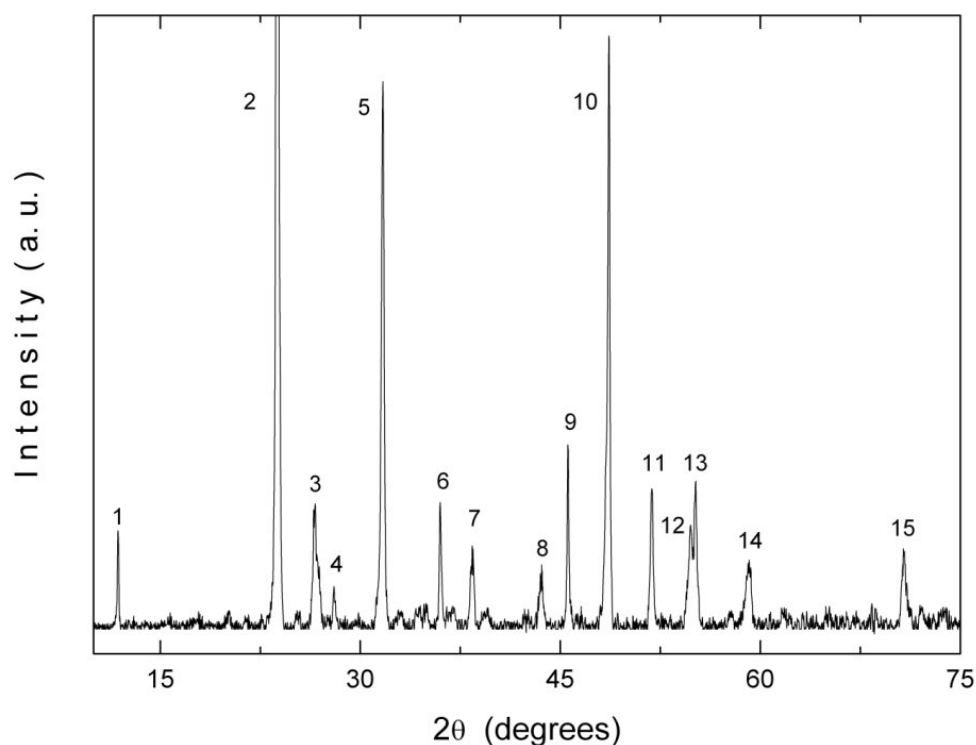


Figure 4.35. X-ray diffraction pattern of a $\text{Tl}_2\text{InGaS}_4$ powder sample.

Table 4.4. X-ray powder diffraction data for $\text{Tl}_2\text{InGaS}_4$ crystals.

No.	h k l	d_{obs} (nm)	d_{calc} (nm)	I/I_0
1	1 0 -1	0.7468	0.7460	3
2	2 0 -2	0.3735	0.3736	100
3	0 1 1	0.3346	0.3345	4
4	1 1 1	0.3182	0.3185	2
5	0 1 2	0.2820	0.2821	15
6	3 0 -3	0.2493	0.2492	4
7	3 1 -2	0.2338	0.2339	2
8	4 1 -2	0.2078	0.2077	2
9	5 0 2	0.1989	0.1987	5
10	4 0 -4	0.1870	0.1870	16
11	5 0 3	0.1762	0.1761	4
12	0 2 2	0.1674	0.1674	3
13	1 2 -2	0.1664	0.1664	4
14	6 0 3	0.1561	0.1562	2
15	2 1 6	0.1332	0.1332	2

The calculated (using equation 2.12) and observed interplanar spacings were found to be in good agreement with each other. The lattice parameters of the monoclinic unit cell were found to be $a = 0.9133$, $b = 0.3603$, $c = 1.1604$ nm, and $\beta = 95.20^\circ$. Small amounts of the detected impurities are expected to reside at the interstitial positions. We assume that they do not change the calculated lattice parameters within our cited accuracy.

4.5.2 Results of EDSA Experiments

The chemical composition of $\text{Tl}_2\text{InGaS}_4$ crystals was established by EDSA experiments. The result of the EDSA experiment in 0-10 keV energy range is displayed in figure 4.36. The composition of the studied samples (Tl:In:Ga:S) was found as 25.9:13.0:13.1:48.0, respectively. Moreover, the presence of silicon impurities in the crystal was indicated by EDSA.

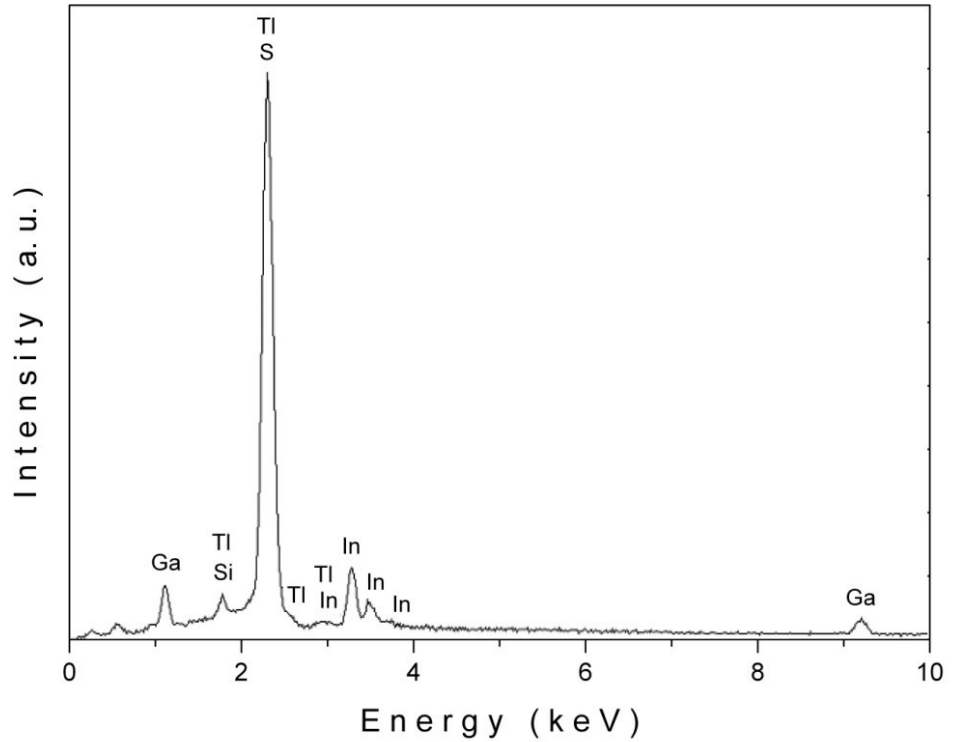


Figure 4.36. Energy dispersive spectroscopic analysis of $\text{Tl}_2\text{InGaS}_4$ crystal.

4.5.3 Results of Transmission and Reflection Experiments

Figure 4.37 shows the transmittance (T) and reflectivity (R) spectra recorded in the 400-1100 nm wavelength range for $\text{Tl}_2\text{InGaS}_4$ single crystals. As mentioned in section 2, the determination of n , k and α can be done from the reflectivity and transmittance measurements by using equations 2.16 and 2.18. The reflectivity is measured using specimens with natural cleavage planes and a thickness such that $\alpha x \gg 1$. The sample is then reduced in thickness until it is convenient for transmission measurements by repeated cleaving using transparent adhesive tape. The sample thickness was determined using transmission interference fringes at a wavelength slightly longer than the intrinsic absorption edge where the sample has relatively high transmission values (figure 4.37) by the help of equation 2.21. The long-wavelength value of the refractive index $n = 2.60$, found from reflection

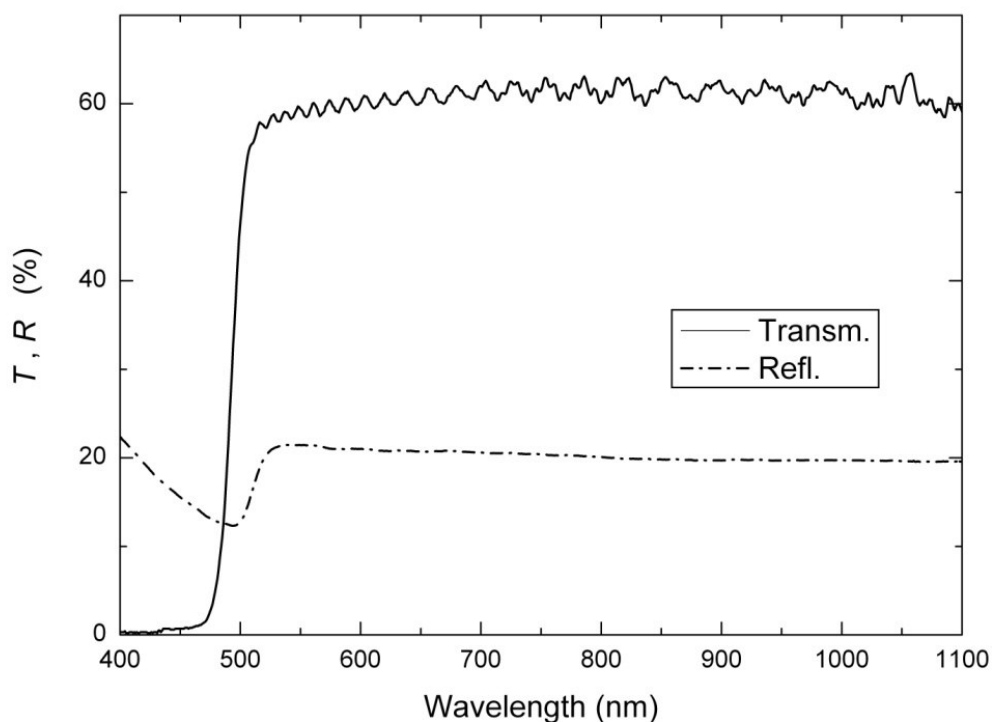


Figure 4.37. The spectral dependence of transmittance and reflectivity for $\text{Tl}_2\text{InGaS}_4$ crystal at $T = 300 \text{ K}$.

measurements, was used to determine the thickness of the sample, which turned out to be about $10 \mu\text{m}$ for room temperature transmission measurements in most of the cases.

The analysis of the dependence of absorption coefficient on photon energy in the high absorption regions is carried out to obtain the detailed information about the energy band gaps. As mentioned, the absorption coefficient α and photon energy can be related by equation 2.15. Figure 4.38 shows the calculated room temperature absorption coefficient α for $\text{Tl}_2\text{InGaS}_4$ crystal in the photon energy range 2.30-2.70 eV. It was found that α changes from 70 to 3800 cm^{-1} with increasing photon energy from 2.30 to 2.70 eV. The analysis of the experimental data showed that the absorption coefficient is proportional to $(h\nu - E_g)^p$ with $p = 2$ in the energy range 2.20-2.54 eV and $p = 1/2$ in the energy range 2.56-2.70 eV. Insets 1 and 2 of figure 4.38 display the dependences of $(\alpha h\nu)^{1/2}$ and $(\alpha h\nu)^2$ on photon energy $h\nu$,

respectively. The circles are the experimental data that were fitted to a linear equation (the solid lines) for finding the band gaps. Linear dependences were

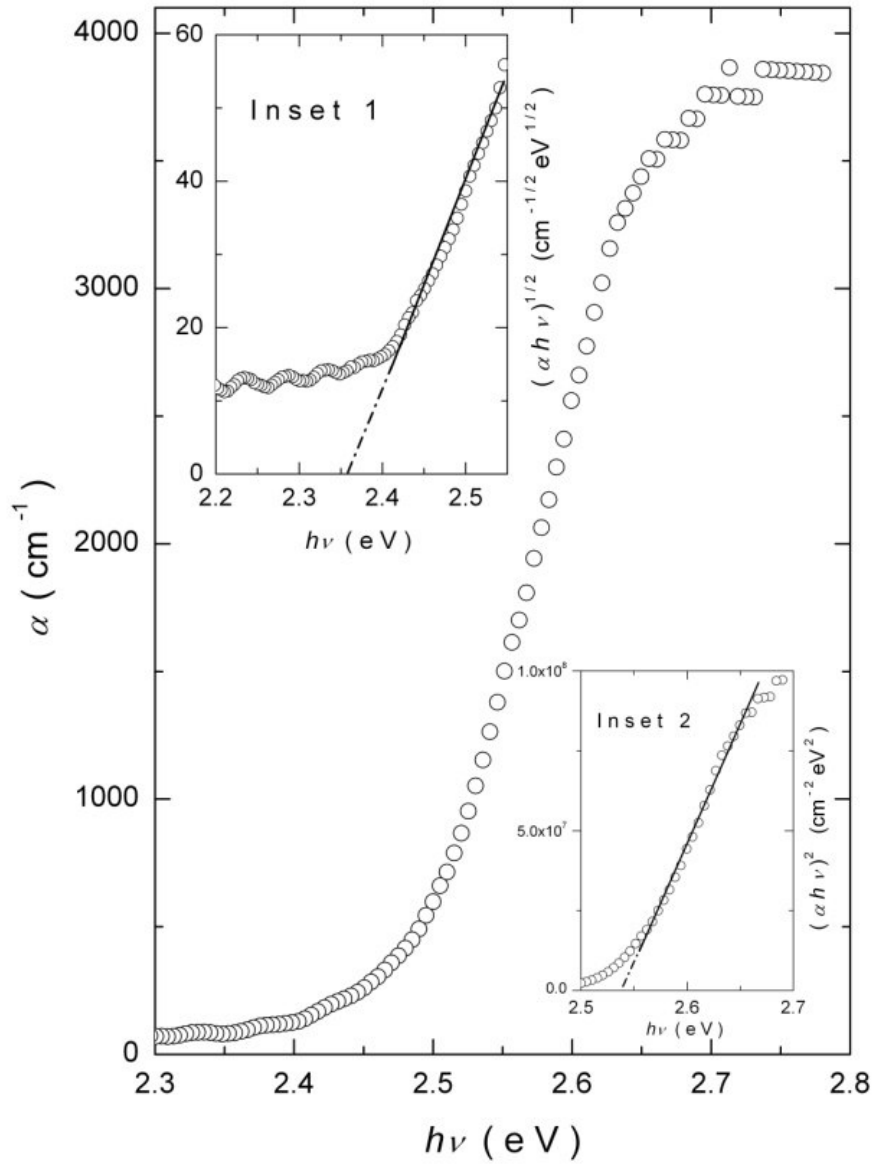


Figure 4.38. The variation of absorption coefficient as a function of photon energy at $T = 300$ K. Insets 1 and 2 represent the dependences of $(\alpha h\nu)^{1/2}$ and $(\alpha h\nu)^2$, respectively, on photon energy.

observed for the relations $(ahv)^{1/2}$ and $(ahv)^2$ versus hv . This suggests the realization of indirect and direct allowed transitions for Tl_2InGaS_4 crystal over the ranges 2.20-2.54 and 2.56-2.70 eV, respectively. The extrapolations of the straight lines down to $(ahv)^{1/2} = 0$ and $(ahv)^2 = 0$ give the values of indirect and direct band gap energies $E_{gi} = 2.35 \pm 0.02$ and $E_{gd} = 2.54 \pm 0.02$ eV, respectively.

Figure 4.39 shows the transmission spectra for Tl_2InGaS_4 crystal registered in the temperature range of 10-300 K. Since the thin layered samples broke into pieces at low temperatures due to their excessive fragility, the low temperature measurements could only be carried out on thick samples (about 200 μm). As a consequence, the analysis of the temperature dependence could be done for only the indirect energy band gap (E_{gi}). For technical reasons, we were unable to measure the reflection at low temperatures directly. Therefore, for the calculation of the absorption coefficient α , the spectral dependence of room temperature reflectivity was uniformly shifted in energy according to the blue shift of the absorption edge.

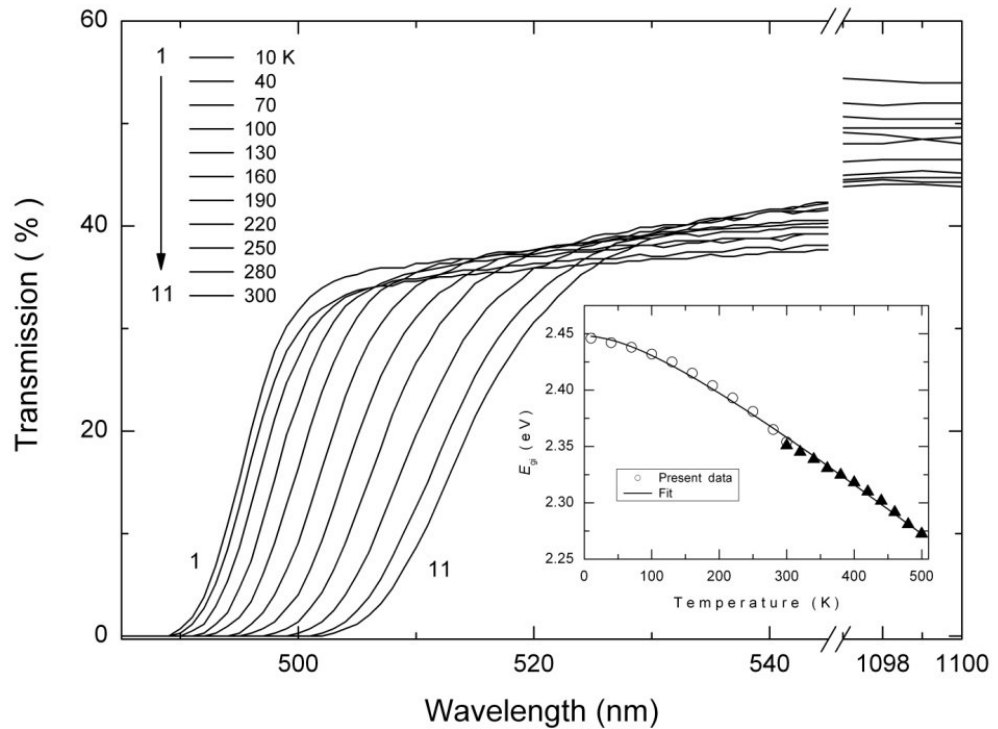


Figure 4.39. The spectral dependence of transmittance for Tl_2InGaS_4 crystal in the temperature range 10-300 K. Inset: the indirect band gap energy as a function of temperature. The solid line represents the fit using equation 2.10. Experimental data (solid triangles) were taken from Ref. [103].

The decrease of the obtained value of the indirect transition energy gap from 2.45 to 2.35 eV with increasing temperature from 10 to 300 K is illustrated in the inset of figure 4.39. The experimental data for the indirect energy band gap of $\text{Tl}_2\text{InGaS}_4$ crystal in the high temperature range of 300-500 K were taken from [103]. The data of the $E_{\text{gi}} - T$ dependence (inset of figure 4.39) were fitted using equation 2.10. The fitting of equation 2.10 is represented by the solid line in the figure. The fitting parameters were found to be $E_{\text{gi}}(0) = 2.45$ eV, $\gamma = -4.70 \times 10^{-4}$ eV/K and $\beta = 169$ K. The Debye temperature for $\text{Tl}_2\text{InGaS}_4$ crystal was found to be $\beta = 173$ K, estimated by Lindemann's melting [93] rule using X-ray results and a melting temperature $T_m = 1103$ K.

Figure 4.40 shows the change of refractive index n calculated using equations 2.14, 2.16 and 2.18 as a function of wavelength. As seen from this figure, the refractive index in the energy region of $h\nu < E_g$ gradually decreases from 2.72 to 2.60 with increasing wavelength in the range 543-1100 nm. The long wavelength value of refractive index is consistent with the values 2.7 ($\lambda = 800$ nm) and 2.6 ($\lambda = 1100$ nm) reported for TlInS_2 [99] and TlGaS_2 [67] single crystals, respectively.

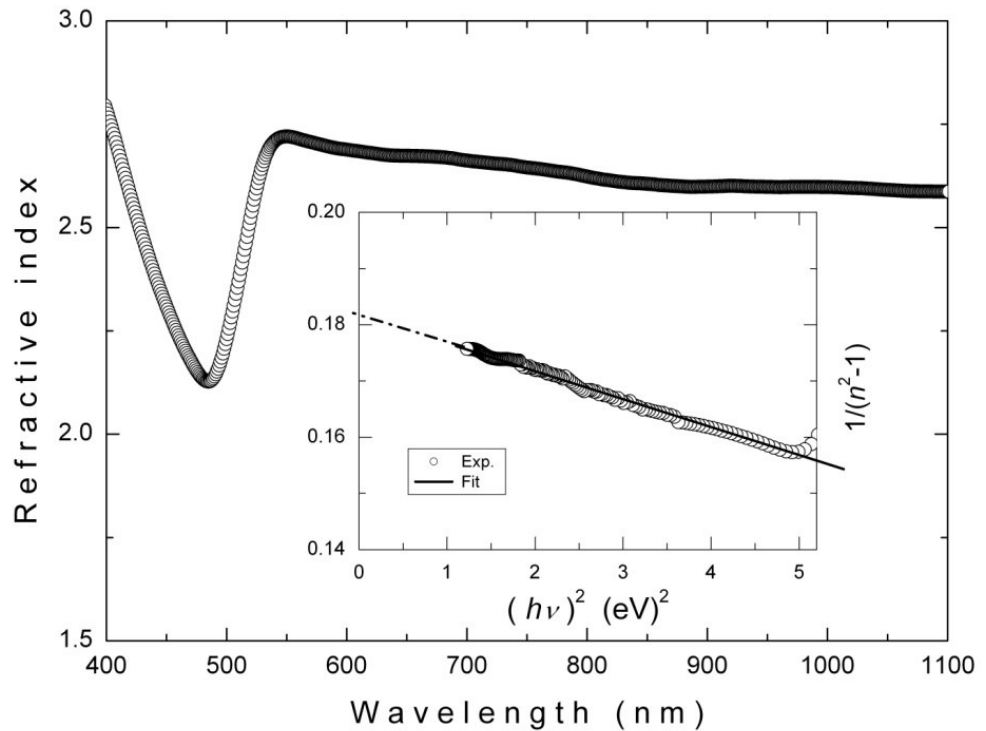


Figure 4.40. The dependence of refractive index on the wavelength for $\text{Tl}_2\text{InGaS}_4$ crystal. Inset: plot of $(n^2 - 1)^{-1}$ versus $(h\nu)^2$. The solid line represents the fit using equation 2.22.

The dispersive refractive index data in $h\nu < E_g$ range were analyzed according to the single-effective-oscillator model proposed by Wemple and DiDomenico [60, 61]. According to this model, the refractive index is related to photon energy through the equation 2.22 and plotting $(n^2 - 1)^{-1}$ versus $(h\nu)^2$ allows the determination of the oscillator parameters by fitting a linear function to the lower energy data range (1.13-2.25 eV). The fitting of the above reported function is presented in the inset of figure 4.40. The zero-frequency refractive index n_0 is estimated with the help of equation 2.23. By using the slope and the intersection with y-axis of the straight line (inset of figure 4.40), the values of the parameters E_{so} and E_d were calculated to be 5.73 and 31.46 eV, respectively. Furthermore, the values of the zero-frequency dielectric constant $\epsilon_0 = n_0^2 = 6.49$ and refractive index $n_0 = 2.55$ were calculated equation 2.22. As mentioned before, the oscillator energy E_{so} is associated empirically with the lowest direct band gap E_{gd} through the relationship $E_{so} \cong 2.0 E_{gd}$. The ratio E_{so}/E_{gd} for Tl_2InGaS_4 crystal was determined to be 2.25 in this study.

To determine the oscillator strength S_{so} for Tl_2InGaS_4 crystal, the analysis of refractive index n can be used. The refractive index is represented by a single Sellmeier oscillator at low energies by equation 2.25. The values of S_{so} and λ_{so} were found from $(n^2-1)^{-1}$ versus λ^{-2} plot to be $11.72 \times 10^{13} \text{ m}^{-2} (180.27 \text{ eV}^2)$ and $2.16 \times 10^{-7} \text{ m}$, respectively. As before, it is seen that the value obtained for the oscillator strength is of the same order as those obtained for ZnS, ZnSe, Ag_2S , $GeSe_2$ and $TlGaS_2$ crystals [61, 65, 67, 94].

4.5.4 Results of Photoluminescence Experiments

In the PL experiment, we observed three bands (labeled as A, B and C), dominating in the spectra at different excitation intensities. For the analysis, we plotted two different figures to observe the behaviors of the PL bands with respect to temperature variations. Figure 4.41 shows the PL spectra of the Tl_2InGaS_4 crystal measured in the 500-750 nm wavelength and the 15-55 K temperature ranges at constant laser excitation intensity of $L = 0.11 \text{ Wcm}^{-2}$ for the B-band centered at 607 nm (2.04 eV). Likewise, figure 4.42 shows the PL spectra measured in the 475-800 nm wavelength and the 15-150 K temperature ranges at a constant laser excitation intensity of $L =$

56.36 Wcm^{-2} for the A- and the C-bands centered at 542 nm (2.29 eV) and 707 nm (1.75 eV), respectively. For clarity, the 475-600 nm region of the spectra is multiplied by a factor of four in figure 4.42. From figure 4.42, the C-band is seen to be the same band observed in previous PL studies of the $\text{Tl}_2\text{InGaS}_4$ crystal [96], so we do not analyze the behavior of the C-band in detail any further. We note that PL peak energies and intensities change as increasing functions of the sample temperature for all three bands. Figure 4.43 illustrates the shifts of the peaks to lower energies for the A- and the B-bands with increasing temperature. It is well known that the donor-acceptor pair transition energy decreases along with the band gap energy when the temperature is increased. As the figure shows, the decrease in the peak energy of the B-band with increasing temperature is larger than

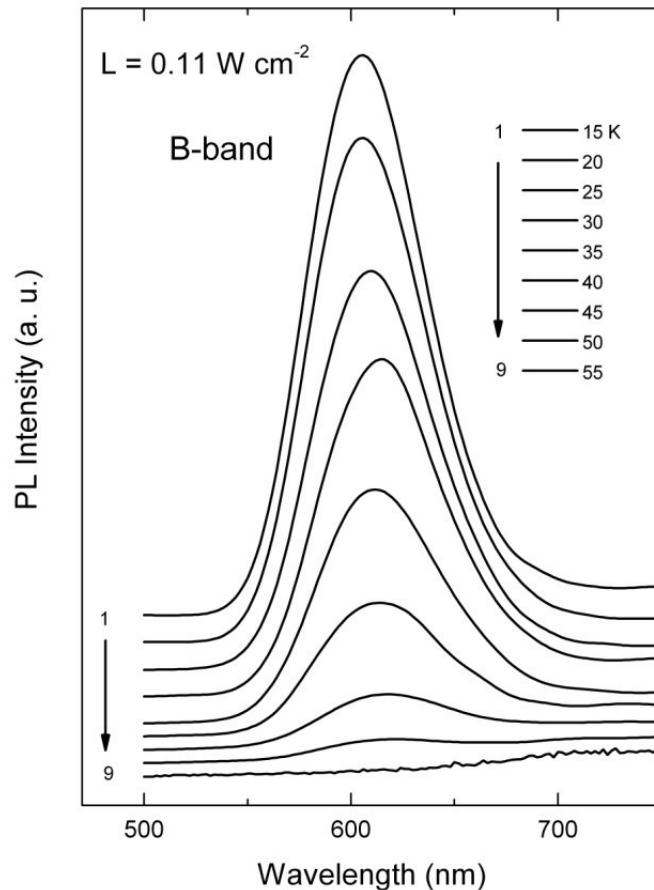


Figure 4.41. Temperature dependence of the PL spectra (B-band) from $\text{Tl}_2\text{InGaS}_4$ crystals in the 500-750 nm range. The excitation laser intensity is $L = 0.11 \text{ Wcm}^{-2}$.

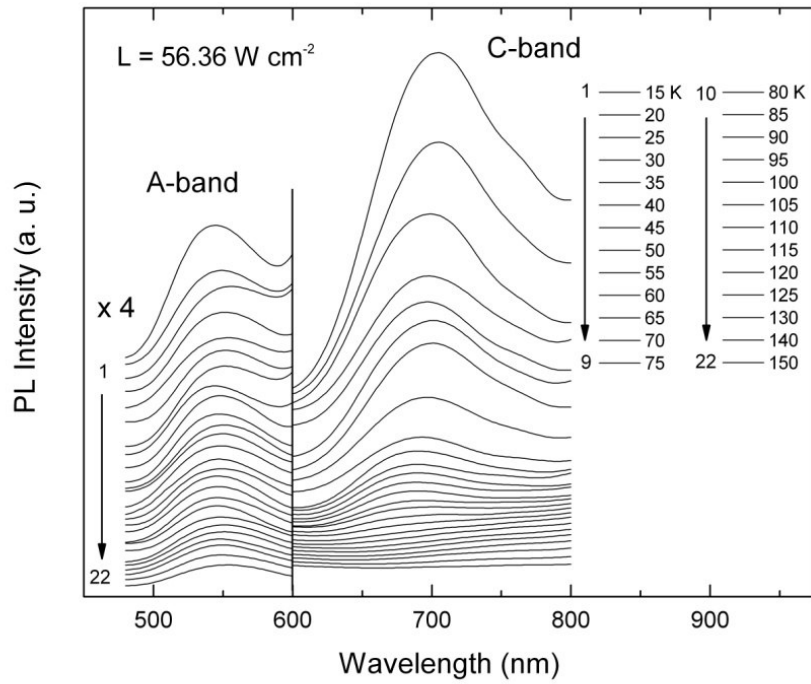


Figure 4.42. Temperature dependence of PL spectra (A- and C-bands) from $\text{Tl}_2\text{InGaS}_4$ crystals in the 475-800 nm range. The excitation laser intensity is $L = 56.36 \text{ W cm}^{-2}$.

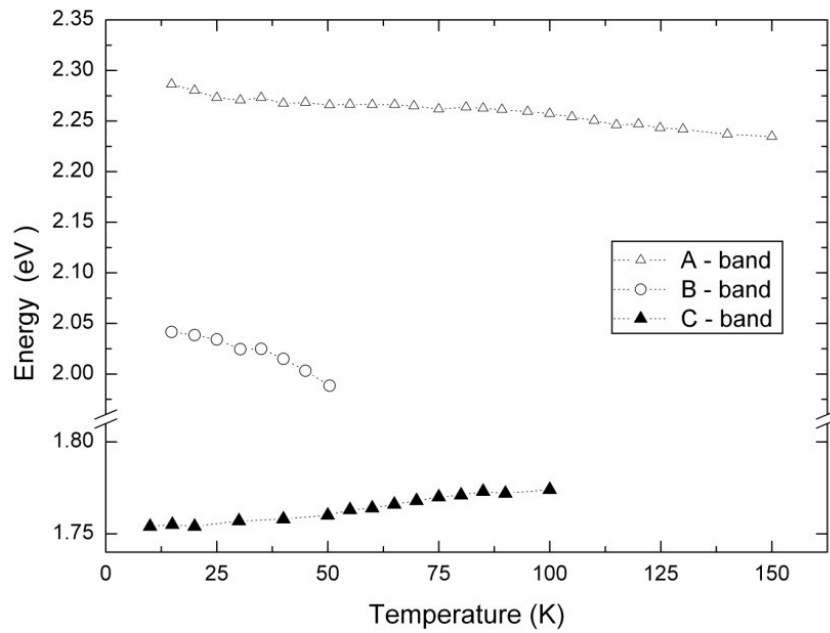


Figure 4.43. Temperature dependencies of the A- B- and the C-emission band peak energies. The dotted lines are only guides for the eyes. Experimental data for C-band (solid triangles) were taken from Ref. [96].

that of the A-band. This difference in peak energy shifts of the bands suggests that the centers responsible for the observed recombination may be similar, but not necessarily the same. Furthermore, the temperature dependence expected for the donor-acceptor pair recombination is the same as the observed red shift of both bands. Figures 4.41 and 4.42 show that the PL intensities of the B- and the A-bands decrease as the temperature of the sample is increased. The variations in the maximum intensities for both PL emission bands with temperature are plotted in figure 4.44. We notice, that the PL intensity of the A-band decreases insignificantly in the 15-55 K range, followed by thermal quenching above 55 K. The basic behavior of B-band is the same; the PL intensity decreases gradually at low temperatures, followed by thermal quenching of the PL emission for temperatures above 20 K.

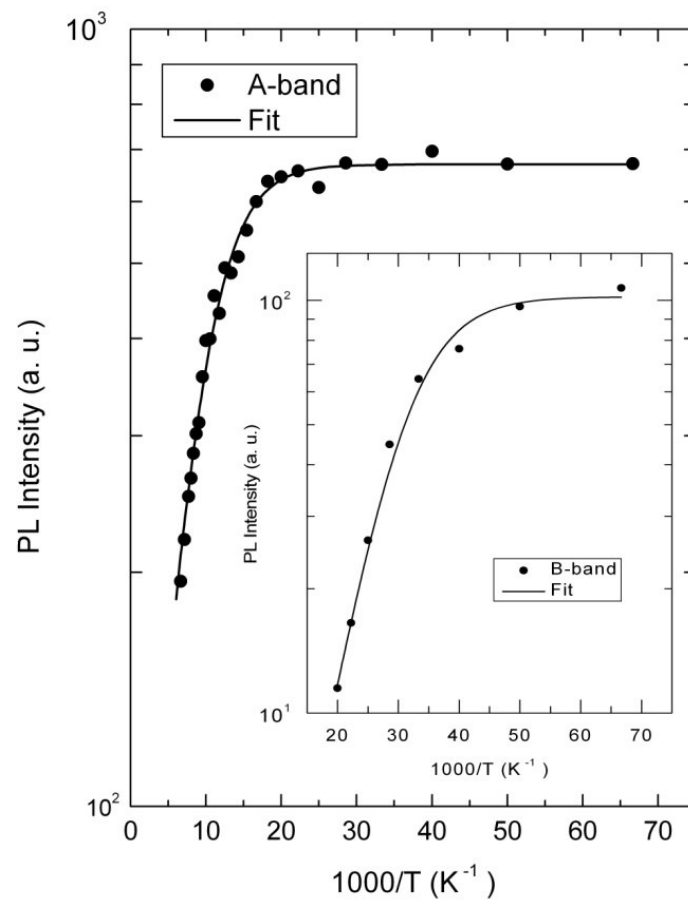


Figure 4.44. Temperature dependencies of the PL intensities at the A- and B-emission bands maxima.

The activation energies for both bands have been obtained by fitting the experimental data to the equation 2.40. After a nonlinear least squares fit, the activation energies for the A- and the B-bands are found to be 0.03 and 0.02 eV, respectively. Since $\text{Tl}_2\text{InGaS}_4$ is an n-type semiconductor, we believe that these levels are shallow donor levels located at 0.03 and 0.02 eV below the bottom of the conduction band. These shallow levels can be considered as originating from either uncontrolled impurities or from point defects. The former may be attributed to the presence of Si impurities introduced into $\text{Tl}_2\text{InGaS}_4$ during the crystal growth process in ungraphitized ampoules.

The dependence of the PL spectra on the excitation laser intensity provides invaluable insight into the nature and analysis of the luminescence spectra. For this purpose, we plot four different graphs, which allow the reader to follow the changes in the spectra with respect to the excitation laser intensity at $T = 15$ K (Figures 4.45a-4.45d). The C-band emission peak shifts slightly towards higher energies with increasing excitation laser intensity. The observed blue shift is a fundamental characteristic of donor-acceptor pair recombination [70] and is due to the spatial inhomogeneity of the donor-acceptor pairs [96]. The highest energies agree with transitions between closest pairs while the lowest energies correspond to pairs with larger separations. A detailed analysis of the peak positions of the A- and the B-bands as functions of the excitation laser intensity did not yield any variation of the peak energies. We, therefore, concentrated on the analysis of the PL intensity as a function of the excitation laser intensity. In figure 4.45a, we present the PL spectra of the $\text{Tl}_2\text{InGaS}_4$ crystal in the 0.01 - 5.15 W cm^{-2} excitation laser intensity range. In this range, we see that the PL intensities for both the B- and the C-bands increase with increasing excitation intensity. In figure 4.45b, the spectra are plotted in the 5.15 - 14.70 W cm^{-2} excitation laser intensity range. Here, we observe a decrease in the intensity of the B-band and an increase in the intensity of the C-band until finally the B-band vanishes for laser excitation intensities of $L > 10.29$ W cm^{-2} . The PL spectra in the 14.70 - 32.21 W cm^{-2} excitation laser intensity range are plotted in figure 4.45c. This graph shows that after the B-band vanishes completely, the intensity of the C-band continues to increase, reaching its maximum value at $L = 32.21$ W cm^{-2} . The last spectra, representing the PL intensity versus laser intensity, are shown in

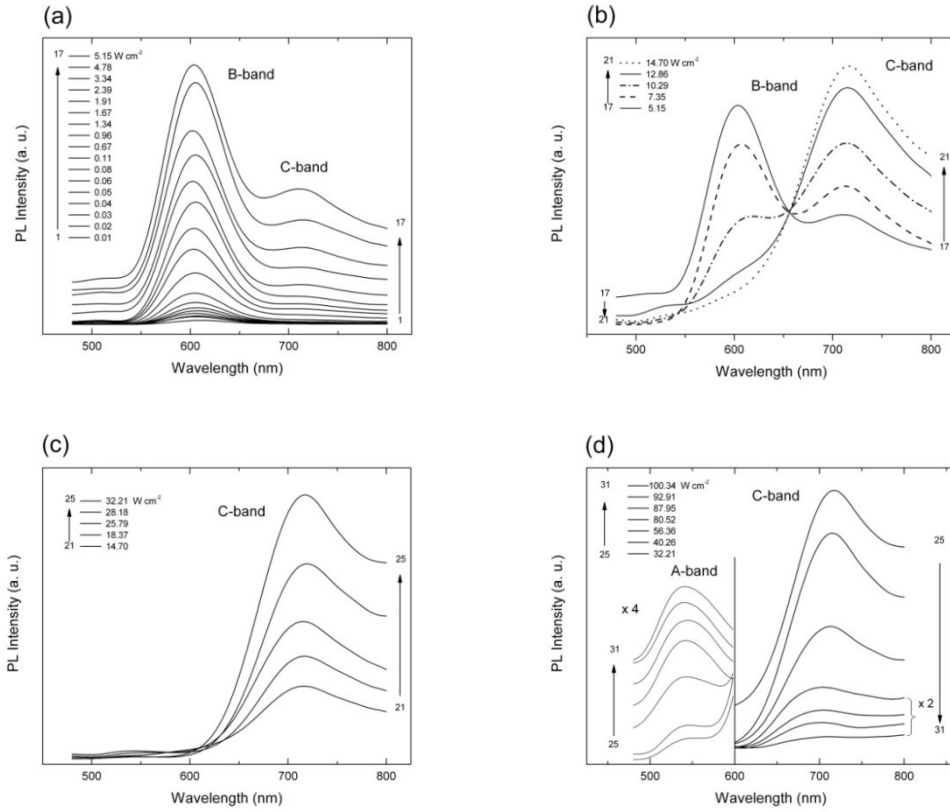


Figure 4.45. PL spectra from $\text{Tl}_2\text{InGaS}_4$ crystals at $T = 15$ K versus excitation intensity: (a) $0.01 - 5.15 \text{ Wcm}^{-2}$, (b) $5.15 - 14.70 \text{ Wcm}^{-2}$, (c) $14.70 - 32.21 \text{ Wcm}^{-2}$, and (d) $32.21 - 100.34 \text{ Wcm}^{-2}$.

figure 4.45d. In this figure, the intensities in the 475-600 nm wavelength region are multiplied by a factor of four and in the 600-800 nm wavelength region by a factor of two for clarity of the PL spectra. As figures 4.45c and 4.45d show, a new A-band arises in the spectra when the laser excitation intensity reaches the value of 18.37 Wcm^{-2} . We see that while the PL intensity of the A-band increases with increasing laser excitation intensity, the PL intensity of the C-band decreases significantly. To follow the behaviors of all the bands mentioned above more clearly, we plot, on a logarithmic scale, the PL emission band maximum intensity versus excitation laser intensity (figure 4.46). The common behavior of the three bands with respect to the excitation laser intensity is clearly demonstrated by this graph. For the analysis, the experimental data for each band in the spectra (the linear part of the curves) were fitted by the power law of the form of equation 2.33. We found that PL intensity for

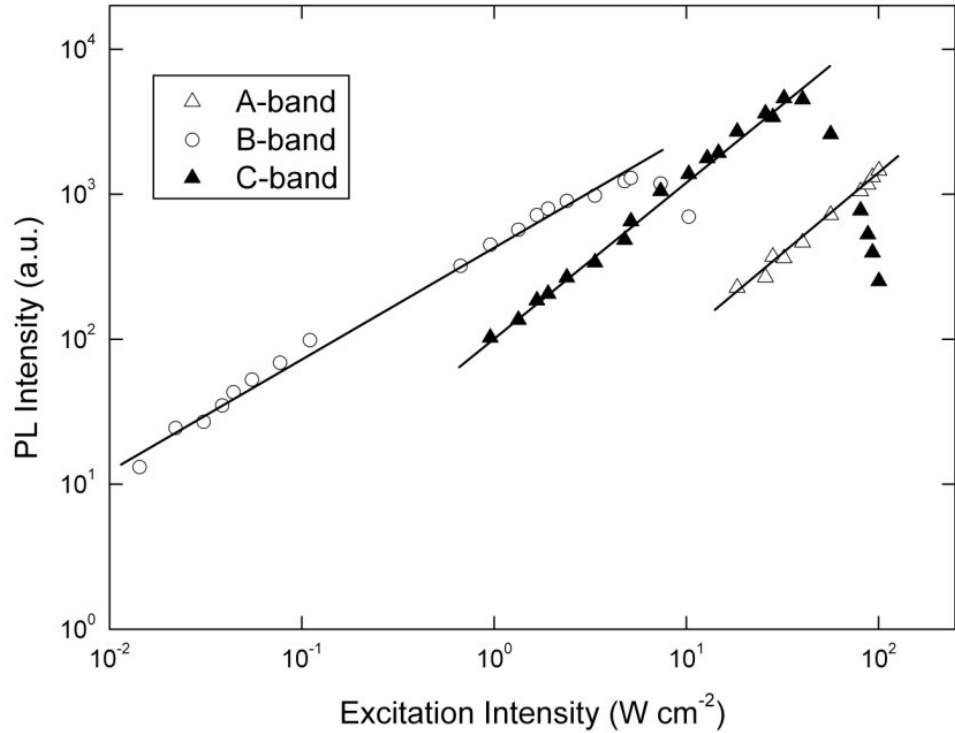


Figure 4.46. Dependencies of PL intensities at the emission band maxima versus excitation laser intensity at $T = 15$ K.

all bands increases sublinearly with increasing excitation laser intensity. By fitting the experimental data, we found γ values of 0.92, 0.78, and 0.98 for the A-, B-, and C-bands, respectively. As mentioned in chapter 2, the exponent γ is generally $1 < \gamma < 2$ for free- and bound-exciton emission, whereas $0 < \gamma \leq 1$ is typical for free-to-bound and donor-acceptor pair recombination. Thus, the obtained values of $\gamma = 0.92$, 0.78, and 0.98 confirm our assignment of the observed emission bands in the $\text{Tl}_2\text{InGaS}_4$ spectra to the donor-acceptor pair recombination. The sublinear dependence of the PL intensity on the excitation laser intensity is consistent with a donor-acceptor pair recombination process because simultaneous solution of the rate equations involving all possible radiative transitions gives a sublinear dependence for free-to-bound and donor-acceptor pair recombination [76].

Figure 4.47 shows the band and the configuration coordinate models for the A-, B-, and C-emission bands. The optical transitions causing the A- and the B-bands are summarized in this figure. Using the activation energies obtained from the temperature dependence of the PL intensity for n-type $\text{Tl}_2\text{InGaS}_4$, we place the donor

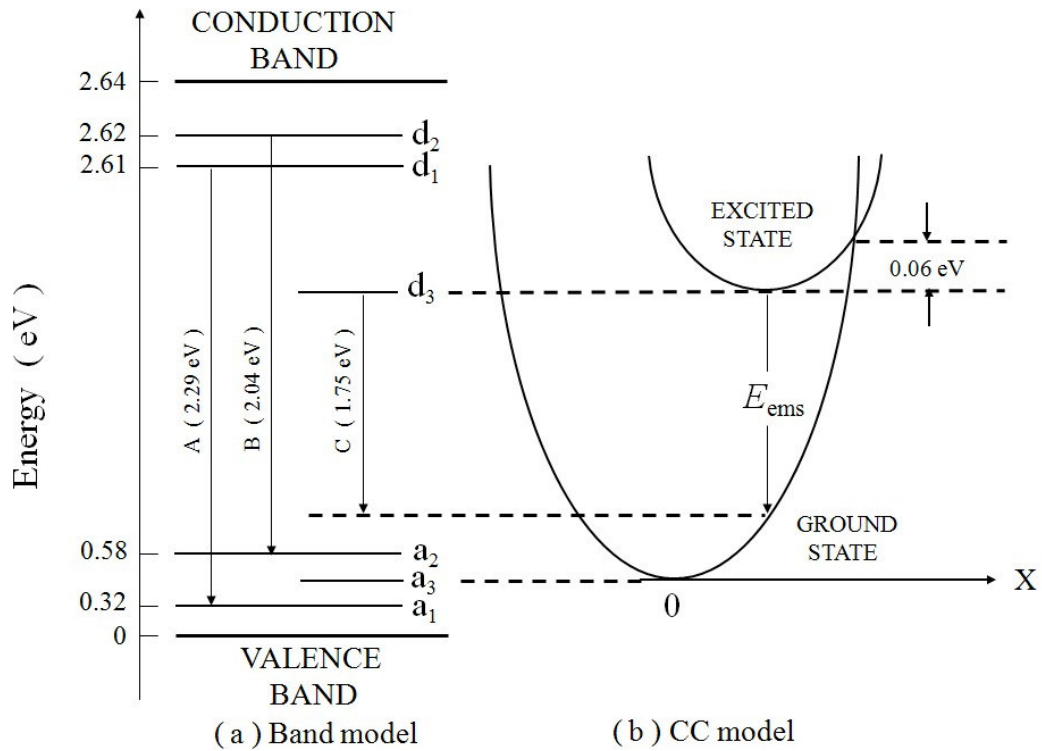


Figure 4.47. (a) Band model and (b) configurational coordinate (CC) model of a $\text{Tl}_2\text{InGaS}_4$ crystal at $T = 15$ K.

levels d_1 and d_2 at 0.03 and 0.02 eV, respectively, below the conduction band. From equation 2.31 and the peak energy values of the observed transitions (2.29 and 2.04 for A- and B-bands, respectively), the related acceptor energy levels a_1 and a_2 are then placed at 0.32 and 0.58 eV, respectively, above the valence band. Thus, the donor-acceptor pairs responsible for the A- and the B-bands are composed of moderately shallow donor and deep acceptor states.

The most striking feature of the C-band is the temperature dependence of its peak energy, which blue shifts by almost 120 meV until 150 in contrast with the A- and the B-bands displaying red shifts (figure 4.43). Such a behavior is typically understood in terms of a CC model of defects. In figure 4.47, we also present a CC model for the C-band in the PL spectra. This model assumes that the ground state of localized center is derived from an acceptor level a_3 while the excited state originates from a sulphur vacancy donor level d_3 and that the zero point of both states lies within the band gap. Since $\text{A}^{\text{III}}\text{B}^{\text{VI}}$ -type layered crystals are more polar than covalent

[101], the displacement of the excited-state minimum is expected to be reasonably large. Generally, in compound semiconductors, a deviation from stoichiometry generates donors in the case of anion vacancies. The acceptor level a_3 above the top of the valence band may be linked, as in the case of GaSe [102], to uncontrolled impurities, point defects, or stacking faults, which can easily form due to the weak interlayer interactions in the studied crystals. Electron transitions from the excited states of the donor level to the ground states of the acceptor level give rise to PL with photon energy E_{ems} .

At low excitation intensities ($L < 0.96 \text{ W cm}^{-2}$) sufficient to observe the B-band emission, the quasi-Fermi level for holes is located below only the acceptor states a_2 (figure 4.47). With increasing excitation intensity ($L > 0.67 \text{ W cm}^{-2}$), the quasi-Fermi level for holes is shifted, and the number of excited holes is large enough to fill in the acceptor level a_3 as well, which is responsible for the observed C-band emission. Therefore, in the PL spectra, we observe C-band emission along with B-band emission (figure 4.45a). If the transition probability for holes from the ground state of the acceptor level a_3 to the excited state of the donor level d_3 is greater than that for holes from acceptor level a_2 to donor level d_2 , then the dominant radiative recombination will occur from the former levels with increasing excitation intensity ($L > 7.35 \text{ Wcm}^{-2}$) (figures 4.45b and 4.45c). A further increase in the excitation intensity ($L > 32.21 \text{ Wcm}^{-2}$) leads to an increased electron population in the excited state at higher displacement coordinates (figure 4.47). These electrons then return to the ground state through nonradiative recombination. The activation energy $\Delta E = 0.06 \text{ eV}$, obtained in the previous work [96], is the difference between the energies of the lowest excited state and of the intersection point of the excited and the ground-state CC curves (figure 4.47). Thus, any further increase in the excitation intensity should not lead to an increase in the PL intensity. It is worth noting that, for $L > 32.21 \text{ Wcm}^{-2}$, we observe a decrease in the C-band intensity with increasing excitation intensity. Finally, for excitation intensities of $L > 18.37 \text{ Wcm}^{-2}$, the quasi-Fermi level for holes is shifted closer to the valence band and is located below the acceptor level a_1 . Therefore, at high excitation intensities, we observe a new A-band in the PL spectra along with the C-band due to the hole transition from the acceptor level a_1 to the donor level d_1 (figure 4.45d). This suggests that the transition probability for holes from the acceptor level a_1 to the donor level d_1 is higher than that for holes from the ground state of the acceptor level a_3 to the excited

state of the donor level d_3 . This fact may account for the dominant radiative recombination from the acceptor level a_1 to the donor level d_1 rather than that from the acceptor level a_3 to the donor level d_3 at $L > 56.36 \text{ Wcm}^{-2}$ (figure 4.45d).

4.6 Results of the Structural and Optical Characterization Experiments for $\text{Tl}_4\text{InGa}_3\text{S}_8$ crystal

The quaternary $\text{Tl}_4\text{InGa}_3\text{S}_8$ crystal belongs to the group of layered semiconductors. This compound is a structural analog of TlGaS_2 , with a difference that a quarter of gallium ions are replaced by indium ions [5, 92]. The lattice of $\text{Tl}_4\text{InGa}_3\text{S}_8$ consists of rigorously periodic two-dimensional layers arranged parallel to the (001) plane (figure 4.10). Each consecutive layer is rotated by a right angle with respect to the previous one. The bonding between Tl and S atoms is of an interlayer type whereas the bonding between (In)Ga and S is of an intralayer type. The fundamental structural unit of a layer is the $\text{Ga}_4(\text{In}_4)\text{S}_6$ adamantane-like units linked together by bridging S atoms.

The electrical conductivity of the studied sample was determined to be n-type by the hot probe method. Crystals suitable for PL measurements had typical sample dimensions of $6 \times 4 \times 1 \text{ mm}^3$. After cleaving, the resulting ingot appears green in color and the freshly cleaved surfaces were mirror-like.

4.6.1 Results of X-Ray Experiments

The structure of $\text{Tl}_4\text{InGa}_3\text{S}_8$ crystals was defined by the X-ray powder diffraction experiments. X-ray diffractograms of $\text{Tl}_4\text{InGa}_3\text{S}_8$ were indexed as seen in figure 4.48. As a result of the analysis, the obtained Miller indices (hkl), the observed and calculated interplanar spacings (d) and the relative intensities (I/I_0) of the diffraction lines are listed in table 4.5.

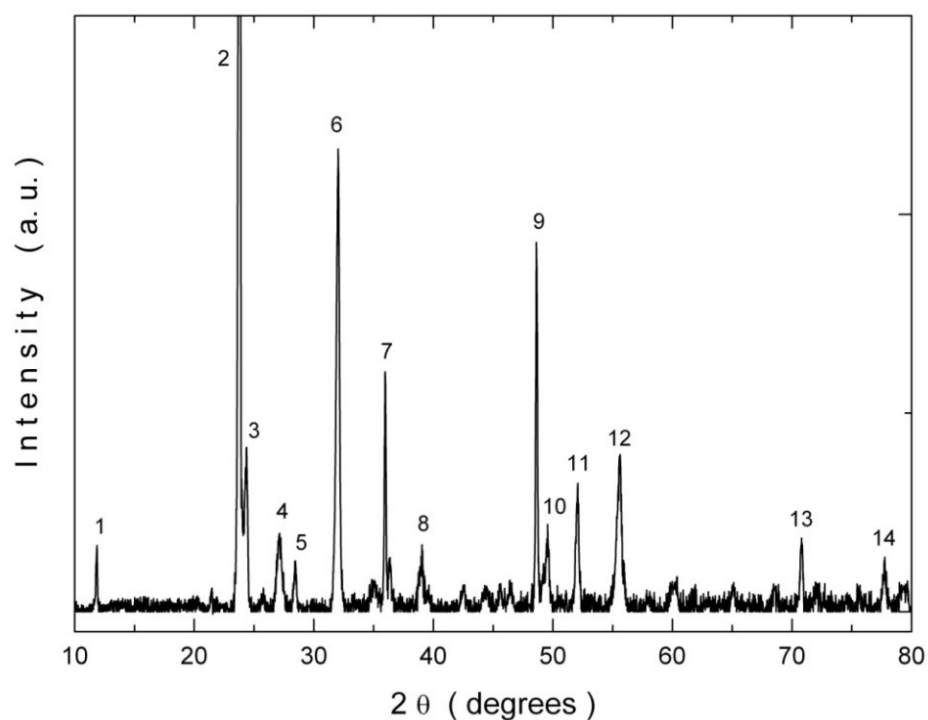


Figure 4.48. X-ray diffraction pattern of $\text{Tl}_4\text{InGa}_3\text{S}_8$ powder sample.

Table 4.5. X-ray powder diffraction data for $\text{Tl}_4\text{InGa}_3\text{S}_8$ crystals.

No.	<i>h</i>	<i>k</i>	<i>l</i>	d_{obs} (nm)	d_{calc} (nm)	I/I_0
1	1	0	-1	0.7456	0.7460	3
2	2	0	-2	0.3739	0.3737	100
3	1	1	-1	0.3648	0.3651	6
4	2	1	-1	0.3285	0.3284	3
5	1	1	1	0.3134	0.3133	2
6	2	1	-2	0.2789	0.2789	15
7	3	0	-3	0.2494	0.2493	8
8	0	0	3	0.2304	0.2305	3
9	4	0	-4	0.1870	0.1871	12
10	1	2	-2	0.1841	0.1841	3
11	2	1	-4	0.1753	0.1753	4
12	2	1	3	0.1650	0.1650	6
13	7	1	0	0.1330	0.1330	3
14	8	0	0	0.1227	0.1227	2

The calculated (using equation 2.12) and observed interplanar spacings were found to be in good agreement with each other. The lattice parameters of the monoclinic unit cell were found to be $a = 0.7777$, $b = 0.4192$, $c = 1.0198$ nm, and $\beta = 105.63^\circ$.

4.6.2 Results of EDSA Experiments

The determination of the chemical composition of $\text{Tl}_4\text{InGa}_3\text{S}_8$ crystals was done by EDSA experiments. The result of the EDSA experiment in 0-10 keV energy range is shown in figure 4.49. The composition of the studied samples (Tl:In:Ga:S) was estimated as 26.1:6.1:19.0:48.8, respectively. Furthermore, EDSA indicated that silicon impurities were present in the crystal.

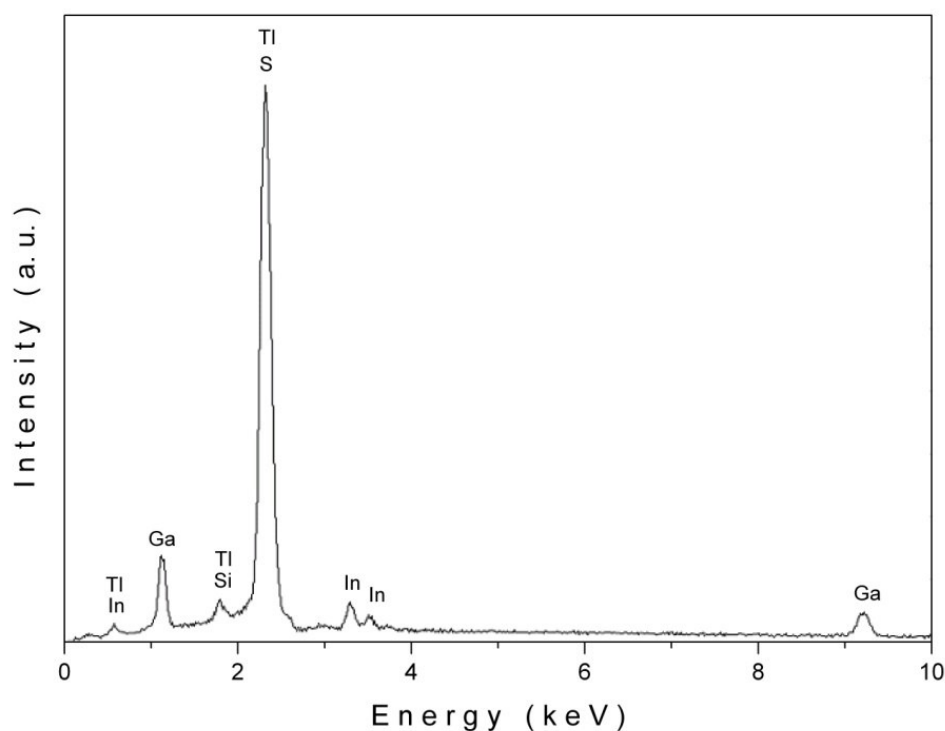


Figure 4.49. Energy dispersive spectroscopic analysis of $\text{Tl}_4\text{InGa}_3\text{S}_8$ crystal.

4.6.3 Results of Transmission and Reflection Experiments

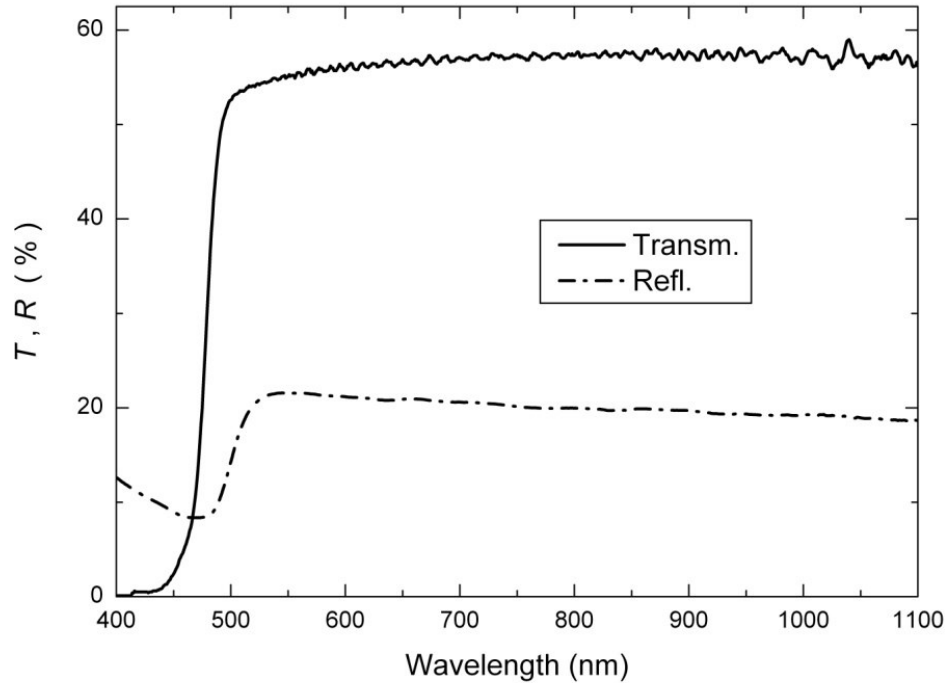


Figure 4.50. The spectral dependence of transmittance and reflectivity for $\text{TL}_4\text{InGa}_3\text{S}_8$ crystal at $T = 300$ K.

Figure 4.50 presents the results of the transmission and reflection experiments for $\text{TL}_4\text{InGa}_3\text{S}_8$ single crystals in 450-1100 nm wavelength range. As mentioned in chapter 2, the reflectivity and transmittance of the material is governed by the equations 2.16 and 2.18, respectively. The determination of n , k and α can be done from the reflectivity and transmittance measurements by the help of these relations. The reflectivity is measured using samples with natural cleavage planes and a thickness such that $\alpha x \gg 1$. The sample is then reduced in thickness (by repeated cleaving using transparent adhesive tape) until it is convenient for transmission measurements. The thickness was determined using transmission interference fringes at the wavelengths slightly longer than the intrinsic absorption edge, i.e., in a region with relatively high transmission (figure 4.50) by the help of equation 2.21. For this purpose, the long wavelength value of the refractive index $n = 2.52$, obtained from

the reflection measurements was used. In most cases the sample thickness was about $10\ \mu\text{m}$ for room temperature transmission measurements.

The dependence of absorption coefficient on photon energy is analyzed in the high absorption regions to obtain the detailed information about the energy band

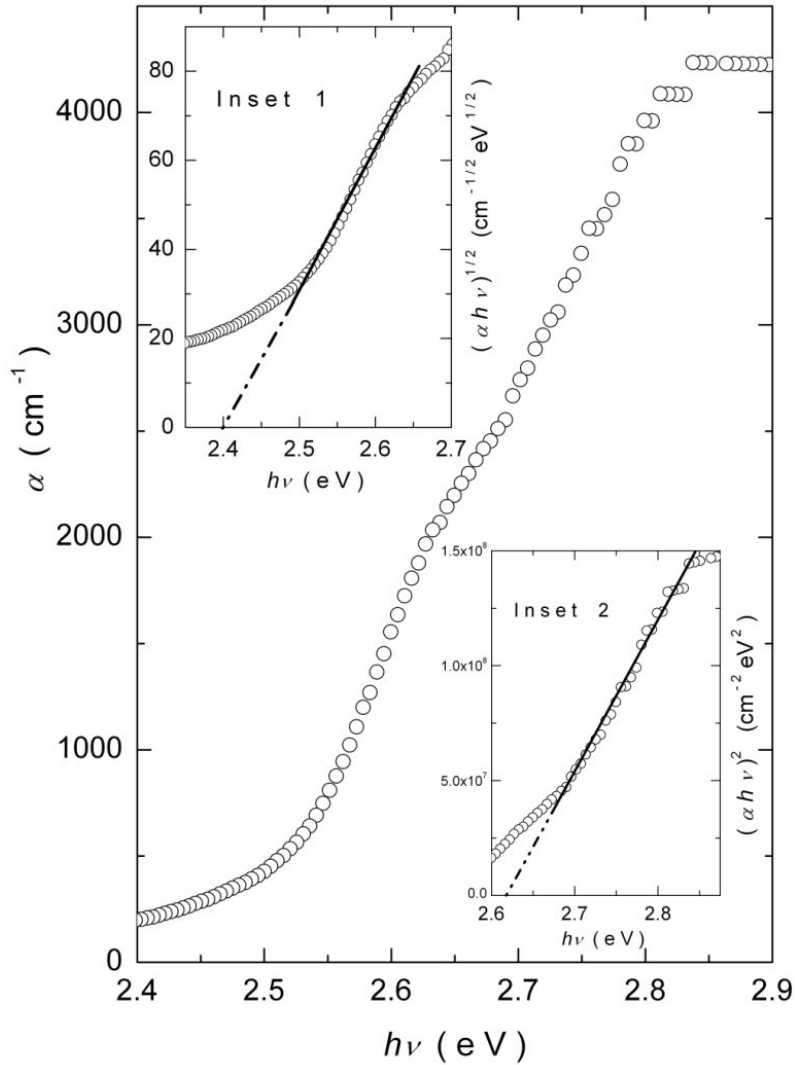


Figure 4.51. The variation of absorption coefficient as a function of photon energy at $T = 300\ \text{K}$. Insets 1 and 2 represent the dependences of $(\alpha h\nu)^{1/2}$ and $(\alpha h\nu)^2$ on photon energy, respectively.

gaps. As mentioned in chapter 2, the relation between the absorption coefficient α and photon energy can be expressed by equation 2.15. Figure 4.51 shows the

calculated room temperature absorption coefficient α for $\text{Tl}_4\text{InGa}_3\text{S}_8$ crystal in the photon energy range 2.40-2.85 eV. It was revealed that α changes from 200 to 4230 cm^{-1} with increasing photon energy from 2.40 to 2.85 eV. Analysis of the experimental data shows that the absorption coefficient is proportional to $(h\nu - E_g)^p$ with $p = 2$ and $1/2$ for ranges 2.50-2.65 eV and 2.68-2.85 eV, respectively. Insets 1 and 2 of figure 4.51 display the dependences of the dependencies of $(\alpha h\nu)^{1/2}$ and $(\alpha h\nu)^2$ on photon energy $h\nu$, respectively. The circles are the experimental data that were fitted to a linear equation (the solid lines) for finding the band gaps. The linear dependencies for the relations $(\alpha h\nu)^{1/2}$ and $(\alpha h\nu)^2$ versus $h\nu$ suggests the realization of indirect and direct allowed transitions for $\text{Tl}_4\text{InGa}_3\text{S}_8$ crystal over the ranges 2.50-2.65eV and 2.68-2.85 eV, respectively. The extrapolations of the straight lines down to $(\alpha h\nu)^{1/2} = 0$ and $(\alpha h\nu)^2 = 0$ give the values of indirect and direct band gap energies $E_{gi} = 2.40 \pm 0.02 \text{ eV}$ and $E_{gd} = 2.61 \pm 0.02 \text{ eV}$, respectively.

The transmission spectra for $\text{Tl}_4\text{In}_3\text{GaS}_8$ crystal registered in the temperature range of 10-300 K is shown in Figure 4.52. Since the thin layered samples were very fragile, they broke into pieces at low temperatures. Therefore, the low-temperature measurements were carried out on thick samples (about $350 \mu\text{m}$). For this reason, we were able to analyze the temperature dependence of indirect energy band gap (E_{gi}) only. Technical reasons did not allow a direct measurement of the reflection at low temperatures. Hence, for the calculation of absorption coefficient α , the spectral dependence of room temperature reflectivity was uniformly shifted in energy according to the blue shift of the absorption edge.

The obtained value of indirect transition energy gap decreases from 2.51 to 2.41 eV with increasing temperature from 10 to 300 K, as illustrated in the inset of figure 4.52. As mentioned before, the data of the $E_{gi} - T$ dependence (inset of figure 4.52) were fitted using equation 2.10. The fitting is represented by the solid line that revealed the fitting parameters as $E_{gi}(0) = 2.52 \text{ eV}$, $\gamma = -6.0 \times 10^{-4} \text{ eV/K}$ and $\beta = 180 \text{ K}$. As a result of calculations with Lindemann's melting rule [93], the Debye temperature for $\text{Tl}_4\text{InGa}_3\text{S}_8$ crystal was estimated to be $\beta = 183 \text{ K}$.

The refractive index n calculated using equations 2.14, 2.16 and 2.18 as a function of wavelength is shown in figure 4.53. The figure shows that The refractive index in the energy region of $h\nu < E_g$ gradually decreases from 2.73 to 2.52 with

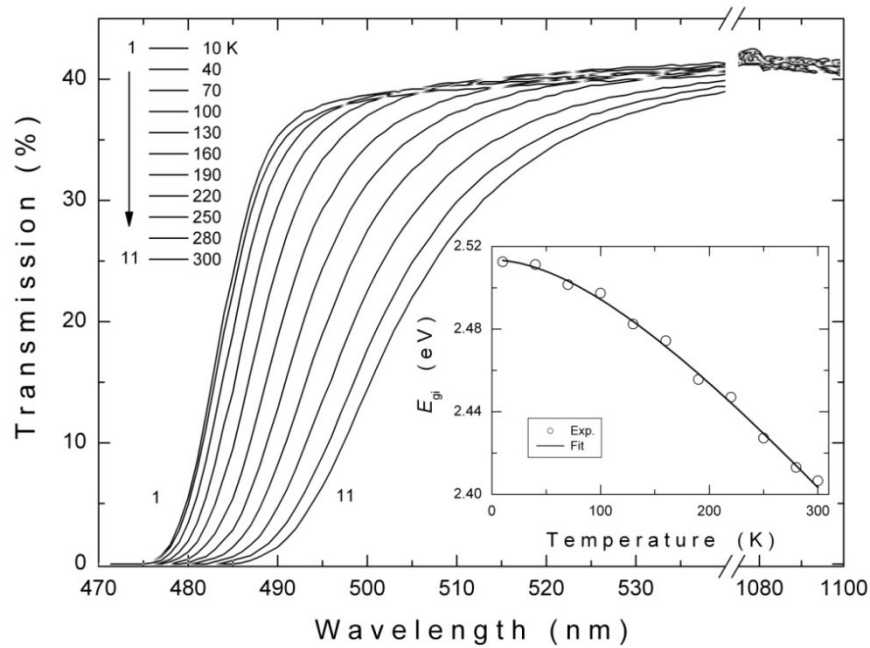


Figure 4.52. The spectral dependence of transmittance for $\text{Tl}_4\text{InGa}_3\text{S}_8$ crystal in the temperature range of 10-300 K. Inset: the indirect band gap energy as a function of temperature. The solid line represents the fit using equation 2.10.

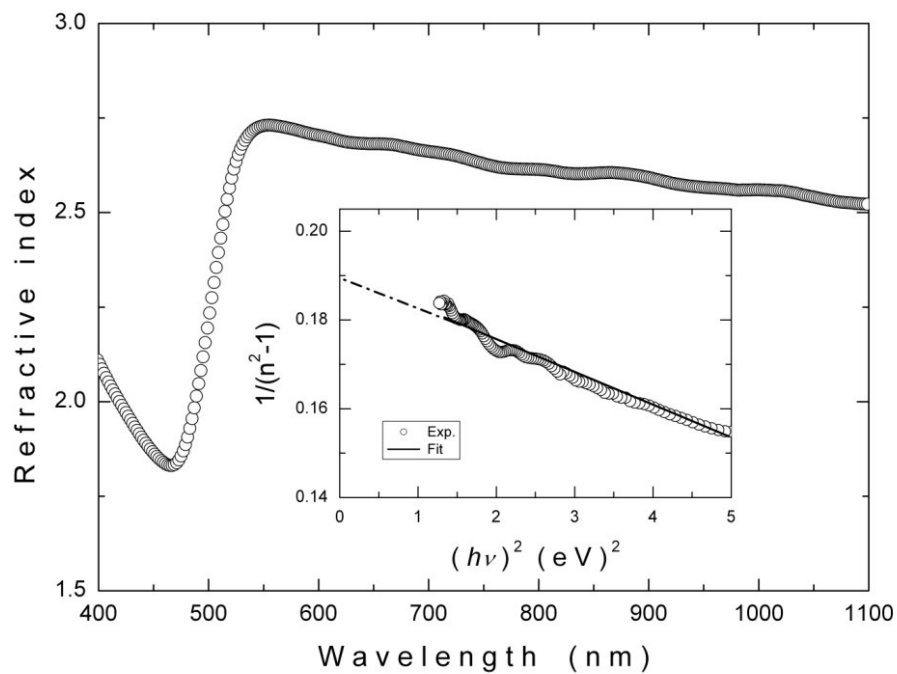


Figure 4.53. The dependence of refractive index on the wavelength for $\text{Tl}_4\text{InGa}_3\text{S}_8$ crystal. Inset: Plot of $(n^2-1)^{-1}$ versus $(h\nu)^2$. The solid line represents the fit using equation 2.22.

increasing wavelength in the range 555-1100 nm. The long wavelength value of refractive index is consistent with the values 2.7 ($\lambda = 800$ nm), 2.6 ($\lambda = 1100$ nm), and 2.6 ($\lambda = 1100$ nm) reported for TlInS₂ [99], TlGaS₂ [67] and Tl₂InGaS₄ [100] single crystals, respectively.

The dispersive refractive index data in $h\nu < E_g$ range were analyzed according to the single-effective-oscillator model proposed by Wemple and DiDomenico [60, 61]. As mentioned in chapter 2, the refractive index is related to photon energy through the equation 2.22, according to which plotting $(n^2-1)^{-1}$ versus $(h\nu)^2$ allows the determination of the oscillator parameters by fitting a linear function to the lower energy data range (1.15-2.24 eV). The fitting of the above reported function is presented in inset of figure 4.53. The zero-frequency refractive index n_0 is estimated according to the equation 2.23. The values of the parameters E_{so} and E_d were calculated from the slope and the intersection with y -axis of the straight line (inset of figure 4.53) as 5.07 eV and 26.67 eV, respectively. In addition, the values of zero-frequency dielectric constant $\varepsilon_0 = n_0^2 = 6.26$ and refractive index $n_0 = 2.50$ were calculated by means of equation 2.22. As mentioned before, the oscillator energy E_{so} is related empirically with the lowest direct band gap E_{gd} by the relationship $E_{so} \cong 2.0 E_{gd}$. The ratio E_{so}/E_{gd} for Tl₄InGa₃S₈ crystal, determined in this study, was calculated as 1.94.

The refractive index n can be analyzed to determine the oscillator strength S_{so} for Tl₄InGa₃S₈ crystal. The refractive index can be represented by a single Sellmeier oscillator at low energies by equation 2.25. The values of S_{so} and λ_{so} were calculated from $(n^2-1)^{-1}$ versus λ^{-2} plot to be $8.82 \times 10^{13} \text{ m}^{-2}$ (135.67 eV^2) and $2.44 \times 10^{-7} \text{ m}$, respectively. As before, it is recognized that the obtained value of oscillator strength is of the same order as those obtained for ZnS, ZnSe, Ag₂S, GeSe₂ and TlGaS₂ crystals [61, 65, 67, 94].

4.6.4 Results of Photoluminescence Experiments

Temperature-dependent PL measurements in Tl₄InGa₃S₈ crystal were carried out by using two different excitation sources. Since our sample has a direct band gap of $E_{gd} = 2.71$ eV at $T = 30$ K, the source (He-Cd laser) with $\lambda_{exc} = 325$ nm (3.82 eV) is referred to as the above bandgap excitation source and the other one (YAG:Nd³⁺

laser) with $\lambda_{\text{exc}} = 532 \text{ nm}$ (2.33 eV) is referred to as the below band gap excitation source, for this study. Figure 4.54 shows PL spectra of a $\text{Tl}_4\text{InGa}_3\text{S}_8$ crystal corresponding to the above band gap excitation process in the 420-600 nm wavelength region and the 30-300 K temperature range at a constant excitation laser intensity of $2476.4 \text{ mW cm}^{-2}$. Figure 4.55 demonstrates PL spectra of the sample corresponding to the below band gap excitation process in the 550-710 nm wavelength region and 80-300 K temperature range at a constant excitation laser intensity of 429.7 mW cm^{-2} . In figure 4.54, a broad emission band having a full-width at half maximum (FWHM) of 0.53 eV at $T = 30 \text{ K}$ centered at 496 nm (2.49 eV, A-band) was observed, while in figure 4.55 another broad emission band with FWHM of 0.25 eV at $T = 80 \text{ K}$ centered at 580 nm (2.14 eV, B-band) was revealed. These large FWHM values of A- and B-bands are typical properties of emissions originating from donor-acceptor pair transitions [104]. From figures 4.54 and 4.55, it is also clear that both band peak energies show a red shift of different degrees. The change in the peak energy of the A-band with increasing temperature from 30 to 300 K is about 80 meV, whereas that of the B-band in the temperature interval of 80-300 K is about 6 meV.

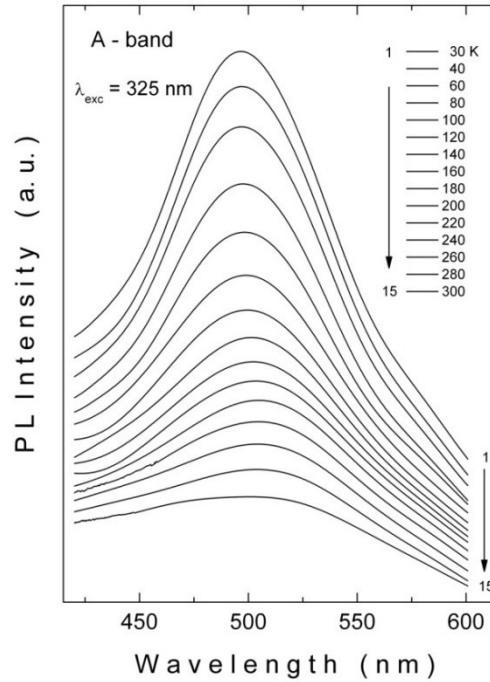


Figure 4.54. Temperature dependence of PL spectra of $\text{Tl}_4\text{InGa}_3\text{S}_8$ crystal for above bandgap excitation with $\lambda_{\text{exc}} = 325 \text{ nm}$ at an excitation laser intensity of $L = 2476.4 \text{ mW cm}^{-2}$.

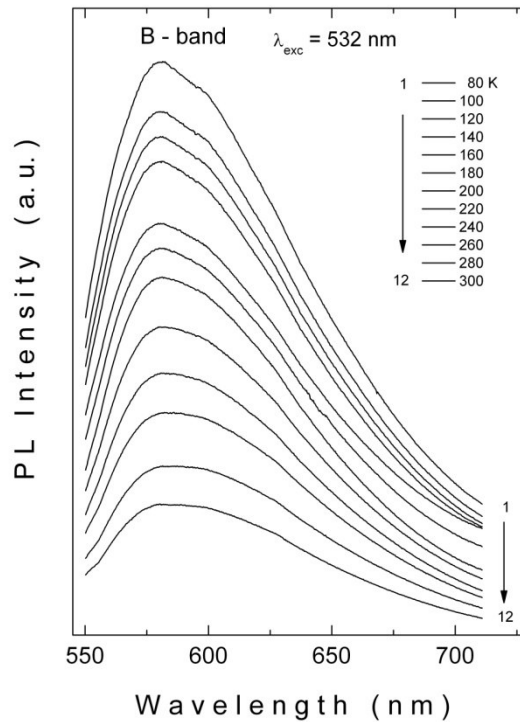


Figure 4.55. Temperature dependence of PL spectra of $\text{Tl}_4\text{InGa}_3\text{S}_8$ crystal for below bandgap excitation with $\lambda_{\text{exc}} = 532 \text{ nm}$ at an excitation laser intensity of $L = 429.7 \text{ mW cm}^{-2}$.

The temperature dependence of the peak intensity of the PL spectra can be used to obtain valuable information about the electronic energy levels in the forbidden energy gap. From figures 4.54 and 4.55, it is seen that the peak intensities of both A- and B-bands change as a function of sample temperature. To analyze the intensity behavior of both bands, the Arrhenius plots of peak intensity dependence on temperature are plotted in figure 4.56. From the figure it is clear that as the temperature is increased both bands significantly decrease in intensity. It is well-known that the decrease in intensity can be explained by the activation of nonradiative processes in the crystal structure. From the figure, it is also seen that neither band has completely vanished at 300 K, therefore, before doing any calculations, we supposed that the activation energies for both bands should have been large enough to completely overcome quenching at room temperature, which can also be interpreted to show that we are dealing with deep defect levels. The

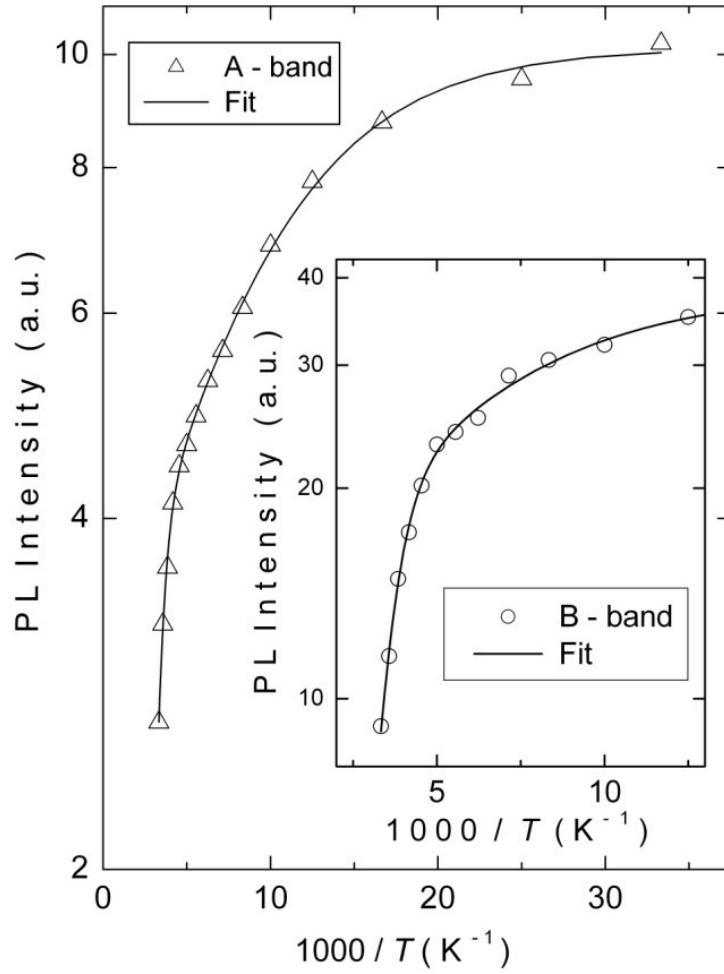


Figure 4.56. Temperature dependences of PL intensities at emission band maxima for A- and B-bands.

thermal quenching behavior of PL peak intensity can be defined best by the equation 2.42 with two activation energies as

$$I = \frac{I_0}{1 + \alpha_1 \exp\left(-\frac{E_{t1}}{k_B T}\right) + \alpha_2 \exp\left(-\frac{E_{t2}}{k_B T}\right)}. \quad (2.42)$$

The activation energies for both bands have been obtained by fitting experimental data to the equation 2.42. The results of the fits are shown in figure 4.56. After a successful fitting process, it was found that the A-band quenches with two activation energies as $E_{1A} = 0.02$ eV at low temperatures and $E_{2A} = 0.20$ eV at higher temperatures, while the B-band also quenches with two activation energies as $E_{1B} =$

0.03 eV at low temperatures and $E_{2B} = 0.20$ eV at higher temperatures. From the results, it is clear that the activation energies E_{2A} and E_{2B} belong to the same energy level, therefore, we can say that the origin of both emission processes is the same energy level having an activation energy of 0.20 eV, which also confirms our previous remark that a deep defect level plays a role in both emissions processes.

Recalling equation 2.7, a simple calculation for A-band emission by using the values of $E_g = 2.71$ eV, $h\nu_A = 2.49$ eV and $E_a(E_{2A}) = 0.20$ eV gives us the energy of the donor level $E_d(E_{1A})$ as 0.02 eV. Moreover, since $\text{Tl}_4\text{InGa}_3\text{S}_8$ crystal has n-type conductivity, it is very reasonable to believe that the A-band low-temperature activation energy E_{1A} relates to the shallow donor level d_1 located below the conduction band at 0.02 eV, which also confirms our previous calculation result. On the other hand, we notice that the B-band low temperature activation energy E_{1B} does not simply belong to a shallow donor level. The reason for this proposition is that the thermal quenching process of the B-band cannot be described by the existence of a 0.03 eV shallow donor level, since equation 2.7 is not satisfied with obtained values of $E_g = 2.71$ eV, $h\nu_B = 2.14$ eV, $E_d(E_{1B}) = 0.03$ eV and $E_a(E_{2B}) = 0.20$ eV. Therefore, we suppose the presence of two deep donor levels d_2 and d_3 with energies 0.34 and 0.37 eV, respectively, in the band gap (figure 4.58). In this case, the activation energy $E_{1B} = 0.03$ eV actually corresponds to the thermal release of electrons from the deep donor state d_3 to the relatively shallow state d_2 . A similar proposal for two close deep acceptor levels in CdTe crystal has been made by Cotal *et al.* [105], where the low-temperature activation energy (0.02 eV) was directly related to the thermal quenching process between these deep acceptor levels.

Excitation laser intensity dependence of the PL spectra is an important consideration when studying the nature of deep level luminescence from semiconductors. For this reason, to study excitation laser intensity-dependent variations of the B-band, the PL measurements were done at $T = 80$ K in the 10.3-429.7 mW cm^{-2} excitation laser intensity range and the 540-710 nm wavelength region with only below band gap excitation using a YAG:Nd³⁺ laser. The excitation laser intensity dependence of the A-band with above band gap excitation could not be studied due to a lack of neutral density filters that can be used at $\lambda_{\text{exc}} = 325$ nm. The results of the experiments for different excitation laser intensities are shown in figure 4.57. From the figure, it is easily noticeable that the B-band peak intensity changes as a function of excitation laser intensity, whereas its energy does not show

any significant change at all. This kind of behavior can be explained by a closely spaced donor-acceptor pair model, which proposes that the donor-acceptor pairs responsible for the emission are located at only closely spaced sites and are distributed homogeneously, in contrast with inhomogeneously distributed donor-acceptor pairs where increasing laser intensity excites more pairs that are closely spaced leading to a blue shift of the peak energy of the observed band [70]. We believe that these pairs are associated with some uncontrollable defects in the crystal structure due to stacking faults or unintentional impurities. Further analyses were carried out by fitting the experimental data to a power law of the form of equation 2.33. It was revealed that the intensity of the B-band increases sublinearly with increasing excitation laser intensity. The value of γ was found to be 0.96 by a linear fit, as shown in the inset to figure 4.57. As mentioned in chapter 2, the exponent γ is generally $1 < \gamma < 2$ for free- and bound-exciton emission, whereas $0 < \gamma \leq 1$ is typical for free-to-bound and donor-acceptor pair recombination. Thus, the obtained value of $\gamma < 1$ further confirms our assertion that the B-band originates from a donor-acceptor pair recombination.

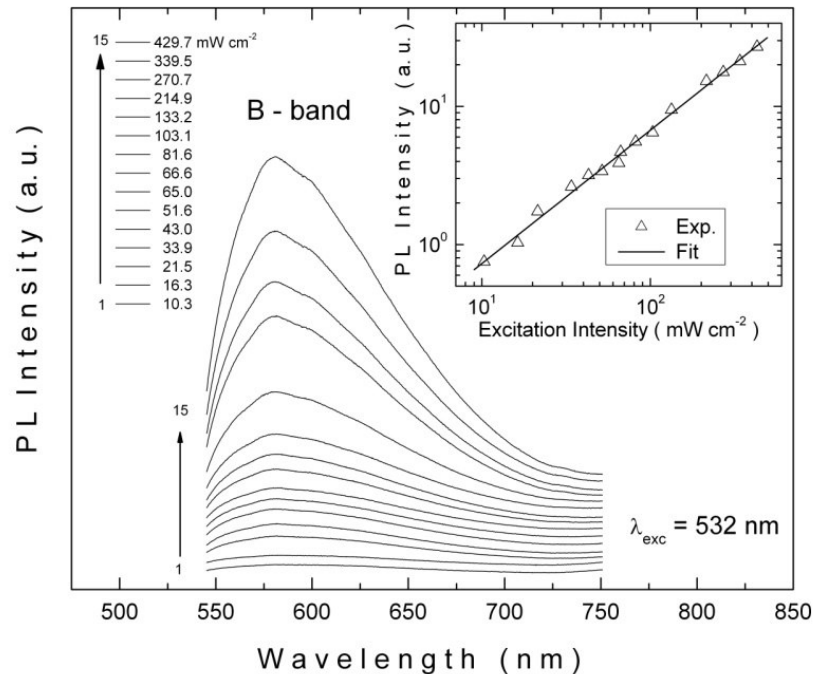


Figure 4.57. Excitation laser intensity dependence of PL spectra of Tl₄InGa₃S₈ crystal for below bandgap excitation with $\lambda_{\text{exc}} = 532$ nm at $T = 80$ K. Inset: dependence of B-band PL intensity at the emission band maxima on the excitation laser intensity ($\lambda_{\text{exc}} = 532$ nm).

As a result of the analysis, we propose a band structure model for $\text{Tl}_4\text{InGa}_3\text{S}_8$ crystal, presented in figure 4.58. In this model, one shallow donor level d_1 and two deep donor levels d_2 and d_3 are located at 0.02 eV, 0.34 eV and 0.37 eV, respectively, below the conduction band. In addition to these donor levels, we also suppose that a deep acceptor level a is located at 0.20 eV above the valence band. Taking into account the high resistivity of our crystal, we believe that the concentration of acceptors is high enough to efficiently compensate the donors. At this point, it is inevitable that the below band gap excitation with photons from the YAG:Nd³⁺ laser having a wavelength of $\lambda_{\text{exc}} = 532 \text{ nm}$ (2.33 eV) does not have enough energy to overcome the band gap energy, so such an excitation can only

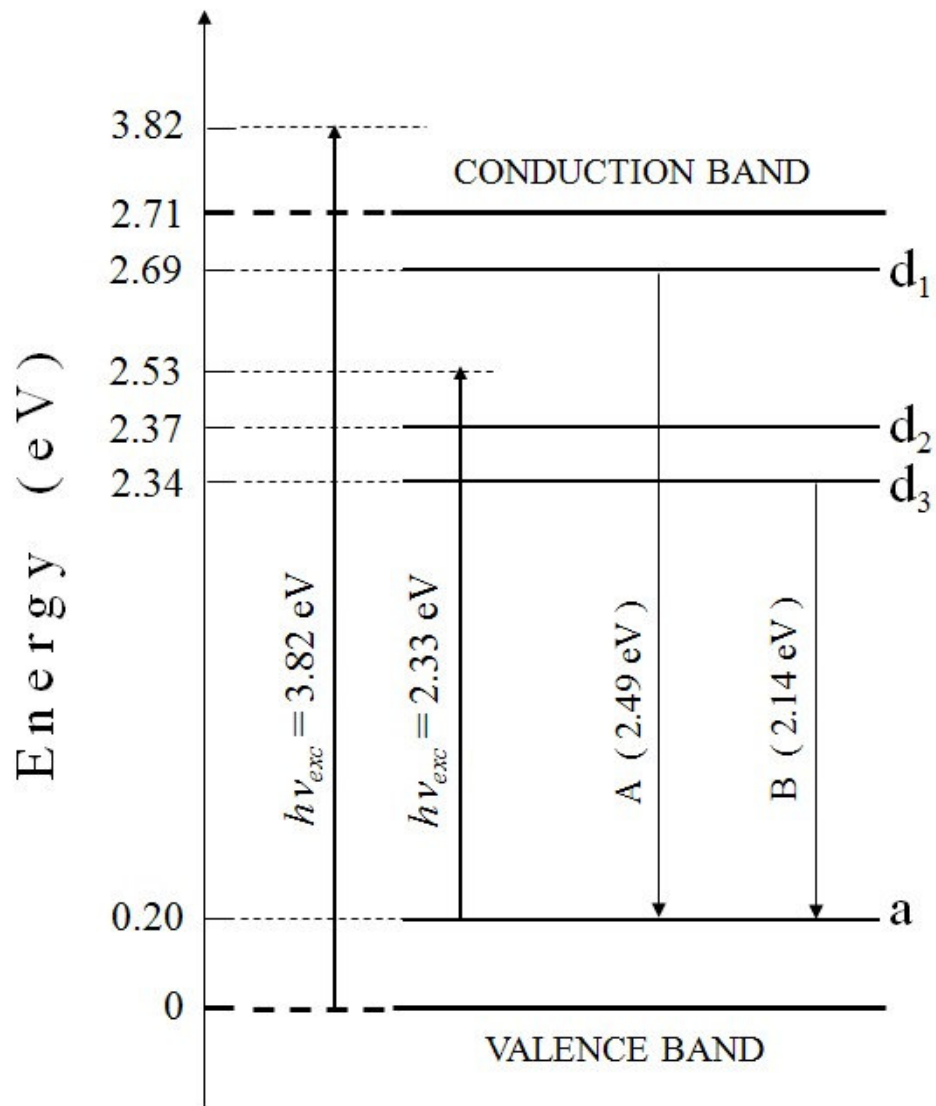


Figure 4.58. Proposed band model for $\text{Tl}_4\text{InGa}_3\text{S}_8$ crystal.

cause the electrons to be excited from the acceptor level a to levels above the deep donor levels. Then the excited electrons make a transition from the donor level d_3 to the acceptor level a , giving rise to B-band emission. When we switch to above band gap excitation with photons from the He-Cd laser having a wavelength of $\lambda_{\text{exc}} = 325$ nm (3.82 eV), it is seen that the photon energy is high enough to overcome the band gap energy this time. So, the electrons can easily be excited to the conduction band. If the transition probability between the shallow donor level and the deep acceptor level is greater than that of the deep donor level and deep acceptor level, the dominant radiative recombination will occur from the shallow donor level to the deep acceptor level. Therefore, transitions from the donor level d_1 to the acceptor level a result in A-band emission. In such a condition, B-band emission is not observed in the spectra due to its relatively low probability, as expected.

CHAPTER 5

CONCLUSION

On account of the fact that the layered- and chain-structured $\text{TlIn}_x\text{Ga}_{1-x}\text{Se}_2$ and $\text{TlIn}_x\text{Ga}_{1-x}\text{S}_2$ chalcogenide systems attract much interest for their possible applications in optoelectronic devices, the focus of the dissertation research was the study of optical properties of relatively unexplored system members, namely $\text{Tl}_4\text{In}_3\text{GaSe}_8$, $\text{Tl}_4\text{InGa}_3\text{Se}_8$, $\text{Tl}_4\text{In}_3\text{GaS}_8$, $\text{Tl}_2\text{InGaS}_4$ and $\text{Tl}_4\text{InGa}_3\text{S}_8$. In line with the reality that the optoelectronic properties of these materials are dominated by defects of various types and the interactions between them, it became essential to have detailed information on the defect levels for the fabrication of high-quality devices. Therefore, in the present study, photoluminescence (PL) and transmission-reflection experiments were employed to study the defect and band edge states, respectively. In addition, the completion of a comprehensive characterization was achieved by use of X-ray and energy dispersive spectral analysis (EDSA) experiments.

The determination of the structural parameters of $\text{TlIn}_x\text{Ga}_{1-x}\text{Se}_2$ and $\text{TlIn}_x\text{Ga}_{1-x}\text{S}_2$ systems were done by X-ray experiments. It was revealed that the variations of In and Ga contents in the crystals belonging to $\text{TlIn}_x\text{Ga}_{1-x}\text{Se}_2$ selenide system resulted in the transformation of crystal structure from chained ($\text{Tl}_4\text{In}_3\text{GaSe}_8$) to layered ($\text{Tl}_4\text{InGa}_3\text{Se}_8$). Meanwhile, the unit cell type changes from tetragonal ($\text{Tl}_4\text{In}_3\text{GaSe}_8$) to monoclinic ($\text{Tl}_4\text{InGa}_3\text{Se}_8$). On the other hand, crystals belonging to $\text{TlIn}_x\text{Ga}_{1-x}\text{S}_2$ sulfide system exhibited quite a different behavior: their crystal structures and unit cell types did not change with variations of In and Ga contents. To be more definite, it was found that all of the crystals had layered structures and

monoclinic unit cells. Furthermore, the determination of the compositional parameters of $\text{TlIn}_x\text{Ga}_{1-x}\text{Se}_2$ and $\text{TlIn}_x\text{Ga}_{1-x}\text{S}_2$ systems were done by EDSA experiments. It was revealed that the atomic composition ratio in all members of the $\text{TlIn}_x\text{Ga}_{1-x}\text{Se}_2$ and $\text{TlIn}_x\text{Ga}_{1-x}\text{S}_2$ systems were very close to the stoichiometric values.

On the basis of the temperature- and excitation laser intensity-dependent PL experiments on $\text{Tl}_4\text{In}_3\text{GaSe}_8$ crystals, two emission bands centered at 589 nm (2.10 eV, A-band) and 633 nm (1.96 eV, B-band) were observed in the spectra at $T = 30$ K. The variations of the spectra with temperature (16-300 K) that the transitions from two upper conduction bands (2.13 and 1.97 eV) to the acceptor levels with activation energies of 0.03 and 0.01 eV, respectively, could be responsible for the observed emissions. The sublinear increase of the emission bands' intensities with excitation intensity (0.0003-1.1777 W cm^{-2}) confirmed our assignment of these bands to free-to-bound recombination process. From the excitation intensity-dependent measurements, it was revealed that only B-band appeared in the spectra at low excitation intensities. However, as the excitation intensity was increased, A-band started to arise and became dominant in the spectra. This behavior was explained by shifting of quasi-Fermi level to higher energies with increasing excitation intensity.

For $\text{Tl}_4\text{InGa}_3\text{Se}_8$ crystals, the results of PL measurements showed the existence of a broad emission band centered at 652 nm (1.90 eV) at $T = 17$ K. The temperature-dependent measurements (17-68 K) supposed that the transitions between the donor level located at 0.43 eV below the bottom of the conduction band and the acceptor level located at 0.03 eV above the top of the valence band might be responsible for the observed emission band. The excitation intensity-dependent measurements (0.13-55.73 W cm^{-2}) revealed the sublinear behavior of emission band intensities, which confirmed the attribution of the observed emission band to donor-acceptor pair recombination.

To study the behaviors of the defect levels in $\text{Tl}_4\text{In}_3\text{GaS}_8$ crystals, PL measurements were carried out by using two different excitation sources: 406 nm (3.05 eV) line of a Hg-Xe arc lamp and 532 nm (2.33 eV) line of a YAG:Nd³⁺ laser as the intrinsic and extrinsic excitation sources, respectively. In the PL spectra, three emission bands centered at 514 nm (2.41 eV, A-band), 588 nm (2.11 eV, B-band), and 686 nm (1.81 eV, C-band) were observed with extrinsic excitation, whereas only A- and B-bands were observed with intrinsic excitation. The presence of the C-band

in the PL spectra excited by the former source, having higher excitation intensity than the latter source, was explained by the shift of quasi-Fermi level closer to the bottom of the conduction band. The results of the PL experiments as a function of temperature were analyzed under extrinsic excitation. As a consequence of the temperature-dependent measurements (26-130 K), A- and C-bands were attributed to the transitions from the donor levels located at 0.03 and 0.01 eV below the bottom of the conduction band to the acceptor levels located at 0.20 and 0.82 eV above the top of the valence band, respectively. Due to the blue shift of the B-band peak energy with increasing temperature, a CC model was proposed to account for this behavior. In accordance with this model, the activation energy of 0.02 eV obtained from thermal quenching for B-band was suggested to be the difference between the minimum of the excited state and the intersection point of the excited and ground state CC curves. The variations of the spectra with extrinsic excitation intensity (0.9-183.0 mW cm⁻²) revealed the sublinear increase of the intensity of the emission bands with respect to the excitation intensity, which justified that the observed emission bands were caused by the recombination of charge carriers involving donor-acceptor pairs.

The nature of defect levels in Tl₂InGaS₄ was studied by PL experiments. As a result of the measurements, three PL bands centered at 542 nm (2.29 eV, A-band), 607 nm (2.04 eV, B-band), and 707 nm (1.75 eV, C-band) were observed at $T = 15$ K. The temperature-dependent measurements (15-150 K) implied that the transitions from the donor levels located at 0.03 and 0.02 eV below the bottom of the conduction band to the acceptor levels located at 0.32 and 0.58 eV above the top of the valence band could be responsible for the observed A- and B-bands, respectively. Since the peak energy of the C-band with increasing temperature exhibits a blue shift, a CC model was proposed to explain this behavior. In line with this model, the activation energy of 0.06 eV obtained from thermal quenching for C-band was suggested to be the difference between the minimum of the excited state and the intersection point of the excited and ground state CC curves. By the excitation intensity-dependent measurements (0.01-100.34 W cm⁻²), the sublinear behavior of emission band intensities were revealed, affirming that the observed emission bands were due to donor-acceptor pair recombination. At low excitation intensities, it was also observed that B- and C-bands were present in the spectra; with the increasing of excitation intensity, the vanishing of B- and C-bands in the spectra was followed by

the emerging of A-band. This behavior of the bands was accounted for the shift of the quasi-Fermi level closer to the top of the valence band.

For $\text{Tl}_4\text{InGa}_3\text{S}_8$ crystals, the PL measurements were carried out with two different excitation sources: He-Cd laser with $\lambda_{\text{exc}} = 325$ nm (3.82 eV) and YAG:Nd³⁺ laser with $\lambda_{\text{exc}} = 532$ nm (2.33 eV) for intrinsic and extrinsic excitations, respectively. Only one band centered at 496 nm (2.49 eV, A-band) was observed in the PL spectra with intrinsic excitation. The spectra comprised another band centered at 580 nm (2.14 eV, B-band) with extrinsic excitation. This observation might be accounted for the assumption that A-band was a consequence of band-to-band excitation, while B-band was a result of excitation from an acceptor level. The variations of the emission spectra with respect to temperature revealed that the centers responsible for the emissions were the donor levels located at 0.02 and 0.37 eV below the bottom of the conduction band and the acceptor level located at 0.20 eV above the top of the valence band. In the case of extrinsic excitation, the behavior of emission band intensity with respect to excitation intensity (10.3-429.7 mW cm⁻²) was found to be sublinear. This result confirmed the proposal that the observed emission band was due to donor-acceptor pair recombination.

The above results of PL measurements suggested that the emission bands in the spectra obtained from the samples were mainly due to the transitions involving at least one localized state. As the studied crystals were not intentionally doped, the localized states present in the samples were thought to originate from stacking faults, which were due to weak interlayer bonding in studied crystals, and the uncontrolled impurities.

The room temperature transmission and reflection measurements made it possible to analyze the absorption edge of the crystals studied. The results of transmission measurements carried out on thick samples of $\text{Tl}_4\text{In}_3\text{GaSe}_8$ chain crystals in the near-infrared range revealed the indirect transitions with an energy of 0.94 eV. The analysis of transmission measurements done on thin samples (≈ 10 μm) of $\text{Tl}_4\text{InGa}_3\text{S}_8$, $\text{Tl}_4\text{In}_3\text{GaS}_8$, $\text{Tl}_2\text{InGaS}_4$, and $\text{Tl}_4\text{InGa}_3\text{S}_8$ layered crystals in the visible range revealed the coexistence of indirect transitions with energies of 1.94, 2.32, 2.35, and 2.40 eV and direct transitions with energies of 2.20, 2.52, 2.54 and 2.61 eV, respectively. It should be noted that with replacing of In and Ga atoms in $\text{TlIn}_x\text{Ga}_{1-x}\text{S}_2$ sulfide systems, the indirect and direct band gap energies were shifted to higher values, as expected. The transmission measurements in the temperature

range of 10-300 K were carried out on thick samples ($\approx 300 \mu\text{m}$) due to high fragility of thin samples at low temperatures. For this reason, it was possible to trace the temperature dependence of only indirect band gap energies. The rates of change of the indirect band gap energies with respect to temperature were determined to be $(-4.1, -6.0, -4.7 \text{ and } -6.0) \times 10^{-4} \text{ eV/K}$ for $\text{Tl}_4\text{InGa}_3\text{Se}_8$, $\text{Tl}_4\text{In}_3\text{GaS}_8$, $\text{Tl}_2\text{InGaS}_4$ and $\text{Tl}_4\text{InGa}_3\text{S}_8$ layered crystals, respectively.

To complete the characterization of the samples, the refractive index dispersion data were analyzed using the Wemple–DiDomenico single-effective-oscillator model. The oscillator and dispersion energies, and zero-frequency refractive indices were determined to be 4.10 eV, 23.17 eV, and 2.58 ($\text{Tl}_4\text{InGa}_3\text{Se}_8$), 4.87 eV, 26.76 eV and 2.55 for ($\text{Tl}_4\text{In}_3\text{GaS}_8$), 5.73 eV, 31.46 eV and 2.55 for ($\text{Tl}_2\text{InGaS}_4$), and 5.07 eV, 26.67 eV and 2.50 for ($\text{Tl}_4\text{InGa}_3\text{S}_8$), respectively.

REFERENCES

- [1] N. Arpiarian, *Proceedings of the International Conference on Luminescence*, 903 (1966).
- [2] H. W. Leverenz, *An Introduction to Luminescence of Solids*, Dover Publications, New York (1968).
- [3] S. Larach and A. Hardy, *Proceedings of the IEEE* **61**, 915 (1973).
- [4] E. N. Harvey, *A History of Luminescence From the Earliest Times Until 1900*, J.H. Furst Company, Baltimore, Maryland (1957).
- [5] K. A. Yee and A. Albright, *J. Am. Chem. Soc.* **113**, 6474 (1991).
- [6] Y. Shim, W. Okada, K. Wakita, and N. Mamedov, *J. Appl. Phys.* **102**, 083537 (2007).
- [7] S. Kashida, Y. Yanadori, Y. Otaki, Y. Seki, and A. M. Panich, *Phys. Stat. Sol. (a)* **203**, 2666 (2006).
- [8] V. Grivickas, V. Bikbajevs, and P. Grivickas, *Phys. Stat. Sol. (b)* **243**, R31 (2006).
- [9] Y. Rud, V. Rud, S. Iida, M. Morohashi-Yamazaki, H. Uchiki, and N. Mamedov, *Inst. Phys. Conf. Series* **152**, 967 (1998).
- [10] A. A. Ketelaar, W. H. t'Hart, M. Moerel, and D. Porter, *Z. Kristallogr.* **101**, 396 (1939).
- [11] M. Haniyas, A. Anagnostopoulos, K. Kambas, and J. Spyridelis, *Physica B* **160**, 154 (1989).
- [12] M. K. Rabinal, S. S. K. Titus, S. Asokan, E. S. R. Gopal, M. O. Godzhaev, and N. T. Mamedov, *Phys. Stat. Sol. (b)* **178**, 403 (1993).

- [13] K. R. Allakhverdiev, T. G. Mamedov, E. Y. Salaev, and I. K. Efendieva, *Phys. Stat. Sol. (b)* **113**, K43 (1982).
- [14] G. D. Guseinov, E. Mooser, E. M. Kerimova, R. S. Gamidov, I. V. Alekseev, and M. Z. Ismailov, *Phys. Stat. Sol.* **34**, 33 (1969).
- [15] S. Ellialtioglu, E. Mete, R. Shaltaf, K. Allakhverdiev, F. Gashimzade, M. Nizametdinova, and G. Orudzhev, *Phys. Rev. B* **64**, 195118 (2004).
- [16] G. Orudzhev, N. Mamedov, H. Uchiki, N. Yamamoto, S. Iida, H. Toyota, E. Gojaev, and F. Gashimzade, *J. Phys. Chem. Solids* **64**, 1703 (2003).
- [17] G. S. Orudzhev, E. M. Godzhaev, R. A. Kerimova, and E. A. Allakhyarov, *Phys. Solid State* **48**, 42 (2006).
- [18] K. Okazaki, K. Tanaka, J. Matsuno, A. Fujimori, L. F. Mattheiss, S. Iida, E. Kerimova, and N. Mamedov, *Phys. Rev. B* **64**, 045210 (2001).
- [19] K. R. Allakhverdiev, *Solid State Commun.* **111**, 253 (1999).
- [20] J. A. Kalomiros, N. Kalkan, M. Hantias, A. Anagnostopoulos, and K. Kambas, *Solid State Commun.* **96**, 601 (1995).
- [21] C. S. Yoon, S. J. Chung, S. J. Nam, and W. T. Kim, *Cryst. Res. Technol.* **31**, 229 (1996).
- [22] C. S. Yoon, B. H. Kim, D. J. Cha, and W. T. Kim, *Jpn. J. Appl. Phys.* **32**, 555 (1993).
- [23] I. M. Ashraf, M. M. Abdel-Rahman, and A. M. Badr, *J. Phys. D: Appl. Phys.* **36**, 109 (2003).
- [24] M. P. Hantias, A. N. Anagnostopoulos, K. Kambas, and J. Spyridelis, *Mat. Res. Bull.* **27**, 25 (1992).
- [25] N. Kalkan, J. A. Kalomiros, M. P. Hantias, and A. N. Anagnostopoulos, *Solid State Commun.* **99**, 375 (1996).
- [26] B. Abay, H. S. Guder, H. Efeoglu, and H. K. Yogurtcu, *Phys. Stat. Sol. (b)* **227**, 469 (2001).
- [27] A. Kato, M. Nishigaki, N. Mamedov, M. Yamazaki, S. Abdullaeva, E. Kerimova, H. Uchiki, and S. Iida, *J. Phys. Chem. Sol.* **64**, 1713 (2003).
- [28] H. J. Song, S. H. Hun, and W. T. Kim, *Solid State Commun.* **94**, 225 (1995).

- [29] I. M. Ashraf, *J. Phys. Chem. B* **108**, 10765 (2004).
- [30] G. A. Gamal, *Semicond. Sci. Technol.* **13**, 185 (1998).
- [31] K. Allakhverdiev, N. Akhmed-zade, M. Tagyev, and M. Shirinov, *Phys. Stat. Sol. (b)* **152**, 317 (1989).
- [32] K. Allakhverdiev, N. Akhmed-zade, M. Tagyev, M. Shirinov, and S. Haisler, *Phys. Stat. Sol. (b)* **148**, K93 (1988).
- [33] B. Kulbujev, Z. Rabkin, V. Torgashev, and Y. Izuk, *Fiz. Tverd. Tela* **30**, 195 (1988).
- [34] G. B. Abdullaev, G. I. Abutalybov, A. A. Aliev, L. S. Larionkina, I. K. Neimanzade, and E. Yu. Salaev, *JETP Lett.* **38**, 632 (1983).
- [35] T. Arai, J. Aoyagi, Y. Maryama, S. Onari, K. R. Allakhverdiev, and E. Bairamova, *Jpn. J. Appl. Phys.* **32**, (suppl. 3), 754 (1993).
- [36] K. R. Allakhverdiev, N. M. Gasanly, and A. Aydinli, *Solid State Commun.* **94**, 777 (1995).
- [37] A. E. Bakhyshov, A. A. Lebedev, Z. D. Khalafov, and M. A. Yakobson, *Sov. Phys. Semicond.* **12**, 320 (1978).
- [38] G. I. Abutalybov and E. Yu. Salaev, *Sov. Phys. Solid State* **28**, 1231 (1986).
- [39] S. G. Abdullaeva, N. T. Mamedov, F. A. Mustafaev, and E. Yu. Salaev, *Phys. Stat. Sol. (a)* **82**, K75 (1984).
- [40] R. A. Aliyev, G. D. Guseinov, A. I. Najafov, and M. Kh. Alieva, *Bull. Soc. Chim. France* **2**, 142 (1985).
- [41] E. A. Vinogradov, N. M. Gasanly, A. F. Goncharov, B. M. Dzhadov, and V. I. Tagirov, *Sov. Phys. Solid State* **22**, 526 (1980).
- [42] B. Abay, H. S. Guder, H. Efeoğlu, and Y. K. Yoğurtcu, *J. Phys. Chem. Solids* **62**, 747 (2001).
- [42] A. F. Qasrawi, and N. M. Gasanly, *Phys. Scripta* **76**, 249 (2007).
- [44] A. Aydinli, N. M. Gasanly, I. Yilmaz, and A. Serpenguzel, *Semicond. Sci. Technol.* **14**, 599 (1999).

- [45] N. M. Gasanly, A. Aydinli, A. Bek, and I. Yilmaz, *Solid State Commun.* **105**, 21 (1998).
- [46] N. M. Gasanly, A. Serpenguzel, A. Aydinli, and S. M. A. Baten, *J. Lumin.* **86**, 39 (2000).
- [47] B. Abay, H. Efeoglu, Y. K. Yogurtcu, and M. Alieva, *Semic. Sci. Tech.* **16**, 745 (2001).
- [48] G. E. Kimball, *J. Chem. Phys.* **3**, 560 (1935).
- [49] J. I. Pankove, *Optical Processes in Semiconductors*, Prentice Hall, New Jersey (1971).
- [50] M. Born and R. Oppenheimer, *Ann. Phys. (Leipzig)* **84**, 457 (1927).
- [51] B. Henderson and G. F. Imbush, *Optical Spectroscopy of Inorganic Solids*, Clarendon Press, Oxford (1989).
- [52] M. Gaft, R. Reisfeld, and G. Panczer, *Modern Luminescence Spectroscopy of Minerals and Materials*, Springer-Verlag, Berlin (2005).
- [53] R. W. Gurney and N. F. Mott, *Trans. Faraday Soc.* **35**, 69 (1939).
- [54] C. C. Klick and J. H. Schulman, *Solid State Physics*, Academic, New York (1957).
- [55] G. A. Russel and C. C. Klick, *Phys. Rev.* **101**, 1473 (1956).
- [56] Y. P. Varshni, *Physica* **34**, 149 (1967).
- [57] M. B. Panish and H. C. Casey, *J. Appl. Phys.* **40**, 163 (1969).
- [58] W. L. Bragg, *Proceedings of the Royal Society of London Series A* **17**, Part I, 43 (1913).
- [59] T. S. Moss, G. J. Burrell, and B. Ellis, *Semiconductor Opto-Electronics*, John Wiley & Sons, New York (1973).
- [60] S. H. Wemple and M. DiDomenico, *Phys. Rev. B* **3**, 1338 (1971).
- [61] S. H. Wemple and M. DiDomenico, *Phys. Rev. Lett.* **23**, 1156 (1969).
- [62] K. Tanaka, *Thin Solid Films* **66**, 271 (1980).

- [63] F. Yakuphanoglu, A. Cukurovali, and I. Yilmaz, *Physica B* **351**, 53 (2004).
- [64] F. Yakuphanoglu, A. Cukurovali, and I. Yilmaz, *Physica B* **353**, 210 (2004).
- [65] E. Marguez, P. Nagels, J. M. Gonzalez-Leal, A. M. Bernal-Oliva, E. Sleetckx, and R. Callaerts, *Vacuum* **52**, 55 (1999).
- [66] E. Marguez, A. M. Bernal-Oliva, J. M. Gonzalez-Leal, R. Prieto-Alcon, A. Ledesma, R. Jimenez-Garay, and I. Martil, *Mater. Chem. Phys.* **60**, 231 (1999).
- [67] A. F. Qasrawi and N. M. Gasanly, *Phys. Stat. Sol. (a)* **202**, 2501 (2005).
- [68] M. M. El-Nahass, M. M. Sallam, S. A. Rahman, and E. M. Ibrahim, *Solid State Sci.* **8**, 488 (2006).
- [69] A. K. Walton, and T. S. Moss, *Proc. Phys. Soc.* **81**, 509 (1963).
- [70] P. Y. Yu and M. Cardona, *Fundamentals of Semiconductors*, Springer, Berlin (1995).
- [71] P. J. Dean, *Prog. Cryst. Growth Charact.* **5**, 89 (1982).
- [72] T. Taguchi, J. Shirafuji, and Y. Inuishi, *Phys. Stat. Sol. (b)* **68**, 727 (1975).
- [73] D. E. Cooper, J. Bajaj, and P. R. Newmann, *J. Cryst. Growth* **86**, 544 (1988).
- [74] Z. C. Feng, A. Mascarenhas, and W. J. Choyke, *J. Lumin.* **35**, 329 (1986).
- [75] Q. Kim and D. W. Langer, *Phys. Stat. Sol. (b)* **122**, 263 (1984).
- [76] T. Schmidt, K. Lischka, and W. Zulehner, *Phys. Rev. B* **45**, 8989 (1992).
- [77] M. I. Nathan and T. N. Morgan, *Physics of Quantum Electronics*, McGraw-Hill, New York (1966).
- [78] D. G. Thomas, M. Gershenson, and F. A. Trumbore, *Phys. Rev.* **133**, A269 (1964).
- [79] K. Maeda, *J. Phys. Chem Solids* **26**, 595 (1965).
- [80] P. J. Dean and J. L. Merz, *Phys. Rev.* **178**, 1310 (1969).
- [81] E. Zacks and A. Halperin, *Phys. Rev. B* **6**, 3072 (1972).

- [82] J. Krustok, H. Collan, K. Hjelt, M. Yakushev, A. E. Hill, R. D. Tomlinson, H. Mandar, and H. Neumann, *J. Appl. Phys.* **83**, 7867 (1998).
- [83] W. Stadler, D. M. Hofmann, H. C. Alt, T. Muschik, B. K. Meyer, E. Weigel, G. Müller-Vogt, M. Salk, E. Rupp, and K. W. Benz, *Phys. Rev. B* **51**, 10619 (1995).
- [84] J. Lee, N. C. Giles, D. Rajavel, and C. J. Summers, *J. Appl. Phys.* **78**, 5669 (1996).
- [85] J. Krustok, V. Valdna, K. Hjelt, and H. Collan, *J. Appl. Phys.* **80**, 1757 (1996).
- [86] C. J. Hwang, *Physical Review* **180**, 827 (1969).
- [87] D. Muller, G. Eulenberger, and H. Hahn, *Z. Anorg. Allg. Chemie* **398**, 207 (1973).
- [88] N. M. Gasanly, *J. Korean Phys. Soc.* **48**, 914 (2006).
- [89] J. Krustok, H. Collan, and K. Hjelt, *J. Appl. Phys.* **81**, 1442 (1997).
- [90] A. Jagomagi, J. Krustok, J. Raudoja, M. Grossberg, and M. Danilson, *Phys. Stat. Sol. (b)* **237**, R3 (2003).
- [91] S. Ellialtioglu, E. Mete, and O. Yildirim, *Proceedings of the 12th National Conference on Condensed Matter Physics*, 11, Ankara, Turkey (2005).
- [92] D. Muller and H. Hahn, *Z. Anorg. Allg. Chemie* **438**, 258 (1978).
- [93] J. R. Drabble and H. J. Goldsmid, *Thermal Conduction in Semiconductors*, Pergamon, Oxford (1961).
- [94] M. M. El-Nahass, A. M. M. Farag, E. M. Ibrahim, and S. A. Rahman, *Vacuum* **72**, 453 (2004).
- [95] O. Rybak, I. V. Blonskii, Ya. M. Bilyi, Yu. Lun, M. Makowska-Janusik, J. Kasperczyk, J. Berdowski, I. V. Kituk, and B. Sahraoui, *J. Luminescence* **79**, 257 (1998).
- [96] N. M. Gasanly, A. Serpenguzel, O. Gurlu, A. Aydinli, and I. Yilmaz, *Solid State Commun.* **108**, 525 (1998).

- [97] A. Anedda, M. B. Casu, A. Serpi, I. I. Burlakov, I. M. Tiginyanu, and V. V. Ursaki, *J. Phys. Chem. Sol.* **58**, 325 (1997).
- [98] R. Bacewicz, A. Dzierzega, and R. Trykozko, *Jpn. J. Appl. Phys.* **32**, 194 (1993).
- [99] J. A. Kalomiros and A. N. Anagnostopoulos, *Phys. Rev. B* **50**, 7488 (1994).
- [100] K. Goksen, N.M. Gasanly, and H. Ozkan, *J. Phys.: Cond. Matter* **19**, 256210 (2007).
- [101] A. Gauthier, A. Polian, J.M. Besson, and A. Chevy, *Phys. Rev. B* **40**, 3837 (1989).
- [102] V. Capozzi, *Phys. Rev. B* **28**, 4620 (1983).
- [103] A. F. Qasrawi and N. M. Gasanly, *Opt. Mater.* **29**, 1763 (2007).
- [104] A. Mercier, E. Mooser, and J. P. Voitchovsky, *J. Lumin.* **7**, 241 (1973).
- [105] H. L. Cotal, A. C. Lewandowski, B. G. Markey, S. W. S. McKeever, E. Cantwell, and J. Aldridge, *J. Appl. Phys.* **67**, 975 (1990).

VITA

The author of this work was born in Kırşehir on April 1, 1977. He received his B.S. and M.Sc. degrees in physics, both at Middle East Technical University (METU), Ankara, in 2000 and 2002. Since 2004, he has been employed as a teaching/research assistant by the Department of Physics at METU.

His main area of interest is structural and optical characterization of quaternary thallium chalcogenides by photoluminescence, transmission-reflection, X-ray and energy dispersive spectral analysis experiments.

Publications During Ph. D. Study:

1. Donor-acceptor Pair Recombination in $\text{Tl}_2\text{InGaS}_4$ Layered Crystals
K. Goksen, N.M. Gasanly, A. Aydinli, and H. Ozkan
J. Korean Phys. Soc., **47**, 267 (2005).
2. Visible Photoluminescence from Chain $\text{Tl}_4\text{In}_3\text{GaSe}_8$ Semiconductor
N. M. Gasanly and **K. Goksen**
J. Phys.: Cond. Matter, **18**, 6057 (2006).
3. Low-temperature Photoluminescence from $\text{Tl}_4\text{Ga}_3\text{InSe}_8$ Layered Crystals
K. Goksen, N. M. Gasanly, and R. Turan
Crystal Res. Technol., **41**, 822 (2006).
4. Dispersive Optical Constants and Temperature Tuned Band Gap Energy of $\text{Tl}_2\text{InGaS}_4$ layered crystals
K. Goksen, N. M. Gasanly and H. Ozkan
J. Phys.: Cond. Matter, **19**, 256210 (2007).
5. Optical Absorption and Reflection Studies of $\text{Tl}_4\text{InGa}_3\text{S}_8$ Layered Single Crystals
K. Goksen, N. M. Gasanly and H. Ozkan

Acta Phys. Pol. A, **112**, 93 (2007).

6. Optical Constants of $\text{Tl}_4\text{Ga}_3\text{InSe}_8$ Layered Single Crystals

K. Goksen and N. M. Gasanly

Physica B, **400**, 266 (2007).

7. Below and above Bandgap Excited Photoluminescence in $\text{Tl}_4\text{InGa}_3\text{S}_8$ Layered Single Crystals

K. Goksen and N. M. Gasanly

J. Phys.: Cond. Matter., **19**, 456221 (2007).

8. Temperature and Excitation Intensity Tuned Photoluminescence in $\text{Tl}_4\text{GaIn}_3\text{S}_8$ Layered Single Crystals

K. Goksen and N. M. Gasanly

Crystal Res. Technol., **43**, 514 (2008).

9. Refractive Index, Oscillator Parameters and Temperature Tuned Energy Band Gap of $\text{Tl}_4\text{In}_3\text{GaS}_8$ Layered Single Crystals

K. Goksen and N. M. Gasanly

J. Phys. Chem. Sol., (In press, 2008).